2011

Hyperpolarized 129Xe Apparent Diffusion Coefficient Anisotropy in an Elastase- Instilled Rat Model of Emphysema

Mathieu Boudreau

Hyperpolarized ^{129}Xe Apparent Diffusion Coefficient Anisotropy in an Elastase-Instilled Rat Model of Emphysema

(Spine title: Xenon-129 ADC Anisotropy in a Rat Emphysema Model)

(Thesis format: Integrated Article)

by

Mathieu Boudreau

Graduate Program in Physics

A thesis submitted in partial fulfillment
of the requirements for the degree of
Master of Science

The School of Graduate and Postdoctoral Studies
The University of Western Ontario
London, Ontario, Canada
August 2011

THE UNIVERSITY OF WESTERN ONTARIO
School of Graduate and Postdoctoral Studies

CERTIFICATE OF EXAMINATION

Supervisor

Dr. Giles Santyr

Supervisory Committee

Dr. John de Bruyn

Dr. Terry Thompson

Examiners

Dr. Eugene Wong

Dr. John de Bruyn

Dr. Jean Théberge

The thesis by

Mathieu Boudreau

entitled:

Hyperpolarized ^{129}Xe Apparent Diffusion Coefficient Anisotropy in an Elastase-Instilled Rat Model of Emphysema

is accepted in partial fulfillment of the requirements for the degree of Master of Science

Date

Chair of the Thesis Examination Board

Abstract

In recent years, hyperpolarized noble gas magnetic resonance diffusion measurements have shown remarkable sensitivity for diagnosing emphysema. The apparent diffusion coefficient (ADC) of hyperpolarized gases has also been shown to behave anisotropically in the lung at short diffusion times. In this work, we investigate hyperpolarized ^{129}Xe gas anisotropic ADCs of the Yablonskiy model *in vivo* in an elastase-instilled rat model of emphysema. Diffusion simulations in a budded cylinder model estimated that the transverse anisotropic ADC (D_T) may have optimal sensitivity at measuring airways enlargements, and that the optimal diffusion time to measure D_T with xenon is close to 5 ms. Measurements in sham and elastase-instilled rats were performed for a range of diffusion times, and the only significant increase of ADC was observed for D_T at 6 ms ($p < 0.005$), and a strong correlation between D_T and the mean linear intercepts from lung histology was observed ($r = 0.90$).

Keywords

Emphysema, magnetic resonance imaging, anisotropic apparent diffusion coefficient, elastase, hyperpolarized ^{129}Xe.

Co-Authorship Statement

Chapter 3 of this thesis was co-authored by M. Boudreau, X. Xu and G. E. Santyr and is being prepared for submission to Magnetic Resonance in Medicine (MRM).

To my parents Joanne and Valéri Boudreau, for nurturing a curious mind when I was young, and whose unconditional love and support have motivated me all these years.

To previous professors and mentors, Dr. Pandurang V. Ashrit, Dr. Georges Bader, Dr. Normand Beaudoin, Dr. Gisia Beydaghyan and Dr. Serge Gauvin, whom helped me become the scientist I am today.

To my girlfriend Gabrielle Lapointe, whose love, patience and encouragement during these two years made me thrive to succeed.

Acknowledgments

I would like to say thank you to the following individuals whose support made this thesis possible:

- My supervisor, Dr. Giles Santyr, for offering me the opportunity to do research at the Robarts Research Insitute at the University of Western Ontario. His knowledge and expertise provided much appreciated guidance for completing my degree. Thank you for always being honest in our discussions, keeping me on track, and for encouraging me to become a better researcher.
- The other members of my advisory committee, Dr. John de Bruyn and Dr. Terry Thompson, whom have provided me excellent guidance and support.
- Current and past members of the Santyr group: Marcus Couch, Ozkan Doganay, William Dominguez-Viqueira, Adam Farag, Matthew Fox, Elaine Hegarty, Susannah Hickling, Ian Jesse, Ryan Kraayvanger, Alexei Ouriadov, Julie Tanguay, Kundan Thind and Xiaojun Xu. For guidance, technical support and assistance during many experiments.
- Marcus Couch, who assisted every single one of my experiments with assistance running the animal ventilator, I offer my most sincere thank you for your help and your patience.
- To previous colleagues: Vincent Basque, Marc Collette, Richard Cyr, Allison MacKay and Gabrielle Lapointe. For support provided by always questioning and criticizing my work with open minds, and for the expert knowledge that you shared with me when needed.
- To my parents, Joanne and Valéri Boudreau, whose unconditional love and support have motivated me all these years.
- To my girlfriend, Gabrielle Lapointe, whose love, patience and encouragement during these two years made me thrive to succeed.
- Lastly I would like to thank the following organizations whom have made this work possible by providing financial support: the National Sciences and Engineering Research Council of Canada (NSERC), the Canadian Institutes of

Health Research CIHR, and the Ontario Provincial Government for help provided through the Ontario Graduate Scholarships in Science and Technology (OGSST).

Table of Contents

List of Tables

List of Figures

List of Appendices

List of Abbreviations

1D, 2D, 3D	One, two and three dimensional
ADC	Apparent diffusion coefficient
COPD	Chronic Obstructive Pulmonary Disease
CT	Computed tomography
Δ	Diffusion time
D_L	Longitudinal anisotropic diffusion coefficient
DLco	Diffusing capacity of carbon monoxide
D_0	Self-diffusion coefficient
D_T	Transverse anisotropic diffusion coefficient
Eqn.	Equation
FEV_1	Forced expiratory volume in 1 second
Fig.	Figure
G_m	Maximal gradient strength in a PGSE sequence
HNG	Hyperpolarized noble gases
IU	International units
L_m	Mean linear intercept
MR	Magnetic resonance
MRI	Magnetic resonance imaging
PET	Positron emission tomography

PIP	Peak inspiratory pressure
PGSE	Pulse gradient spin echo
ppm	Parts per million
PSI	Pounds per square inch
Rb	Rubidium
SAR	Specific absorption rate
SEOP	Spin exchange optical pumping
SNR	Signal to noise ratio
SPECT	Single photon emission computed tomography
T_1	Longitudinal relaxation time
T_2	Transverse relaxation time

Chapter 1

1 Introduction

1.1 Motivation

Chronic obstructive pulmonary disease (COPD) is projected to be the third natural leading cause of mortality worldwide by 2030 (1). While deaths from cardiovascular diseases and stroke has been steadily declining due to reduction in lifestyle risk factors and improvements in therapies (2,3), COPD deaths has been progressively increasing. Although the prevention of smoking induced COPD plays a key role in reducing the mortality rate, the development of clinical diagnostic modalities for the early stages of the disease are required to assess the risks to the patient at earlier stages and to develop treatments and therapies. Recent studies have shown (4,5) that emphysema is detectable by measuring diffusion of hyperpolarized noble gases (^{3}He) in the lung with magnetic resonance imaging (MRI). This thesis will focus on investigating emphysema-like alveolar damage in a murine disease model with the use of another hyperpolarized noble gas (^{129}Xe) with MRI diffusion measurements.

1.2 Pulmonary Physiology and Pathophysiology

1.2.1 Normal Lungs

The lung is the site of gas exchange between the atmosphere and the circulating blood of the body. Air flows into the trachea by contracting the diaphragm, and for humans branches out into approximately 23 fractal airway generations (6). The conducting zone consists of the first 16 generations (bronchi, bronchiole, terminal bronchioles), while gas exchange occurs progressively in the remaining generations, called the transitional and respiratory zones (respiratory bronchioles, terminal airways, alveolar sacs) (7), diffusing into the alveoli. Figure 1.1 shows the acinus of the lungs, which is composed of the terminal airways covered with alveoli.

Recent studies estimates that the human lung contains approximately 480 million alveoli with a mean diameter of 0.2 mm (8). The lung has a volume of about 4 liters at 60% of total lung capacity with an alveolar surface area of 130 m^2, which makes it extremely efficient for gas exchange (9). The alveoli are covered with a system of capillaries through which red blood cells flow, the diameter of a capillary being that of a single red blood cell. Inflowing blood excretes CO_2 into the airspace and absorbs O_2 from the airspace by diffusion through the lung parenchyma to balance the partial pressure gradients, with the oxygenated blood cells subsequently flowing into the pulmonary blood supply.

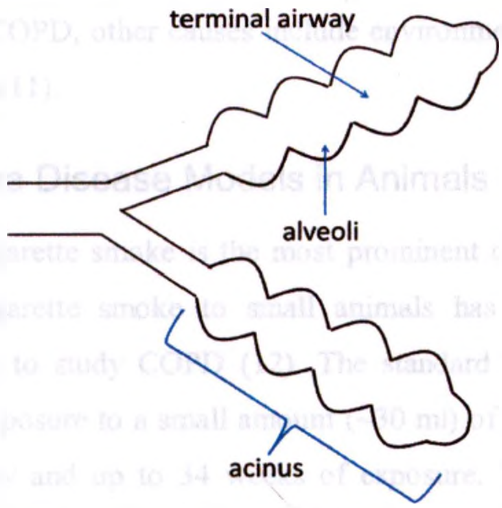

Figure 1.1. Conceptual drawing of the acinus of the lung.

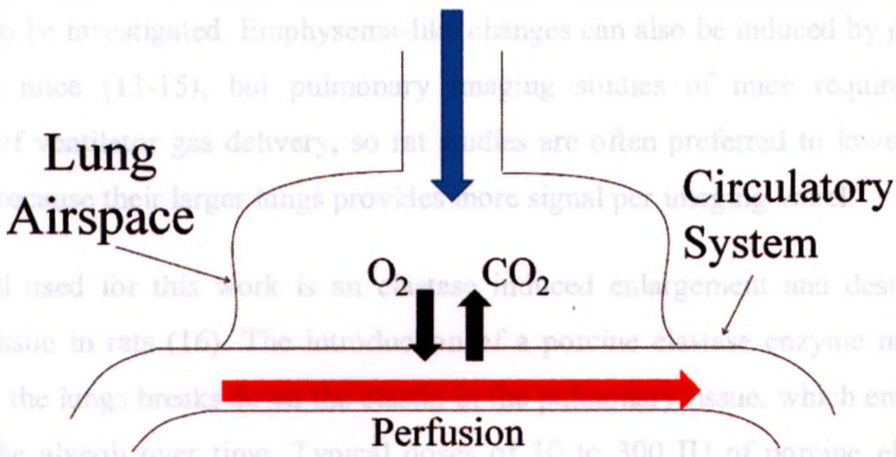

Figure 1.2. Schematic diagram of the breathing process. Air moves into the lungs where O_2 is extracted by diffusion through the capillary barrier into the circulatory system. CO_2 diffuses out of the blood that perfused to the capillaries, into the lung airspace and is then exhaled.

1.2.2 Chronic Obstructive Pulmonary Disease

Chronic obstructive pulmonary disease (COPD) is the co-occurrence of two separate abnormal lung properties: emphysema and airway disease. Airway disease encompasses chronic bronchitis, which is the thickening of the bronchiole walls and mucus secretion causing obstruction, and asthma, which is a reversible chronic inflammatory disease of the airways causing bronchoconstriction. Emphysema is an irreversible enlargement and destruction of alveolar tissue (10). While chronic inhalation of cigarette smoke is the most common cause of COPD, other causes include environmental pollutants as well as α_1-antitrypsin deficiency (11).

1.2.3 Emphysema Disease Models in Animals

Chronic inhalation of cigarette smoke is the most prominent cause of COPD. As such, chronic exposure of cigarette smoke to small animals has been established as an important disease model to study COPD (12). The standard protocol for this disease model in rats involves exposure to a small amount (~30 ml) of cigarette smoke every 60 seconds for 1 hour a day and up to 34 weeks of exposure. This model induces both chronic bronchitis-like mucus secretion as well as emphysema-like alveolar destruction, which makes it an unfavorable disease model when only the emphysema component of COPD is to be investigated. Emphysema-like changes can also be induced by genetically modifying mice (13-15), but pulmonary imaging studies of mice require extreme precision of ventilator gas delivery, so rat studies are often preferred to lower research costs and because their larger lungs provides more signal per imaging voxel.

The model used for this work is an elastase induced enlargement and destruction of alveolar tissue in rats (16). The introduction of a porcine elastase enzyme mixed with saline into the lungs breaks down the elastin in the pulmonary tissue, which enlarges and destroys the alveoli over time. Typical doses of 10 to 300 IU of porcine elastase are administered six to eight weeks prior to the study. This model does not induce any chronic bronchitis-like symptoms and can be used to model emphysema in small animals such as mice and rats as well as larger animals such as canines.

1.3 Diagnostic Techniques

1.3.1 Pulmonary Function Tests

Spirometry is the gold standard clinical test to assess lung function. It measures the volume of exhaled gas over time. The procedure consists of making a patient maximally inhale then exhale completely as fast as possible. The forced expiratory volume in 1 second (FEV_1) is the most common indicator of airway obstruction evident in mid and late stage COPD. A value of FEV_1 below 80% of that predicted for normal patients is considered to be a diagnostic criterion for COPD. Secondary indicators such as the diffusion capacity of carbon monoxide DLco can provide additional information for differentiation between diseases; DLco values have been shown to be normal to high in asthma patients but low for patients with emphysema (17-19).

Despite its common clinical use, spirometry has many disadvantages. It provides no regional information of disease heterogeneity and is also very patient effort dependent, which can lead to some demographics to be over diagnosed (i.e. the elderly).

1.3.2 Chest Radiography/Computed Tomography

The chest radiograph is the most common imaging modality for pulmonary diseases. Regardless of this fact, they can only provide indirect signs of mild COPD such as the flattening of the diaphragm and being abnormally low relative to the ribcage (20). Pulmonary bullaes are detectable in patients with severe emphysema, but symptoms are almost always present at this late stage of the disease.

Computed tomography (CT) has increasingly become the modality of choice for imaging clinical anatomical changes in the lungs when chest radiographies are inconclusive (21). Its high resolution (typically smaller than 1 mm^3 when using multi-detectors CT) enables good lung parenchyma visualization and can accurately quantify lung volume. CT measures the radiodensity of tissue in the Hounsfield Unit (HU) scale, which compares the linear attenuation observed of tissue with that of water: the radiodensity for water is 0 HU, air is -1000 HU. Emphysema can be estimated using the threshold cutoff (eg. lower than -960 HU) or percentile point analysis techniques (22). CT can also be used for functional pulmonary measurements, such as xenon-enhanced CT to quantify ventilation defects in asthmatics (23).

Despite this, CT has several limitations that do not make it an ideal imaging modality for pulmonary imaging. Emphysema quantification is can be sensitive to slice thickness due to noise, and there is a lack of agreement on the optimal Hounsfield unit threshold that describes emphysematous regions. High radiation dose inherent to CT scans (30 to 90 mSv per study) also limit frequent studies for adults with a life expectancy greater than 10 years (24).

1.3.3 PET/SPECT

Nuclear medicine imaging modalities have played a key role in functional imaging of the lung for many decades. Positron emission tomography (PET) detects a pair of gamma rays created by the annihilation of a positron emitted from a radionuclide (i.e. ^{18}F, ^{15}O), and this has provided excellent detection of single pulmonary nodules in high-risk smokers that are undetectable by chest radiography (25). Single photon emission computed tomography (SPECT) has also emerged in the pulmonary imaging field as an excellent tool to obtain ventilation/perfusion (V/Q) maps (26) in asthmatics (27) as well as detection of pulmonary embolisms (28,29), and has also shown sensitivity for quantifying emphysema (30,31). While nuclear imaging provides important functional pulmonary information, its use is limited by the radioactive dose the patient can safely receive as well as its low achievable resolution (26,32) (~1-2 cm).

1.3.4 Magnetic Resonance Imaging

Conventional magnetic resonance imaging (MRI) manipulates the orientation and precession of the magnetic moments of hydrogen in water molecules present in the body to provide spatial information on the hydrogen density and electromagnetic environment, without the use of ionizing radiation. Due to low hydrogen density in the lungs, clinicians do not typically chose MRI as their first choice of imaging modality for pulmonary diseases. Despite the low signal, some novel techniques aim at improving the MR signal and contrast of the lung. Oxygen-enhanced MRI acquires two images, one breathing normal air and the other introducing a high concentration of O_2 in the lungs, reducing the regrowth time of the signal (T_1) of the parenchyma tissue, subtracting the one image relative to the other to provide a signal difference image weighted by ventilation (33). Low field MRIs reduce the air-tissue susceptibility differences which increase the signal decay time constant (T_2*), allowing enough time to dynamically quantify ventilation defects by measuring change in tissue density during breathing cycles (34). Another novel technique recently developed is ventilation and perfusion mapping by Fourier decomposition analysis of the proton signal during the breathing cycle (35). The proton density in each voxel varies during a breathing cycle such that following inspiration, the alveoli is fully expanded and the proton density per voxel will be low, unlike following an expiration where the alveoli will have little gas and the proton density per voxel will be high. Fourier analysis of the signal in the time domain over several breathing cycles can separate signal varying at the breathing frequency and heart rate, and these measurements have been correlated to ventilation and perfusion.

Hyperpolarized noble gas (HNG) MRI is a recently developed technique that uses a contrast agent (^{3}He, ^{129}Xe) as the source of signal instead of protons (36). Unlike conventional MRI, where protons are collectively polarized by a strong magnetic field (thermal polarization, 1 to 10 ppm for clinical field strengths), HNG MRI pre-polarizes the contrast agent by spin-exchange optical pumping to polarization up to 10^4-10^5 larger than by thermal polarization prior to introducing it to the lungs (37). This enormous increase in collective magnetization compensates for the low density of the gas, producing signal densities similar to proton MRI in other regions of the body. This technique allows for both anatomical and functional information of the lung. In addition to measuring regional ventilation maps of asthmatics (38) and COPD patients (4), this technique can provide sub-voxel information such as alveolar dimensions by measuring the diffusion coefficients (4,39), as well as ^{129}Xe alveolar gas uptake and tissue densities measurements as a possible diagnostic tool for asthma and COPD (40,41). Recent studies have also shown (4,5) that emphysema is detectable by measuring a quantity called the apparent diffusion coefficient (ADC) of hyperpolarized ^{3}He, where there lies a correlation between ADC and alveolar airspace size. Most of the clinical research using HNG MRI until recently has mostly used ^{3}He, as its larger gyromagnetic ratio naturally provide a larger signal than ^{129}Xe having the same polarization, as well as because ^{3}He is naturally easier to polarize than ^{129}Xe (37). Due to recent increases in price of ^{3}He due to its low natural abundance, the United States of America has been tightening exports of ^{3}He. As a consequence, there has been a recent surge of ^{129}Xe studies (42,43) due to recent developments in large scale ^{129}Xe polarizers (44,45). In addition, ^{129}Xe has a self-diffusion coefficient approximately 30 times smaller than ^{3}He (46), which means that ADC studies using ^{129}Xe will likely need to employ considerably longer diffusion times than for ^{3}He to probe similar alveolar dimensions. It is for these reasons that this noble gas (^{129}Xe) that will be used for this work.

1.4 Physics of Magnetic Resonance Imaging

1.4.1 Nuclear Spin

An important property of nucleons and electrons is their intrinsic spin. Unlike the case of classical mechanics, the intrinsic spin $\vec{I}$ of neutrons and protons cannot be understood as the movement of the particle about its own axis, but must be regarded as a quantum mechanical property of matter, like mass, energy and charge. Spin $\vec{I}$ has an inherent angular momentum $\vec{J}$, and the relation between both is as follows:

$$\vec{J} = \hbar\vec{I} \qquad [1.1]$$

where $\hbar$ is the reduced Planck's constant. The magnetic moment $\vec{\mu}$ due to the spin of the particle is proportional to the angular momentum:

$$\vec{\mu} = \gamma\vec{J} \qquad [1.2]$$

where the gyromagnetic ratio γ is a constant unique to each nucleus.

Table 1.1: Gyromagnetic ratio of three commonly used atoms in MRI (47)

Atom	γ (10^{6} rad s^{-1} T^{-1})
^{1}H	267.52 2128
^{3}He	-203.801587
^{129}Xe	-74.52103

1.4.2 Dynamics of Magnetic Moments in Magnetic Fields

The classical dynamics of magnetic moments in an external magnetic field $\vec{B}$ is described by the Biot-Savart law, where the force $\vec{F}$ and torque $\vec{N}$ are as follows (48):

$$\vec{F} = \nabla(\vec{\mu} \cdot \vec{B}) \qquad [1.3]$$

$$\vec{N} = \vec{\mu} \times \vec{B}. \qquad [1.4]$$

In the presence of a homogeneous magnetic field, the right side of Eqn. [1.3] is null and only a torque is applied to the magnetic moment. The general relationship between the torque and angular momentum is:

$$\vec{N} = \frac{\mathrm{d}\vec{J}}{\mathrm{d}t}. \qquad [1.5]$$

Thus, by combining Eqn. [1.2] with [1.5], and merging this into Eqn. [1.4], the time evolution of a magnetic moment in a homogeneous external magnetic field can be expressed as:

$$\frac{\mathrm{d}\vec{\mu}}{\mathrm{d}t} = \gamma(\vec{\mu} \times \vec{B}). \qquad [1.6]$$

The solution for this type of differential equation is the behavior known as gyroscopic precession (49), as will now be demonstrated.

A common convention in nuclear magnetic resonance is to set the laboratory reference frame such that $\vec{B} = \mathrm{B}_0\hat{z}$. Equation [1.6] can thus be decomposed in the three orthonormal Cartesian components $\hat{x}$, $\hat{y}$ and $\hat{z}$:

$$\frac{\mathrm{d}\mu_x}{\mathrm{d}t} = \gamma \mathrm{B}_0 \mu_y \qquad [1.7]$$

$$\frac{d\mu_y}{dt} = -\gamma B_0 \mu_x \quad [1.8]$$

$$\frac{d\mu_z}{dt} = 0 \quad [1.9]$$

Equation [1.9] has $\mu_z = \mu_{z,0}$ as a solution, where $\mu_{z,0}$ is the initial magnetic moment aligned with the external magnetic field ($\mu_{z,0} = |\vec{\mu}|\cos(\theta)$, θ is the angle between $\vec{\mu}$ and the $\hat{z}$ axis). Equations [1.7] and [1.8] are a pair of coupled first order differential equations, which can be solved by introducing a complex magnetic moment $\mu_+ = \mu_x + i\mu_y$. Multiplying Eqn. [1.8] by i and adding it to Eqn. [1.7] yields:

$$\frac{d\mu_+}{dt} = -i\gamma B_0 \mu_+ \quad [1.10]$$

The solution of Eqn. [1.10] is well known to be:

$$\mu_+(t) = \mu_{xy} e^{-i\gamma B_0 t + \varphi} \quad [1.11]$$

where μ_{xy} is the modulus of μ_+ and φ is the initial phase. Knowing that equal complex vectors have equal real and imaginary parts, we get:

$$\vec{\mu}_x(t) = \mu_{xy}\cos(\gamma B_0 t + \varphi)\hat{x} \quad [1.12]$$

$$\vec{\mu}_y(t) = -\mu_{xy}\sin(\gamma B_0 t + \varphi)\hat{y}. \quad [1.13]$$

Thus, the overall behavior of $\vec{\mu}(t)$ is a precession about $\vec{B}$ (Fig. 1.3):

$$\vec{\mu}(t) = \mu_0 \sin(\theta)[\cos(\gamma B_0 t + \varphi)\hat{x} - \sin(\gamma B_0 t + \varphi)\hat{y}] + \mu_0 \cos(\theta)\hat{z} \quad [1.14]$$

where μ_0 is the magnitude of $\vec{\mu}$, which is constant. The angular frequency of precession is called the Larmor frequency ω_{LF} and is:

$$\omega_{LF} = \gamma B_0 . \quad [1.15]$$

For a 3.0 T magnetic field and a gyromagnetic ratio of 267.52 10^6 rad s^{-1} T^{-1} (proton), the angular frequency of precession is 802.6 10^6 rad/s or a linear frequency ν of 127.7 MHz.

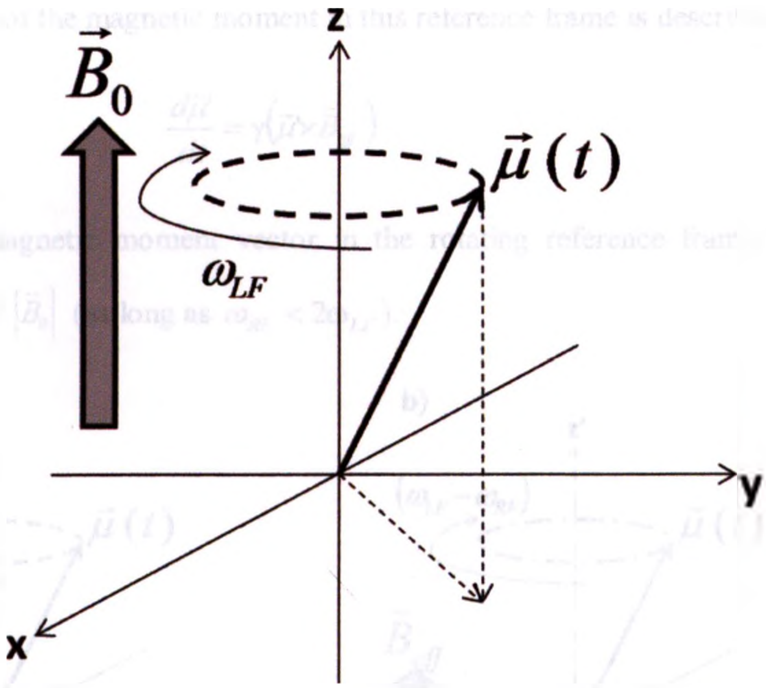

Figure 1.3: Precession of a magnetic moment about a static and homogeneous field, for γ > 0.

1.4.3 Rotating Frames of Reference

A helpful tool to conceptualize nuclear magnetic resonance experiments is that of a rotating frame of reference, indicated in equations and variables with the prime symbol. The rotating frame of reference is centered at the center of the laboratory frame of reference, but with the x' and y' rotating about the z' axis in the same direction as the precessing magnetic moment. Consider a rotating frame of reference that has an angular frequency $\omega_{RF} < \omega_{LF}$ relative to the laboratory. In the rotating frame, the magnetic moment will be precessing slower than ω_{LF} such that, in accordance to the previous section, we can state that it experiences an effective field $B_{eff} < B_0$ in the rotating frame of reference. It is simple to show that the effective field can be described by the following equation if there is only the static B_0 field in the laboratory frame of reference:

$$\vec{B}_{eff} = \left(B_0 - \frac{\omega_{RF}}{\gamma} \right) \hat{z}' . \quad [1.16]$$

Thus, the dynamics of the magnetic moment in this reference frame is described by:

$$\frac{d\vec{\mu}'}{dt} = \gamma \left(\vec{\mu}' \times \vec{B}_{eff} \right) \quad [1.17]$$

where $\vec{\mu}'$ is the magnetic moment vector in the rotating reference frame. Note that $|\vec{\mu}'| = |\vec{\mu}|$, but $|\vec{B}_{eff}| < |\vec{B}_0|$ (as long as $\omega_{RF} < 2\omega_{LF}$).

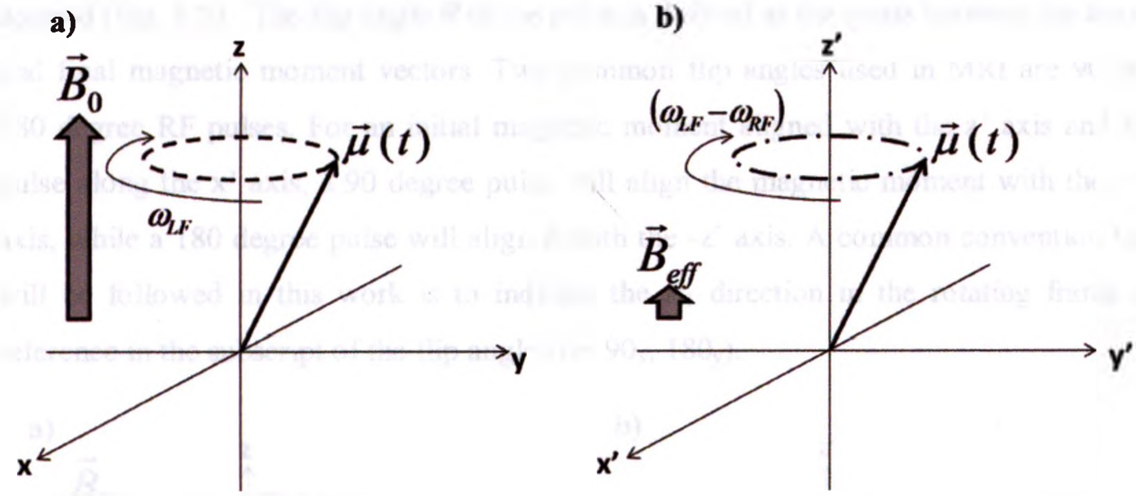

Figure 1.4: Example of a magnetic moment in a) the laboratory frame of reference and b) the rotating frame of reference.

1.4.4 Radio Frequency Pulses

A magnetic moment initially aligned along the static external magnetic field will not precess (see Eqn. [1.14]). A radiofrequency electromagnetic pulse can be used to manipulate the magnetic moment orientation. By applying a circularly polarized electromagnetic pulse at the frequency of the rotating frame of reference described in the previous section, a static B_1 field will be experience by the magnetic moment in the rotating reference frame:

$$\vec{B}_1 = B_1[\cos(\omega_{RF}t)\hat{x} - \sin(\omega_{RF}t)\hat{y}] = B_1\hat{x}' . \quad [1.18]$$

The effective magnetic field experienced by the nuclei is:

$$\vec{B}_{eff} = B_1\hat{x}' + \left(B_0 - \frac{\omega_{RF}}{\gamma}\right)\hat{z}' . \quad [1.19]$$

If the radiofrequency field (and rotating frame of reference) is on resonance with the Larmor frequency ($\omega_{RF} = \omega_{LF} = \gamma B_0$), the effective field is simply $\vec{B}_{eff} = B_1\hat{x}$, and the magnetic moment will precess about the x' axis for as long as the radiofrequency field is applied (Fig. 1.5). The flip angle θ of the pulse is defined as the angle between the initial and final magnetic moment vectors. Two common flip angles used in MRI are 90 and 180 degree RF pulses. For an initial magnetic moment aligned with the z' axis and RF pulse along the x' axis, a 90 degree pulse will align the magnetic moment with the +y' axis, while a 180 degree pulse will align it with the -z' axis. A common convention that will be followed in this work is to indicate the B_1 direction in the rotating frame of reference in the subscript of the flip angle (i.e. 90_x, 180_y).

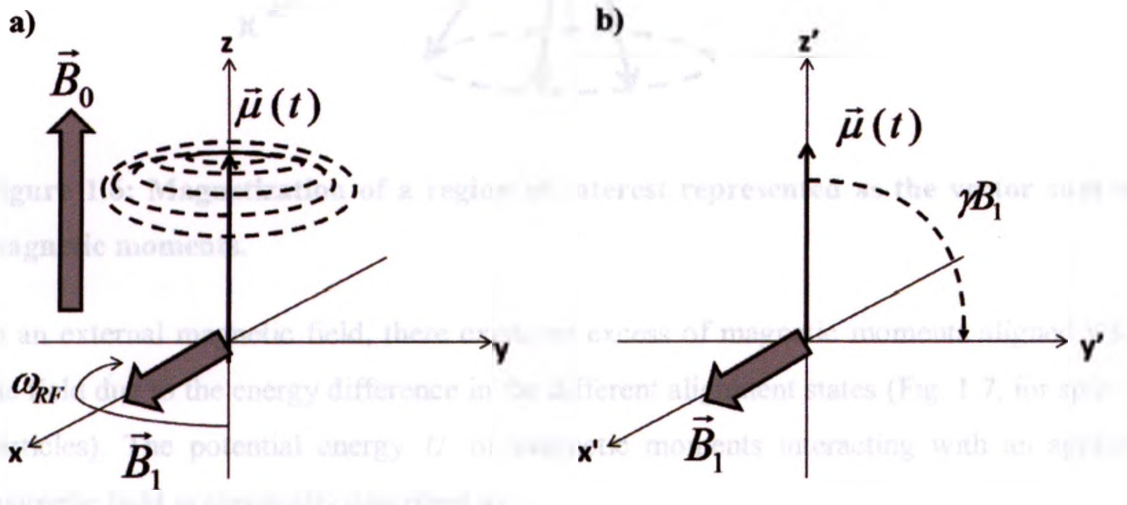

Figure 1.5. Example of a 90_x radiofrequency pulse in a) the laboratory frame of reference and b) a rotating frame of reference.

1.4.5 Magnetization in Thermal Equilibrium

Magnetization is the magnetic moment per unit volume of a system of particles [1.20]. As magnetic moments are a vector quantity, the net magnetization of a randomly oriented set of particles is zero. Thus, for a non-zero magnetization to be present there must be some mechanism that gives the particles an excess of population of a certain state (Fig. 1.6).

$$\vec{M} = \frac{1}{V}\sum_n \vec{\mu}_n \qquad [1.20]$$

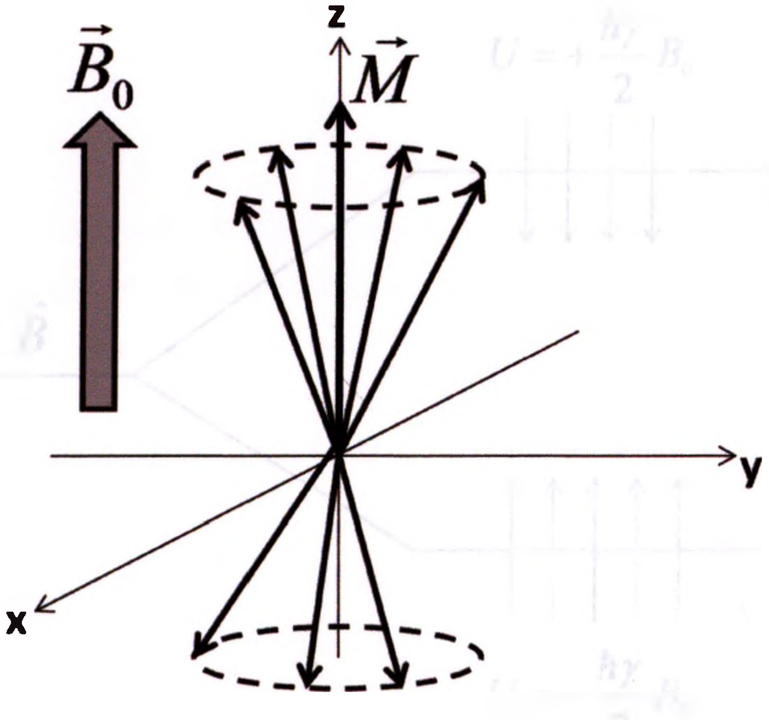

Figure 1.6: Magnetization of a region of interest represented as the vector sum of magnetic moments.

In an external magnetic field, there exists an excess of magnetic moments aligned with the field due to the energy difference in the different alignment states (Fig. 1.7, for spin ½ particles). The potential energy U of magnetic moments interacting with an applied magnetic field is classically described as:

$$U = -\vec{\mu} \cdot \vec{B}. \qquad [1.21]$$

Therefore the potential energy for spin ½ particles is:

$$U = \mp \frac{\hbar\gamma}{2} \mathrm{B}_0 \qquad [1.22]$$

where (-) is for the aligned state and (+) is for magnetic moment states anti-parallel to the field (Figure 7).

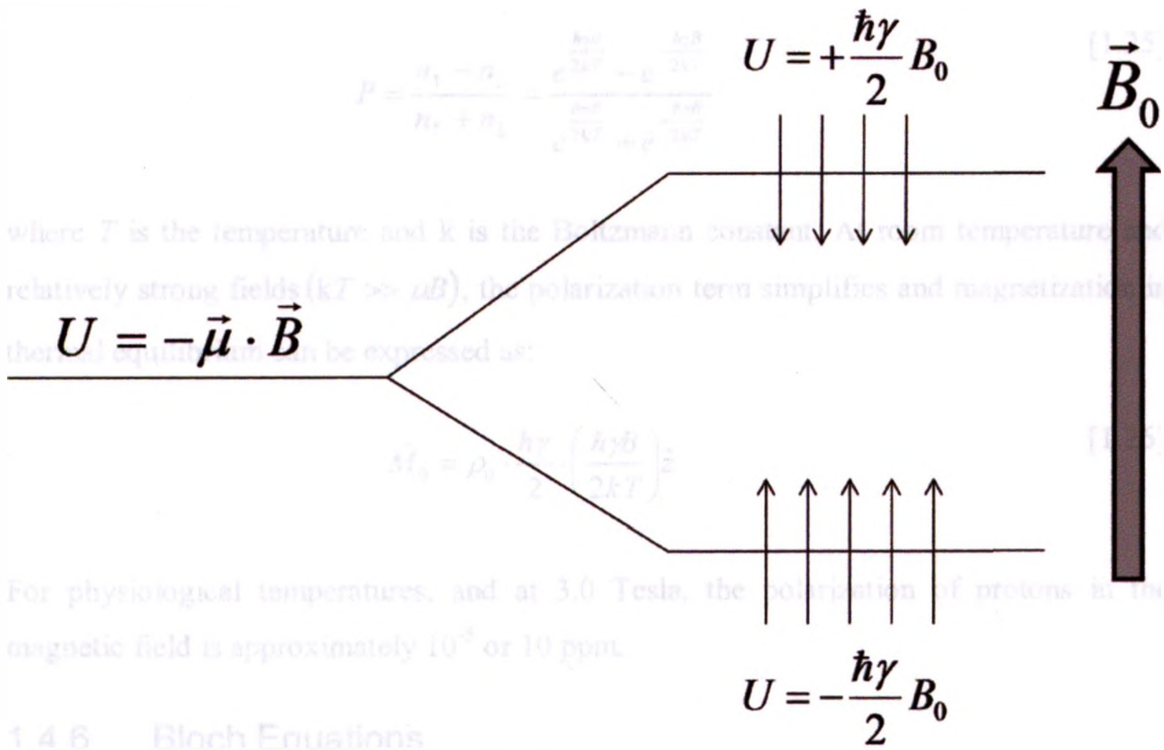

Figure 1.7: Energy splitting of a magnetic moment due to a spin ½ particle in the presence of an external magnetic field.

The magnetization in thermal equilibrium M_0 can be expressed as the following product:

$$M_0 = \begin{pmatrix}\text{Volume density} \\ \text{of particles}\end{pmatrix} \begin{pmatrix}\text{Magnitude of a particle's} \\ \text{magnetic moment in the} \\ \text{"z" direction}\end{pmatrix} \begin{pmatrix}\text{Net probability of alignment} \\ \text{with the external field}\end{pmatrix}. \qquad [1.23]$$

The first two terms are simply ρ_0 and $\frac{\hbar\gamma}{2}$, while the third can be expressed as the difference between the Boltzmann distribution for both states. This term is commonly called the polarization P of the material. M_0 can thus be written as:

$$M_0 = \rho_0 \cdot \frac{\hbar\gamma}{2} \cdot P \qquad [1.24]$$

Using Boltzman statistics, the thermal polarization of magnetic moments in an external magnetic field is:

$$P = \frac{n_\uparrow - n_\downarrow}{n_\uparrow + n_\downarrow} = \frac{e^{\frac{\hbar\gamma B}{2kT}} - e^{-\frac{\hbar\gamma B}{2kT}}}{e^{\frac{\hbar\gamma B}{2kT}} + e^{-\frac{\hbar\gamma B}{2kT}}} \qquad [1.25]$$

where T is the temperature and k is the Boltzmann constant. At room temperature and relatively strong fields $(kT >> \mu B)$, the polarization term simplifies and magnetization in thermal equilibrium can be expressed as:

$$\vec{M}_0 = \rho_0 \cdot \frac{\hbar\gamma}{2} \cdot \left(\frac{\hbar\gamma B}{2kT}\right)\hat{z} \qquad [1.26]$$

For physiological temperatures, and at 3.0 Tesla, the polarization of protons in the magnetic field is approximately 10^{-5} or 10 ppm.

1.4.6 Bloch Equations

The mathematical formulation of the dynamics of magnetic moments in an external magnetic field described by Eqn. [1.6] can be extended to the magnetization of a sample with macroscopic environmental considerations of interacting nuclei. Bloch generalized Eqn. [1.6] to the following equation, called the Bloch Equations (50), which is valid for liquid-like matter and gases:

$$\frac{d\vec{M}}{dt} = \gamma\left(\vec{M} \times \vec{B}\right) + \frac{M_x\hat{x} + M_y\hat{y}}{T_2} + \frac{(M_0 - M_z)\hat{z}}{T_1} \qquad [1.27]$$

where the effects of the T_1 term is called T_1 relaxation (also called longitudinal or spin-lattice relaxation) and that of the T_2 term is called T_2 relaxation (also called transverse or spin-spin relaxation). The reference frame of Eqn. [1.27] has the static magnetic field B_0 aligned with $\hat{z}$, but $\vec{B}$ is not limited to $\vec{B} = B_0\hat{z}$ (i.e. $\vec{B}$ can have time-dependence term, see Section 1.4.4).

1.4.7 T_1 Relaxation

T_1 relaxation is the mechanism that recovers the longitudinal magnetization to its thermal equilibrium value, M_0. To gain a better understanding of the behavior of the T_1 relaxation term in [1.27], this equation can be solved by neglecting the T_2 terms, as well as the precession term (valid for an on-resonance rotating frame of reference and for $\vec{B} = B_0\hat{z}$). This simplifies to:

$$\frac{\mathrm{d}M_z}{\mathrm{d}t} = \frac{(M_0 - M_z)}{T_1} \quad [1.28]$$

The solution of this equation is:

$$M_z(t) = M_{z0}e^{-\frac{t}{T_1}} + M_0\left(1 - e^{-\frac{t}{T_1}}\right) \quad [1.29]$$

where M_{z0} is the initial longitudinal magnetization at the time of observation. The behavior of $M_z(t)$ for three different initial conditions is shown in Fig. 1.8.

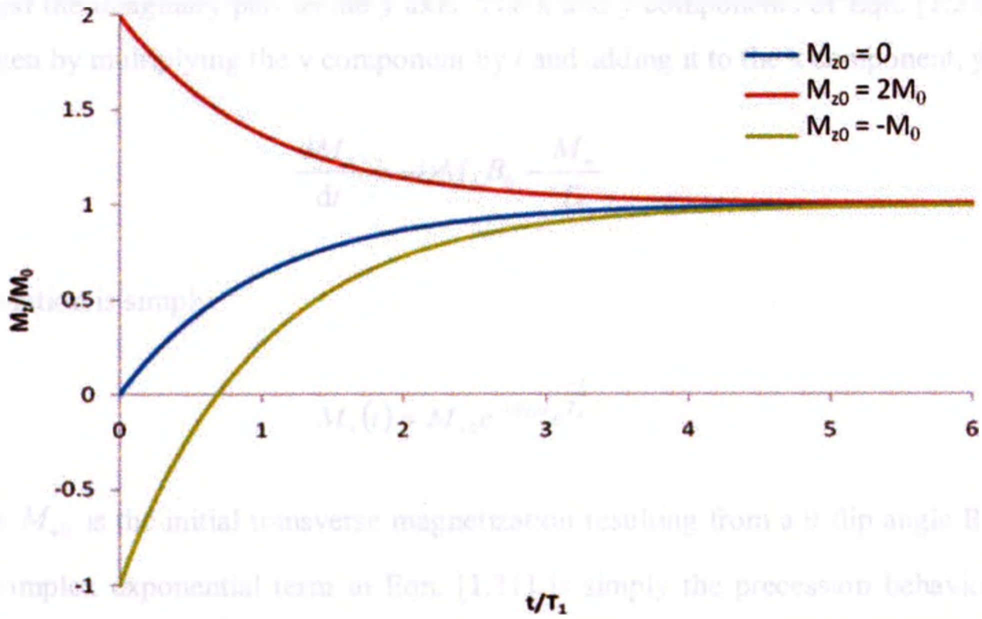

Figure 1.8: The decay/regrowth of the longitudinal component of the magnetization due to T_1 relaxation for three different initial conditions.

The source of T_1 decay results from the need of the spin system to establish its thermal equilibrium state magnetization (Eqn. [1.26]) after being perturbed from its equilibrium state. When the longitudinal magnetization is below or above M_0, rapidly oscillating transverse magnetic fields (in the x-y plane) near the Larmor frequency induces a transition of spin states, regrowing or decaying the total magnetization to its equilibrium magnitude. A wide variety of sources of oscillating fields occur in materials which will shorten T_1, including other magnetic moments in the medium (lattice) and paramagnetic molecules (i.e. O_2, Fe^{+2}).

1.4.8 T_2 Relaxation

T_2 relaxation is the mechanism that decays the transverse magnetization to its thermal equilibrium value, which is zero. As shown in the previous section, Eqn. [1.27] can be solved by neglecting the T_1 terms. Also, as M_x and M_y exhibit a similar but coupled behavior in the transverse plane, a common mathematical trick to simplify the analysis is to define a complex quantity $M_+ = M_x + iM_y$. This complex vector can be easily analyzed as the behavior of magnetization in the transverse plane, with the real part of M_+ as the x axis and the imaginary part as the y axis. The x and y components of Eqn. [1.27] can be rewritten by multiplying the y component by i and adding it to the x component, yielding:

$$\frac{dM_+}{dt} = -i\gamma M_+ B_0 - \frac{M_+}{T_2} \quad [1.30]$$

The solution is simply:

$$M_+(t) = M_{+0} e^{-i\omega_{LF} t} e^{\frac{-t}{T_2}} \quad [1.31]$$

where M_{+0} is the initial transverse magnetization resulting from a θ flip angle RF pulse. The complex exponential term in Eqn. [1.31] is simply the precession behavior of the magnetization about $\vec{B}_0$. The magnitude of the transverse magnetization decays exponentially, as can be seen in Fig. 1.9.

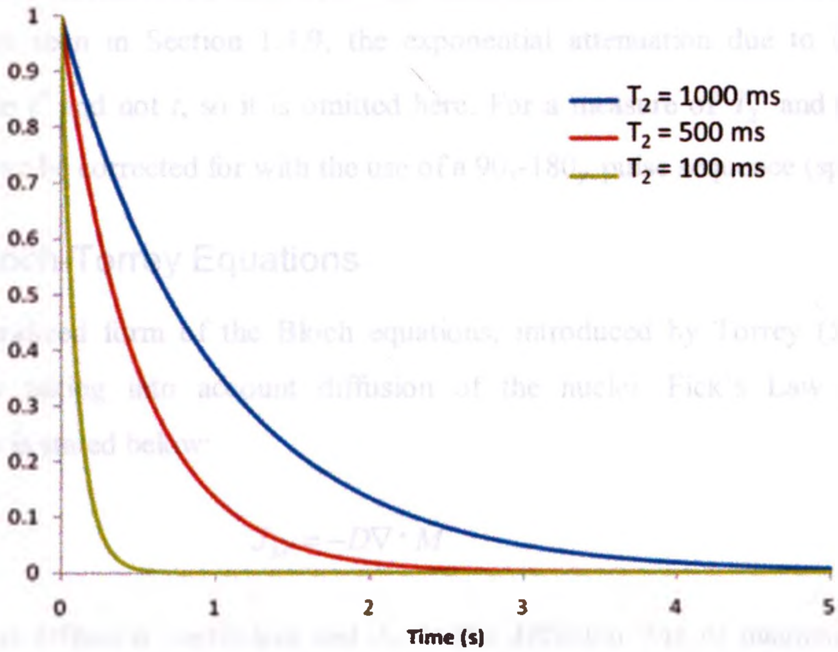

Figure 1.9: The decay of the transverse component of the magnetization due to T_2 relaxation for three different T_2 values.

The source of T_2 decay comes from the dephasing of precessing magnetic moments when there are longitudinal (z-direction) magnetic field inhomogeneities in the volume of interest. Spatial variations of B_z due to the proximity and orientation of neighboring nuclei creating dipolar magnetic fields cause spins to precess at different frequencies, creating an overall decoherence and dephasing of spins. The vector sum of this collection or dephasing spins will reduce the magnitude of the overall precessing magnetization vector as seen in Eqn. [1.31].

A correction to T_2 accounting for static field inhomogeneities (i.e. static B_0 field inhomogeneities) is called T_2^*, and is expressed as:

$$\frac{1}{T_2^*} = \frac{1}{T_2} + \frac{1}{T_2'} \qquad [1.32]$$

where T_2' is the transverse relaxation due to static field inhomogeneities. Often, attenuation due to diffusion through inhomogeneous fields is also included in Eqn. [1.32], but as will be seen in Section 1.4.9, the exponential attenuation due to diffusion is proportional to t^3 and not t, so it is omitted here. For a measure of T_2 and not T_2^*, T_2' contribution can be corrected for with the use of a 90_x-180_y pulse sequence (spin-echo).

1.4.9 Bloch-Torrey Equations

A more generalized form of the Bloch equations, introduced by Torrey (51), can be developed by taking into account diffusion of the nuclei. Fick's Law applied to magnetization is stated below:

$$J_M = -D\nabla \cdot \vec{M} \qquad [1.33]$$

where D is the diffusion coefficient and J_M is the diffusion flux of magnetization at a certain point in space. Another useful relation is the continuity equation applied to magnetization (assuming no T_1 or T_2 relaxation):

$$\frac{\partial \vec{M}}{\partial t} + \nabla J_M = 0 \quad [1.34]$$

Combining these two equations yields:

$$\frac{\partial \vec{M}}{\partial t} = \nabla\left(D\nabla \cdot \vec{M}\right) \quad [1.35]$$

The precession and relaxation terms developed previously can now be added to give the Bloch-Torrey equations:

$$\frac{\partial \vec{M}}{\partial t} = \gamma\left(\vec{M} \times \vec{B}\right) + \frac{M_x\hat{x} + M_y\hat{y}}{T_2} + \frac{(M_0 - M_z)\hat{z}}{T_1} + \nabla\left(D\nabla \cdot \vec{M}\right) \quad [1.36]$$

Note that the time-derivative is a partial derivative due to the fact that this is valid for a single point in space, a condition stemming from Eqn. [1.33] and [1.34].

An important solution of Eqn. [1.36] occurs when a constant linear field gradient G is applied. For this case, Torrey showed that the transverse magnetization M_+ (which is related to signal, see section 1.4.10) is:

$$M_+(t) = M_{+0} e^{-i\omega_{LF}t} e^{-\frac{t}{T_2} - bD} \quad [1.37]$$

where b, commonly referred to as the b-value (which is a measure of the diffusion sensitivity of the pulse sequence) and without explicitly stating its dependence on time, is a function of gradient strength and time. For a constant background gradient G_0, Torrey showed that the b-value is:

$$b = \frac{1}{3}\gamma^2 G_0^2 t^3 \quad [1.38]$$

b-values can also be determined for externally applied time-dependant gradients in pulse sequences, such that the decay in signal can provide a measure of the diffusion coefficient.

Diffusion coefficient measurements using MR can be commonly extracted from a two echo acquisition experiment, one signal echo acquisition S with an external gradient applied and one acquisition S_0 without any external gradients applied (to compensate for T_2 or T_2* effects), yielding the following relationship:

$$S = S_0 e^{-bD} \qquad [1.39]$$

The diffusing sensitizing pulse sequence used in this work is called the pulse gradient spin echo (PGSE) sequence with trapezoidal gradients, and is shown in Fig. 1.10. PGSE sequences have the advantage of having a well-defined diffusion time sensitivity related to the pulse sequence, and the signal from the echo is T_2 weighted due to the use of a spin-echo.

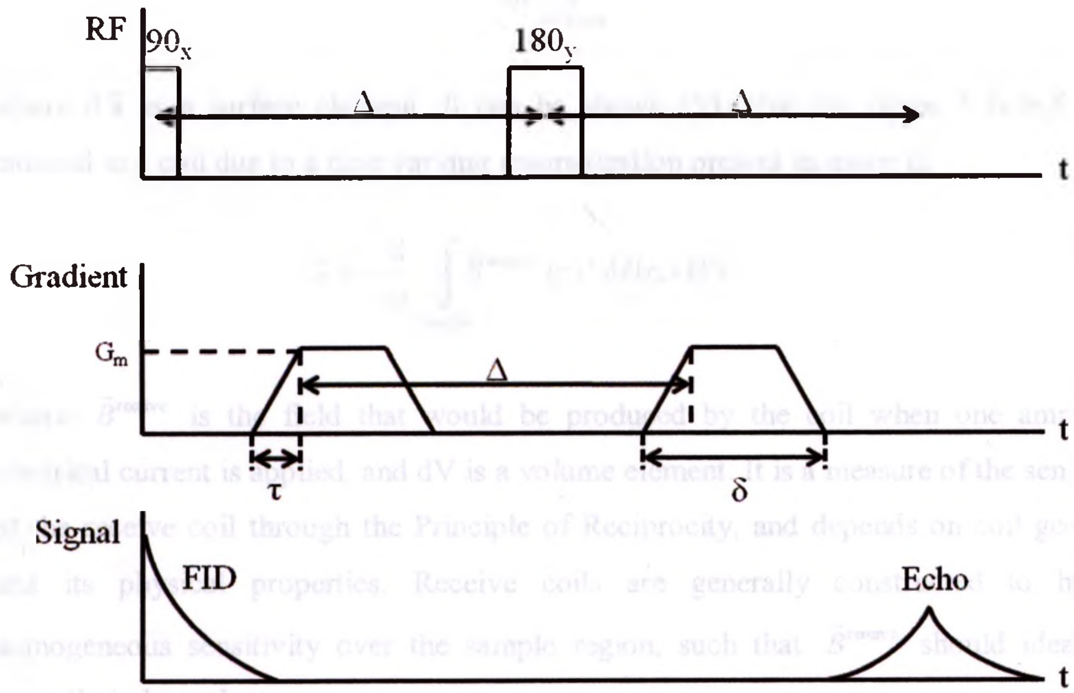

Figure 1.10. Pulse gradient spin echo pulse sequence using trapezoidal gradients. G_m is the maximal gradient strength, τ is the ramp up/down time, Δ is the diffusion time and δ is the gradient flat time + 2 τ.

The b-value associated with this sequence is (52):

$$b = (\gamma G_m)^2 \left[\delta^2 \left(\Delta - \frac{\delta}{3} \right) + \tau \left(\delta^2 - 2\Delta\delta + \Delta\tau - \frac{7}{6}\delta\tau + \frac{8}{15}\tau^2 \right) \right] \quad [1.40]$$

where G_m is the maximal gradient strength, τ is the ramp up/down time, Δ is the diffusion time and δ is the gradient flat time + 2τ.

1.4.10 Signal Equation

Precessing magnetization cause a flux of magnetic field that can be detected by the electromotive force (*e.m.f.*) induced through a conducting wire, a consequence of Faraday's Law:

$$e.m.f = -\frac{\mathrm{d}}{\mathrm{d}t} \int_{\text{Coil area}} \vec{B} \cdot \mathrm{d}\vec{s} \quad [1.41]$$

where $\mathrm{d}\vec{s}$ is a surface element. It can be shown (53) that the signal S (*e.m.f*, volts) induced in a coil due to a time varying magnetization present in space is:

$$S = -\frac{\mathrm{d}}{\mathrm{d}t} \int_{\text{Sample}} \vec{B}^{\text{receive}}(r) \cdot \vec{M}(r,t) \mathrm{d}V \quad [1.42]$$

where $\vec{B}^{\text{receive}}$ is the field that would be produced by the coil when one ampere of electrical current is applied, and dV is a volume element. It is a measure of the sensitivity of the receive coil through the Principle of Reciprocity, and depends on coil geometry and its physical properties. Receive coils are generally constructed to have a homogeneous sensitivity over the sample region, such that $\vec{B}^{\text{receive}}$ should ideally be spatially independent.

Since only time varying magnetization will contribute to the signal from the coils, we can ignore induction through T_1 regrowth/decay of the longitudinal magnetization (a variation much slower than the precession frequency) and simply implement the solution to the Bloch equations for precessing transverse magnetization into Eqn. [1.42], which yields the following signal equation:

$$S = A\frac{\hbar\gamma}{2}P\omega_{LF}e^{-i\omega_{LF}t}e^{\frac{-t}{T_2^*}}\int_{Sample}\rho_0(\vec{r})e^{-i\Delta\omega(\vec{r},t)t}dV \quad [1.43]$$

where A is a constant that contains $|\vec{B}^{receive}|$ and other electronic factors. The term $\Delta\omega(\vec{r},t)$ is the local precessing frequency offset that may depend on position and time, and manipulating this phase term in the integral can be used for acquiring images of the sample.

1.4.11 MR Imaging

Spatial images weighted by nuclei density, T_1 and T_2^* can be acquired by nuclear magnetic resonance with the addition of spatial magnetic field gradients. For the sake of simplicity, the signal equation above can be demodulated and T_2^* can be neglected such that:

$$S = \int_{Sample}\rho_{eff}(\vec{r})e^{-i\Delta\omega(\vec{r})t}dV \quad [1.44]$$

where all the constants in Eqn. [1.43] can be combined into one, $\rho_{eff}(\vec{r})$, which is the effective spatial nuclei density. In the absence of inhomogeneous fields, $\Delta\omega(\vec{r})$=0, the signal is simply proportional to the overall quantity of nuclei in the sample, independent of time (in reality, T_2^* decay would exponentially attenuate the signal). In the presence of linear magnetic field gradients $\vec{G} = \nabla B_z$, the magnetic field offset from $\vec{B}_0$ will be $\Delta B = \vec{G}\cdot\vec{r}$ and the phase in Eqn. [1.44] is given by:

$$\Delta\varphi(\vec{r},t) = \gamma\int\vec{G}dt\cdot\vec{r} \quad [1.45]$$

The signal equation can now be transformed into a three-dimensional Fourier transform of the effective spatial nuclei density by defining an angular wave number (also sometimes referred to as a spatial frequency) as:

$$\vec{k}(t)=\frac{\gamma}{2\pi}\int_{o}^{t}\vec{G}dt' \quad [1.46]$$

Thus:

$$S=\int_{Sample}\rho_{eff}(\vec{r})e^{-i2\pi\vec{k}(t)\vec{r}}dV \quad [1.47]$$

Equation [1.47] can be interpreted as the Fourier transform of the effective nuclei density of the sample, what is commonly known as k-space. By controlling gradients prior and during acquisition, k-space can be discretely acquired and applying the inverse Fourier transform produces an image of the sample. Figure 1.11 shows an example of an imaging pulse sequence, while Fig. 1.12 shows an example Cartesian k-space acquisition scheme.

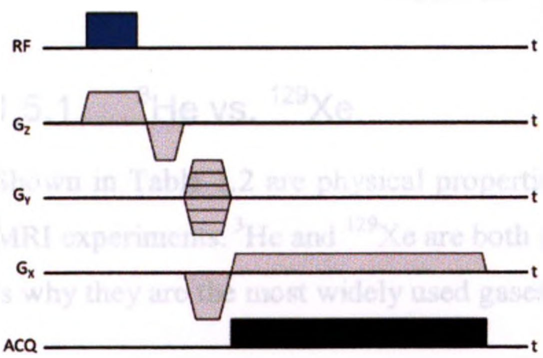

Figure 1.11. Gradient echo imaging pulse sequence. Gz, Gy and Gx are called the slice select, the phase encode and the readout gradients, respectively. The amplitude of Gy changes before each acquisition of a k-space line.

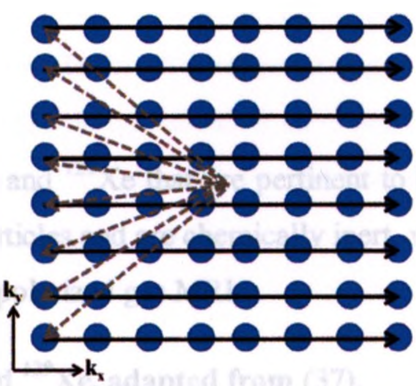

Figure 1.12. Cartesian k-space acquisition scheme. The grey dashed lines represent k-space trajectory of the gradients before acquisition, and the black line represents the trajectory during acquisition.

1.5 Hyperpolarized Noble Gases

Hyperpolarized noble gases have been used as an MRI contrast agent for almost 20 years (36). Though initially conceived as brain activation contrast agent, they have been mostly used for pulmonary imaging due to the practical administration of the gas into the lungs, as well as the wide breadth of anatomical and functional investigational uses, as described in Section 1.3.4. The gas is pre-polarized outside of the main magnet by a spin exchange optical pumping (SEOP) process that takes tens of minutes to a few hours, resulting in polarization levels of up to 64% (44), thus 10^4 to 10^5 times higher than achievable by thermal polarization at clinical field strengths. As a consequence, after the SEOP process, T_1 relaxation results in the decay of the longitudinal magnetization to thermal equilibrium M_0 (Fig. 1.8). Thus, proper handling of the gas prior to imaging is critical, as well as the use of appropriate pulse sequence technique to use the magnetization in the most effective manner possible. The magnetization from hyperpolarized gases can be described by the following equation for spin ½ particles, where P_{HP} is the polarization of the gas and is independent of the imaging magnetic field:

$$\vec{M}_{HP} = \rho_0 \cdot \frac{\hbar\gamma}{2} \cdot P_{HP}\hat{z} \qquad [1.48]$$

1.5.1 ^{3}He vs. ^{129}Xe

Shown in Table 1.2 are physical properties of ^{3}He and ^{129}Xe that are pertinent to HNG MRI experiments. ^{3}He and ^{129}Xe are both spin ½ particles and are chemically inert, which is why they are the most widely used gases in hyperpolarized gas MRI.

Table 1.2: Physical properties of ^{3}He and ^{129}Xe, adapted from (37).

Parameter	^{3}He	^{129}Xe
Nuclear spin, I	1/2	1/2
Gyromagnetic ratio, γ (10^6 rad s^{-1} T^{-1})	-203.781587	-74.52103
Natural abundance of the isotope (%)	1.37 x 10^{-4}	26.4
Self diffusion coefficient, D_0(cm^2 s^{-1})	2.05	0.061
Diffusion coefficient in air, D (cm^2 s^{-1})	0.86	0.14
Ostwald solubility in blood, L	0.0085	0.17
Chemical shift range (ppm)	~0.8	~250

If hyperpolarized to the same polarization (P_{HP}), ^{3}He will provide a signal 7.5 larger than ^{129}Xe due to their difference in gyromagnetic ratios, as the magnitude of the signal from hyperpolarized gases can be described as:

$$S_{HP} = \omega_0 \rho_0 \cdot \frac{\hbar|\gamma|}{2} \cdot P_{HP}. \quad [1.49]$$

For this reason, ^{3}He has been studied more intensively in the past 15 years. Unfortunately, as can be seen by their natural abundances, ^{3}He is a lot scarcer than ^{129}Xe, making it a very expensive research agent. Also, some countries have recently banned exports of ^{3}He, making it very difficult to purchase ^{3}He at a reasonable price from other countries. ^{129}Xe has an advantage over ^{3}He due to its higher solubility in the blood and larger chemical shift, providing a significantly larger signal from dissolved gas into the blood, which is a useful tool for investigating various diseases affecting the lung parenchyma.

The self diffusion coefficients of ^{129}Xe and ^{3}He are drastically different, ^{3}He having a self diffusion coefficient over 30 times larger than ^{129}Xe, which implies that hyperpolarized MRI diffusion experiments using ^{129}Xe need a much longer time than ^{3}He to probe the same microstructure dimensions. One solution to alleviate this difference (if this is not a desired feature), would be to mix the hyperpolarized gas with medical air or nitrogen as it is being inhaled. As can be seen from Table 1.2, mixing 50% air with the gas increase D_0 for ^{3}He but decreases D_0 for ^{129}Xe, reducing the ratio $D_{0,He}/D_{0,Xe}$ to 6.

1.5.2 Spin Exchange Optical Pumping

The most common hyperpolarization technique used for ^{129}Xe and ^{3}He is called Spin Exchange Optical Pumping (SEOP). An overview of this SEOP for ^{129}Xe will be described below. For a more in depth explanation of this technique, the reader is referred to Walker and Happer's excellent review on the subject (54).

A simplified diagram of the SEOP setup used in this thesis for ^{129}Xe is shown in Fig. 1.13. A gas mixture of ^{129}Xe, N_2, ^{4}He and an alkali metal (typically Rb) flows through a glass cell contained in a small but homogeneous magnetic field. A laser at the electron transition wavelength of the alkali metal (794.5 nm for Rb) is pumped through a quarter-wave plate to circularly polarize the beam, and is then transmitted through the optical cell (containing the gas mixture) in the direction parallel to the magnetic field. The photons polarize the Rb atoms valence electron collectively to a 100% aligned spin state, and then exchange its spin state with the ^{129}Xe atoms. The gas then flows through a glass trap submerged in liquid N_2 which quickly freezes the xenon atoms allowing the buffer gases to flow into the atmosphere. The xenon is then quickly thawed into a bag for delivery.

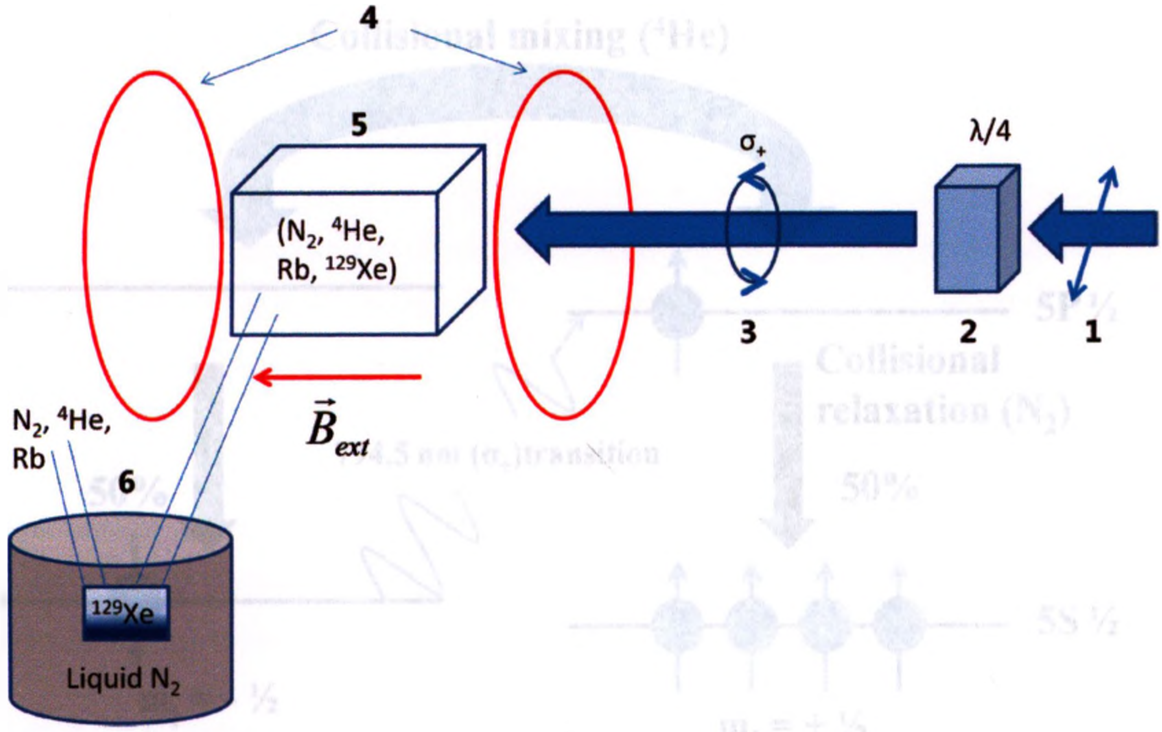

Figure 1.13. Experimental setup for spin exchange optical pumping. (1) Linearly polarized light. (2) Quarter wave plate. (3) Circularly polarizing the beam. (4) Source of homogeneous magnetic field. (5) Optical cell. (6) Glass trap immersed in a liquid N_2 bath.

1.5.2.1 Optically Pumping Rubidium

An overview of the mechanism of optically pumping rubidium is shown in Fig. 1.14. In equilibrium, the valence electron of Rb is in its ground state (5S½). When a small external magnetic field is present, the ground state is split into two states ($m_j = \pm$ ½), with approximately equal probability of being in either state. Incident laser light (794.5 nm) that is circularly polarized with positive helicity σ_+ will transition the electron state of a Rb in state 5S½ (m_j = - ½) to the excited state 5P½ (m_j = + ½); the transition between the ground (5S) and excited (5P) state is due to absorption of the photon at the transition wavelength (794.5 nm); the transition from the spin orientation m_j = - ½ to + ½ occurs as a consequence of the conservation of angular momentum due to the circular polarization of the photon.

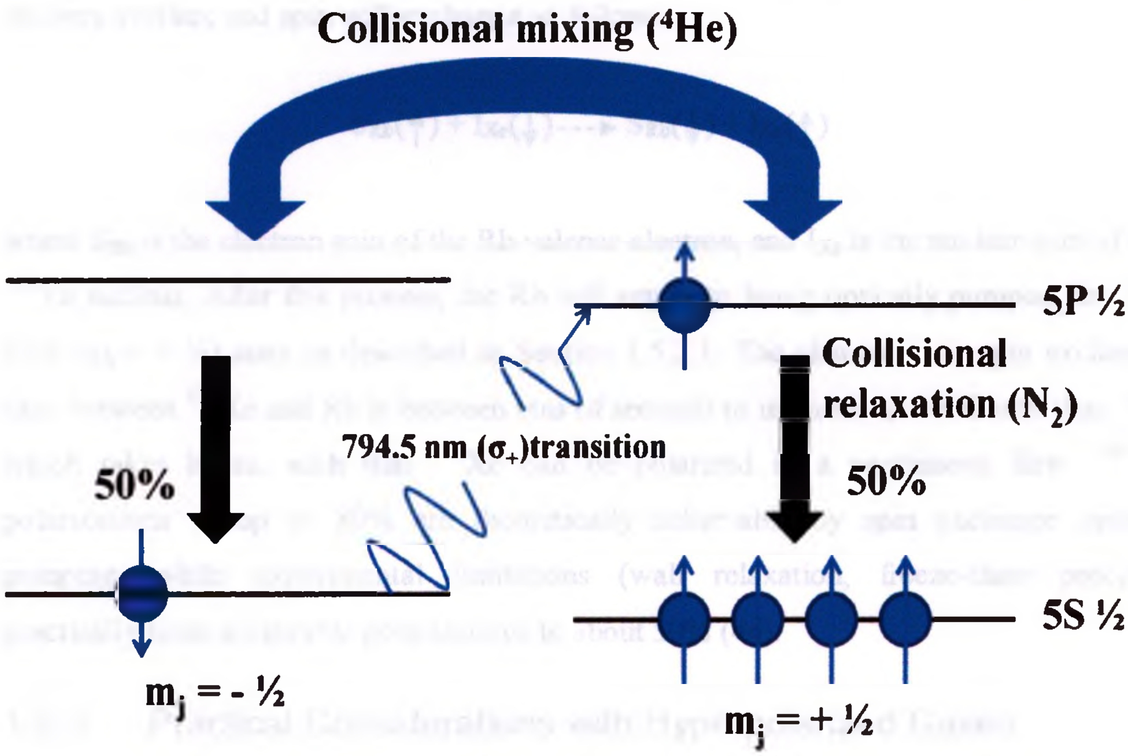

Figure 1.14. Schematic diagram of optical pumping Rb valence electrons into the 5S½ (m_j = ½) spin state.

Collisions with ^{4}He will change the spin orientation of the electron while keeping it in its excited state, such that after a short time the electron will have a 50% probability of being in either spin state. Energy exchange during collisions with N_2 atoms then causes transitions of the electron from the excited to the ground state without any emission of photons, and the spin orientation is conserved during this interaction. This whole process repeats until the collection of Rb atoms all have their 5S½ (m_j = - ½) state depleted. The photon is only absorbed by Rb electrons in the 5S½(m_j = - ½) state due to its circular polarization, and every Rb valence electron is in the 5S½ (m_j = + ½) state (100% aligned electron polarization).

1.5.2.2 Spin Exchange of Rb and ^{129}Xe

Once the Rb atoms have their valence electron fully polarized to the 5S½ (m_j = + ½) state, a spin exchange will occur between the Rb electron and the ^{129}Xe nucleus. A Fermi contact interaction may occur once the wave functions of the Rb electron and ^{129}Xe nucleus overlap, and spin will exchange as follows:

$$S_{Rb}(\uparrow) + I_{Xe}(\downarrow) \dashrightarrow S_{Rb}(\downarrow) + I_{Xe}(\uparrow)$$

where S_{Rb} is the electron spin of the Rb valence electron, and I_{Xe} is the nuclear spin of the ^{129}Xe nucleus. After this process, the Rb will return to being optically pumped into the 5S½ (m_j = + ½) state as described in Section 1.5.2.1. The characteristic spin exchange time between ^{129}Xe and Rb is between tens of seconds to minutes, much shorter than ^{3}He which takes hours, such that ^{129}Xe can be polarized in a continuous flow. ^{129}Xe polarizations of up to 80% are theoretically achievable by spin exchange optical pumping, while experimental limitations (wall relaxation, freeze-thaw process) practically limit achievable polarizations to about 50% (44).

1.5.3 Practical Considerations with Hyperpolarized Gases

Several practical considerations must be taken when using hyperpolarized gases in MRI (55). The most restrictive feature of hyperpolarize gases is that the longitudinal magnetization is non-renewable. Once depleted, the magnetization will only regrow to the thermal equilibrium value M_0, which cannot be used for imaging due to the low density of gases. As such, efforts must be made to minimize any environmental contributions that can increase T_1 decay (wall collision relaxation, oxygen). The pulse sequences can also be optimized to use the longitudinal magnetization most effectively during a series of RF pulse by applying variable flip angle (VFA) pulses (56). VFA provides a constant signal, compensating M_z losses due to previous RF pulses and T_1

decay by gradually increasing the flip angle of the RF pulses. Also, due to the high diffusivity of the gases, signal attenuation due to the imaging gradients must be accounted for in the data analysis by calculating the associated b-value for the pulse sequences.

1.6 Low Field MRI

Researchers and medical professionals using proton MRI have traditionally wanted to operate at high field strengths (3.0 – 9.4 T) to achieve much higher thermal polarization (Eqn. [1.26]) and signal (Eqn. [1.43]). Though higher field strengths provide various contrast advantages, great care must be taken in the development of MRI hardware, especially to reduce the specific absorption rate (SAR) in the subject due to RF pulses. For hyperpolarized gases, high field strengths are not typically necessary as the main magnetic field strength is not the source of the sample polarization, and the relationship between the signal to noise ratio (SNR) and field strengths is shown in Table 1.3.

Table 1.3: SNR dependence on field strength B_0, adapted from (57).

	Patient dominated noise Noise $\propto B_0$	**Receive coil dominated noise** Noise $\propto B_0^{1/4}$
Thermal polarization Signal $\propto B_0^2$	SNR $\propto B_0$	SNR $\propto B_0^{7/4}$
Hyperpolarization Signal $\propto B_0$	SNR $\propto {B_0}^0$ **(Field-independent)**	SNR $\propto B_0^{3/4}$

This lack of field dependence of hyperpolarized gas SNR in patient dominated noise suggests the possibility of imaging hyperpolarized gases at lower field strengths than clinical MRIs (< 1.0 T) without SNR penalties. Although patient-dominated noise is most commonly observed at high field strengths (~3.0 T for large chest coils), careful coil design can push the noise to the patient-dominated regime at field strengths as low as 73.5 mT (58).

Low field MRIs have the potential to be very useful for clinical lung imaging. Reduced hardware costs (resistive or permanent magnets, RF and gradient hardware), reduced

SAR and variable position MRI systems are all great advantages of going to lower field strength. In addition, studies have shown that T_2* of hyperpolarized gases in the lung increases at lower field strengths due to reduced susceptibility differences at the air-tissue interfaces of the airways (59). Optimal SNR at field strengths of approximately 0.1 T has been theoretically predicted for hyperpolarized gas MRI of the lungs (60). Long T_2^* are advantageous for long diffusion times studied in this work due to a longer signal lifetime.

1.7 Restricted Diffusion Measurements

1.7.1 Free Diffusion

The random movement exhibited by particles and molecules in thermal equilibrium is called Brownian motion. Though this process exists for all molecular environments (i.e. a single species of atoms or molecules, as well as a mixture), this mechanism explains the dispersion of molecules from high concentration regions into regions of low concentration, increasing the entropy of the entire system (Example: perfume diffusing throughout a room). In an unrestricted environment, the root-mean-square distance r_{rms} travelled by a particle over some time Δ in a particular molecular environment, having a self-diffusion coefficient D_0, has been shown in 3D to be (61):

$$r_{rms} = \sqrt{6D_0 \cdot \Delta} \quad [1.50]$$

where the diffusion coefficient D_0 is a function of pressure, temperature and the atomic/molecular species present. Molecules of a gas with a diffusion coefficient of 2.05 $cm^2\ s^{-1}$ (^3He) diffuses a root-mean-square distance of 7.84 mm in 50 ms, while molecules of another gas with D_0 of 0.061 $cm^2\ s^{-1}$ (^{129}Xe) would diffuse of 1.35 mm after this diffusion time.

1.7.2 Restricted Diffusion

In a restricted environment (i.e. a box, an alveolus), the distance a molecule can diffuse is limited by the geometrical dimensions of the boundaries and this restricts the achievable diffused distances (Fig. 1.15).

As can be seen in Fig. 1.14 c), Eqn. [1.50] is only valid for very short diffusion times where r_{rms} << the size of the container. The diffusion coefficient measured in a restricted environment is called the apparent diffusion coefficient (ADC), and is a function of diffusion time and the geometry of the environment in addition to the self-diffusion coefficient.

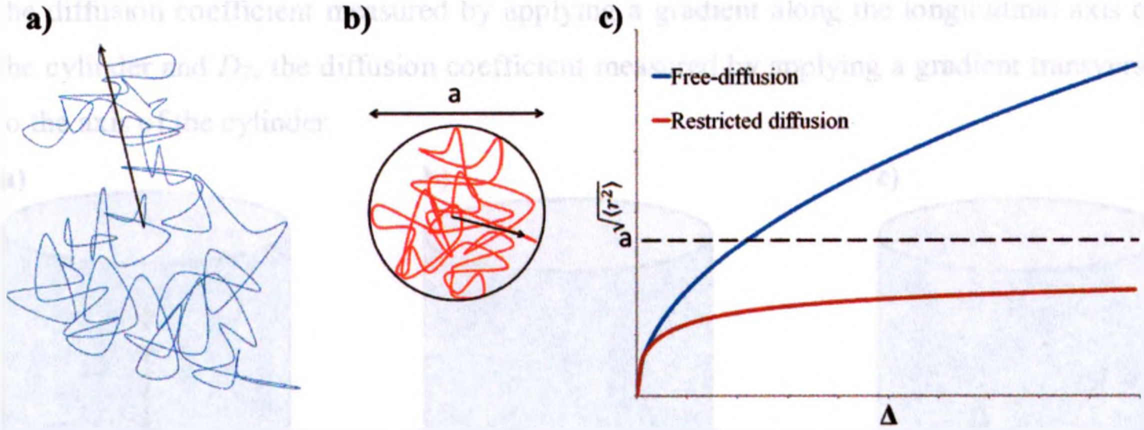

Figure 1.15. A particle diffusing in an unrestricted environment (a) and a restricted environment restricted by a spherical boundary (b). Shown in (c) is the conceptual relationship between the root-mean-squared displacement and diffusion time for these two cases.

In the context of MRI, ADCs can be measured in a similar way to that described in Section 1.4.9, yielding the following relationship for the case of an isotropically restricted environment:

$$S = S_0 e^{-bADC} \quad [1.51]$$

In anisotropic environments, ADC will depend on the orientation of the applied gradients and as such ADC may be better described as a tensor. A complete description of diffusion tensor imaging is beyond the scope of this work (62,63), but a pertinent case for hyperpolarized gas MRI anisotropic diffusion measurements of the lung is discussed in the following section.

1.7.3 The Yablonskiy Model of Anisotropic Apparent Diffusion Coefficients

For the case of gas diffusion in the lungs, the terminal airways can be approximated as infinite cylinders, neglecting the presence of alveoli. Due to the symmetry of the cylinder, the anisotropic ADC can be interpreted as having two orthogonal components (52); D_L, the diffusion coefficient measured by applying a gradient along the longitudinal axis of the cylinder and D_T, the diffusion coefficient measured by applying a gradient transverse to the axis of the cylinder.

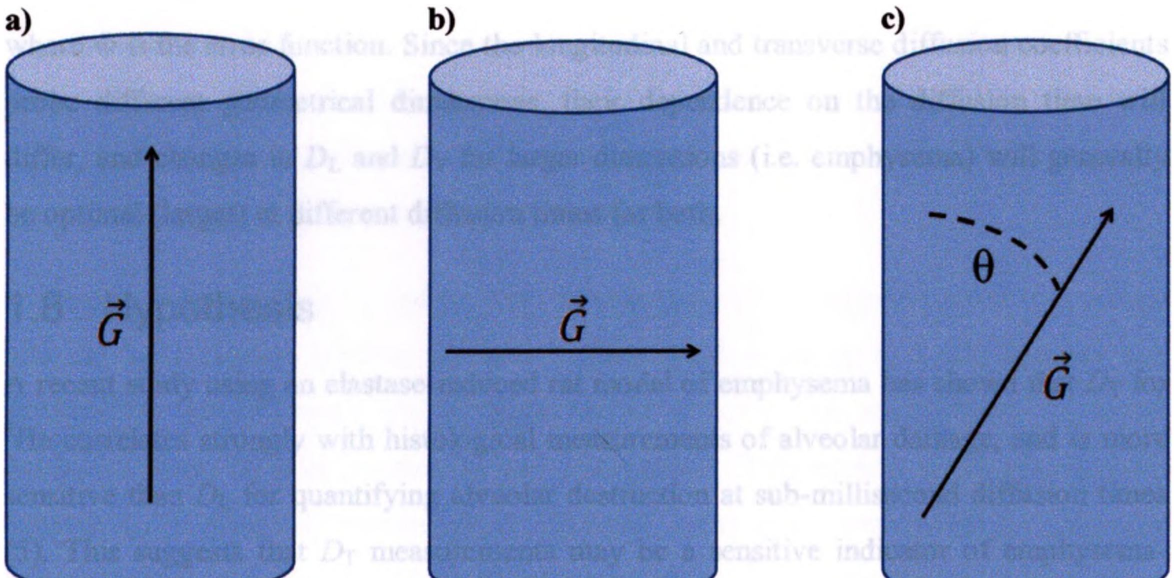

Figure 1.16. Cylinder model of the terminal airways. The ADC measured by applying a gradient along the principle axis of the cylinder (a) is called the longitudinal diffusion coefficient D_L, while the ADC measured by applying a gradient perpendicular to the long axis (b) is called the transverse diffusion coefficient D_T. For an arbitrary angle θ (c), ADC is given by Eqn. [1.52].

In the general case where the gradient is applied along some angle θ relative to the longitudinal axis of the cylinder, ADC is given by:

$$\mathrm{ADC}(\theta) = D_L \cos^2(\theta) + D_T \sin^2(\theta) \qquad [1.52]$$

When acquiring hyperpolarized gas images of the lungs, a single voxel could contain thousands of randomly oriented terminal airways so that Eqn. [1.52] cannot simply be introduced into Eqn. [1.50]. To simulate the effect of random orientation of the terminal airways on the signal, Eqn. [1.52] is introduced into Eqn. [1.50] and this term, weighted by $\sin(\theta)$, is integrated from 0 to π to yield:

$$\frac{S}{S_0} = e^{-bD_T}\left[\frac{\pi}{4b(D_L - D_T)}\right]^{1/2} \Phi\left\{\left[b(D_L - D_T)\right]^{1/2}\right\} \qquad [1.53]$$

where Φ is the error function. Since the longitudinal and transverse diffusion coefficients probe different geometrical dimensions, their dependence on the diffusion time will differ, and changes in D_L and D_T for larger dimensions (i.e. emphysema) will generally be optimal (larger) at different diffusion times for both.

1.8 Hypothesis

A recent study using an elastase-induced rat model of emphysema has shown that D_T for ^{3}He correlates strongly with histological measurements of alveolar damage, and is more sensitive than D_L for quantifying alveolar destruction at sub-millisecond diffusion times (5). This suggests that D_T measurements may be a sensitive indicator of emphysema-induced alveolar destruction. We hypothesized that anisotropic diffusion coefficients for ^{129}Xe can be as sensitive as ^{3}He to changes in alveolar airspace induced in an elastase-instilled rat model, and that significant increases in ADCs between sham and elastase-instilled lungs will be observed at considerably larger diffusion times (on the order of milliseconds) due to the inherently small self-diffusion coefficient of ^{129}Xe compared to ^{3}He.

1.9 Thesis Outline

The work presented in this thesis was completed by me in the Imaging Research Laboratories of the Robarts Research Institute under the supervision of Dr. Giles Santyr as an MSc student in the Department of Physics and Astronomy at the University of Western Ontario. This thesis is a collaborative work between me, Dr. Santyr and colleagues under the supervision of Dr. Santyr who assisted on occasion. The outline of my thesis and the explicit account of my contributions are as follows.

Chapter 2 uses a finite difference approach of numerically simulating the Bloch-Torrey equations for ^{129}Xe restricted diffusion in a 3-D budded cylinder model of the acinus and emphysematous morphological changes were modeled to identify the optimal diffusion times and Yablonskiy anisotropic diffusion coefficients to quantify emphysema. The simulations were written in C and the numerical fitting was done in Matlab. The code for this work was adapted from Xiaojun Xu's work with Dr. Santyr for her MSc project on ^{3}He diffusion (3). The code was changed to perform ^{129}Xe diffusion over a larger range of diffusion times, the geometrical parameters of the model were adjusted to model the airways of healthy and diseased lungs more appropriately, and various code optimizations were applied prior to performing my own simulations.

In Chapter 3, whole-lung D_L and D_T were measured *in vivo* at diffusion times of 6, 50 and 100 ms for 4 elastase-instilled rats and 5 sham-instilled rats at 73.5 mT. Elastase was instilled in the rat lungs six to eight weeks prior to the experiments to model emphysematous alveolar destruction and enlargement. This work is being prepared for submission to *Magnetic Resonance in Medicine*. I am solely responsible for the pulse sequence preparation and calibration, *in vitro* experiments, elastase and sham instillation, most of the animal preparation prior to the experiments, data analysis as well as histological measurements. Colleagues under the supervision of Dr. Santyr assisted with operating the ventilator, collecting ^{129}Xe, and a few animal preparations during the *in vivo* experiments. Dr. Santyr provided consultations and assistance with the manuscript preparation.

Chapter 4 summarizes the work of this thesis and provides ideas for future work using hyperpolarized ^{129}Xe diffusion, particularly to extend this work to include imaging to provide regional ADC maps, and application of anisotropic ADC maps for the purpose of *in vivo* morphology measurements. The ideas described in the chapter came from me in consultation with Dr. Santyr.

1.10 References

1. Mathers CD, Loncar D. Projections of global mortality and burden of disease from 2002 to 2030. PLoS Med 2006;3(11):e442.

2. Ford ES, Ajani UA, Croft JB, Critchley JA, Labarthe DR, Kottke TE, Giles WH, Capewell S. Explaining the decrease in U.S. deaths from coronary disease, 1980-2000. N Engl J Med 2007;356(23):2388-2398.

3. Arialdi M. Miniño MJX, M.D.; and Kenneth D. Kochanek. Deaths: Preliminary Data for 2008. National Vital Statistics Reports Volume;59(2).

4. Mathew L, Evans A, Ouriadov A, Etemad-Rezai R, Fogel R, Santyr G, McCormack DG, Parraga G. Hyperpolarized 3He magnetic resonance imaging of chronic obstructive pulmonary disease: reproducibility at 3.0 tesla. Acad Radiol 2008;15(10):1298-1311.

5. Xu X, Boudreau M, Ouriadov A, Santyr GE. Mapping of 3He Apparent Diffusion Coefficient Anisotropy at Sub-millisecond Diffusion Times in an Elastase-Instilled Rat Model of Emphysema. Magnetic Resonance in Medicine 2011;*In Press*.

6. Weibel ER. Fractal geometry: a design principle for living organisms. Am J Physiol 1991;261(6 Pt 1):L361-369.

7. West JB. Respiratory physiology : the essentials. Philadelphia: Lippincott Williams & Wilkins; 2008. iv, 186 p. p.

8. Ochs M, Nyengaard JR, Jung A, Knudsen L, Voigt M, Wahlers T, Richter J, Gundersen HJ. The number of alveoli in the human lung. Am J Respir Crit Care Med 2004;169(1):120-124.

9. Weibel ER. What makes a good lung? Swiss Med Wkly 2009;139(27-28):375-386.

10. West JB. Pulmonary pathophysiology : the essentials. Philadelphia: Wolters Kluwer Health/Lippincott Williams & Wilkins; 2008. vii, 199 p. p.

11. Barnes PJ. Chronic obstructive pulmonary disease. N Engl J Med 2000;343(4):269-280.

12. Stevenson CS, Docx C, Webster R, Battram C, Hynx D, Giddings J, Cooper PR, Chakravarty P, Rahman I, Marwick JA, Kirkham PA, Charman C, Richardson DL, Nirmala NR, Whittaker P, Butler K. Comprehensive gene expression profiling of rat lung reveals distinct acute and chronic responses to cigarette smoke inhalation. Am J Physiol Lung Cell Mol Physiol 2007;293(5):L1183-1193.

13. Leco KJ, Waterhouse P, Sanchez OH, Gowing KL, Poole AR, Wakeham A, Mak TW, Khokha R. Spontaneous air space enlargement in the lungs of mice lacking tissue inhibitor of metalloproteinases-3 (TIMP-3). J Clin Invest 2001;108(6):817-829.

14. Rangasamy T, Cho CY, Thimmulappa RK, Zhen L, Srisuma SS, Kensler TW, Yamamoto M, Petrache I, Tuder RM, Biswal S. Genetic ablation of Nrf2 enhances susceptibility to cigarette smoke-induced emphysema in mice. J Clin Invest 2004;114(9):1248-1259.

15. Zheng T, Zhu Z, Wang Z, Homer RJ, Ma B, Riese RJ, Jr., Chapman HA, Jr., Shapiro SD, Elias JA. Inducible targeting of IL-13 to the adult lung causes matrix metalloproteinase- and cathepsin-dependent emphysema. J Clin Invest 2000;106(9):1081-1093.

16. Peces-Barba G, Ruiz-Cabello J, Cremillieux Y, Rodriguez I, Dupuich D, Callot V, Ortega M, Rubio Arbo ML, Cortijo M, Gonzalez-Mangado N. Helium-3 MRI diffusion coefficient: correlation to morphometry in a model of mild emphysema. European Respiratory Journal 2003;22(1):14-19.

17. American Thoracic Society. Single-breath carbon monoxide diffusing capacity (transfer factor). Recommendations for a standard technique--1995 update. Am J Respir Crit Care Med 1995;152(6 Pt 1):2185-2198.

18. Saydain G, Beck KC, Decker PA, Cowl CT, Scanlon PD. Clinical significance of elevated diffusing capacity. Chest 2004;125(2):446-452.

19. Dias RM, Chacur FH, Carvalho SR, Neves DD. Which functional parameters can help differentiate severe asthma from COPD? Rev Port Pneumol 2010;16(2):253-272.

20. Friedman PJ. Imaging studies in emphysema. Proc Am Thorac Soc 2008;5(4):494-500.

21. Turner MO, Mayo JR, Muller NL, Schulzer M, FitzGerald JM. The value of thoracic computed tomography scans in clinical diagnosis: a prospective study. Can Respir J 2006;13(6):311-316.

22. Madani A, Zanen J, de Maertelaer V, Gevenois PA. Pulmonary emphysema: objective quantification at multi-detector row CT--comparison with macroscopic and microscopic morphometry. Radiology 2006;238(3):1036-1043.

23. Chae EJ, Seo JB, Lee J, Kim N, Goo HW, Lee HJ, Lee CW, Ra SW, Oh YM, Cho YS. Xenon ventilation imaging using dual-energy computed tomography in asthmatics: initial experience. Invest Radiol 2010;45(6):354-361.

24. Brenner DJ, Hall EJ. Computed tomography--an increasing source of radiation exposure. N Engl J Med 2007;357(22):2277-2284.

25. Kagna O, Solomonov A, Keidar Z, Bar-Shalom R, Fruchter O, Yigla M, Israel O, Guralnik L. The value of FDG-PET/CT in assessing single pulmonary nodules in patients at high risk of lung cancer. Eur J Nucl Med Mol Imaging 2009;36(6):997-1004.

26. Petersson J, Sanchez-Crespo A, Rohdin M, Montmerle S, Nyren S, Jacobsson H, Larsson SA, Lindahl SG, Linnarsson D, Glenny RW, Mure M. Physiological evaluation of a new quantitative SPECT method measuring regional ventilation and perfusion. J Appl Physiol 2004;96(3):1127-1136.

27. Pellegrino R, Biggi A, Papaleo A, Camuzzini G, Rodarte JR, Brusasco V. Regional expiratory flow limitation studied with Technegas in asthma. J Appl Physiol 2001;91(5):2190-2198.

28. Bajc M, Olsson B, Palmer J, Jonson B. Ventilation/Perfusion SPECT for diagnostics of pulmonary embolism in clinical practice. J Intern Med 2008;264(4):379-387.

29. Harris B, Bailey DL, Chicco P, Bailey EA, Roach PJ, King GG. Objective analysis of whole lung and lobar ventilation/perfusion relationships in pulmonary embolism. Clin Physiol Funct Imaging 2008;28(1):14-26.

30. Nagao M, Murase K, Ichiki T, Sakai S, Yasuhara Y, Ikezoe J. Quantitative analysis of technegas SPECT: evaluation of regional severity of emphysema. J Nucl Med 2000;41(4):590-595.

31. Suga K, Kawakami Y, Koike H, Iwanaga H, Tokuda O, Okada M, Matsunaga N. Lung ventilation-perfusion imbalance in pulmonary emphysema: assessment with automated V/Q quotient SPECT. Ann Nucl Med 2010;24(4):269-277.

32. Kernstine KH, Grannis FW, Jr., Rotter AJ. Is there a role for PET in the evaluation of subcentimeter pulmonary nodules? Semin Thorac Cardiovasc Surg 2005;17(2):110-114.

33. Edelman RR, Hatabu H, Tadamura E, Li W, Prasad PV. Noninvasive assessment of regional ventilation in the human lung using oxygen-enhanced magnetic resonance imaging. Nat Med 1996;2(11):1236-1239.

34. Zapke M, Topf HG, Zenker M, Kuth R, Deimling M, Kreisler P, Rauh M, Chefd'hotel C, Geiger B, Rupprecht T. Magnetic resonance lung function--a breakthrough for lung imaging and functional assessment? A phantom study and clinical trial. Respir Res 2006;7:106.

35. Bauman G, Puderbach M, Deimling M, Jellus V, Chefd'hotel C, Dinkel J, Hintze C, Kauczor H-U, Schad LR. Non-contrast-enhanced perfusion and ventilation assessment of the human lung by means of fourier decomposition in proton MRI. Magnetic Resonance in Medicine 2009;62(3):656-664.

36. Albert MS, Cates GD, Driehuys B, Happer W, Saam B, Springer CS, Wishnia A. Biological magnetic resonance imaging using laser-polarized 129Xe. Nature 1994;370(6486):199-201.

37. Möller HE, Chen XJ, Saam B, Hagspiel KD, Johnson GA, Altes TA, de Lange EE, Kauczor H-U. MRI of the lungs using hyperpolarized noble gases. Magnetic Resonance in Medicine 2002;47(6):1029-1051.

38. Tzeng YS, Lutchen K, Albert M. The difference in ventilation heterogeneity between asthmatic and healthy subjects quantified using hyperpolarized He-3 MRI. Journal of Applied Physiology 2009;106(3):813-822.

39. Chen XJ, Möller HE, Chawla MS, Cofer GP, Driehuys B, Hedlund LW, Johnson GA. Spatially resolved measurements of hyperpolarized gas properties in the lung in vivo. Part I: Diffusion coefficient. Magnetic Resonance in Medicine 1999;42(4):721-728.

40. Mansson S, Johansson E, Svensson J, Olsson LE, Stahlberg F, Petersson JS, Golman K. Echo-planar MR imaging of dissolved hyperpolarized 129Xe. Acta Radiol 2002;43(5):455-460.

41. Cleveland ZI, Cofer GP, Metz G, Beaver D, Nouls J, Kaushik SS, Kraft M, Wolber J, Kelly KT, McAdams HP, Driehuys B. Hyperpolarized Xe MR imaging of alveolar gas uptake in humans. PLoS One 2010;5(8):e12192.

42. Patz S, Hersman FW, Muradian I, Hrovat MI, Ruset IC, Ketel S, Jacobson F, Topulos GP, Hatabu H, Butler JP. Hyperpolarized 129Xe MRI: A viable functional lung imaging modality? European Journal of Radiology 2007;64(3):335-344.

43. Kaushik SS, Cleveland ZI, Cofer GP, Metz G, Beaver D, Nouls J, Kraft M, Auffermann W, Wolber J, McAdams HP, Driehuys B. Diffusion-weighted hyperpolarized 129Xe MRI in healthy volunteers and subjects with chronic obstructive pulmonary disease. Magnetic Resonance in Medicine 2011;65(4):1154-1165.

44. Hersman FW, Ruset IC, Ketel S, Muradian I, Covrig SD, Distelbrink J, Porter W, Watt D, Ketel J, Brackett J, Hope A, Patz S. Large Production System for Hyperpolarized 129Xe for Human Lung Imaging Studies. Academic Radiology 2008;15(6):683-692.

45. Ruset IC, Ketel S, Hersman FW. Optical Pumping System Design for Large Production of Hyperpolarized Xe129. Physical Review Letters 2006;96(5):053002.

46. Chen XJ, Moller HE, Chawla MS, Cofer GP, Driehuys B, Hedlund LW, Johnson GA. Spatially resolved measurements of hyperpolarized gas properties in the lung in vivo. Part I: diffusion coefficient. Magn Reson Med 1999;42(4):721-728.

47. Harris RK, Becker ED, de Menezes SMC, Goodfellow R, Granger P. NMR nomenclature: Nuclear spin properties and conventions for chemical shifts - IUPAC recommendations 2001 (Reprinted from Pure Appl. Chem, vol 73, pg 1795-1818, 2001). Solid State Nucl Mag 2002;22(4):458-483.

48. Jackson JD. Classical electrodynamics. New York: Wiley; 1998. xxi, 808 p. p.

49. Goldstein H, Poole CP, Safko JL. Classical mechanics. San Francisco: Addison Wesley; 2002. xviii, 638 p. p.

50. Bloch F. Nuclear Induction. Phys Rev 1946;70(7-8):460.

51. Torrey HC. Bloch Equations with Diffusion Terms. Phys Rev 1956;104(3):563.

52. Yablonskiy DA. Quantitative in vivo assessment of lung microstructure at the alveolar level with hyperpolarized 3He diffusion MRI. Proceedings of the National Academy of Sciences 2002;99(5):3111-3116.

53. Haacke EM. Magnetic resonance imaging : physical principles and sequence design. New York: J. Wiley-Liss; 1999. xxvii, 914 p. p.

54. Walker TG, Happer W. Spin-exchange optical pumping of noble-gas nuclei. Reviews of Modern Physics 1997;69(2):629.

55. Santyr GE, Lam WW, Parra-Robles JM, Taves TM, Ouriadov AV. Hyperpolarized noble gas magnetic resonance imaging of the animal lung: Approaches and applications. Journal of Applied Physics 2009;105(10):102004.

56. Zhao L. Gradient-Echo Imaging Considerations for Hyperpolarized129Xe MR. Journal of Magnetic Resonance, Series B 1996;113(2):179-183.

57. Durand E, Guillot G, Darrasse L, Tastevin G, Nacher PJ, Vignaud A, Vattolo D, Bittoun J. CPMG measurements and ultrafast imaging in human lungs with hyperpolarized helium-3 at low field (0.1 T). Magnetic Resonance in Medicine 2002;47(1):75-81.

58. Dominguez-Viqueira W, Berger W, Parra-Robles J, Santyr GE. Litz Wire Radiofrequency Receive Coils for Hyperpolarized Noble Gas MR Imaging of Rodent Lungs at 73.5 mT. Concept Magn Reson B 2010;37B(2):75-85.

59. Parra-Robles J, Dominguez Viqueira W, Xu X, Ouriadov A, Santyr GE. Theoretical prediction and experimental measurement of the field dependence of the apparent transverse relaxation of hyperpolarized noble gases in lungs. Journal of Magnetic Resonance 2008;192(1):85-91.

60. Parra-Robles J, Cross AR, Santyr GE. Theoretical signal-to-noise ratio and spatial resolution dependence on the magnetic field strength for hyperpolarized noble gas magnetic resonance imaging of human lungs. Medical Physics 2005;32(1):221.

61. Einstein A. Über die von der molekularkinetischen Theorie der Wärme geforderte Bewegung von in ruhenden Flüssigkeiten suspendierten Teilchen. Annalen der Physik 1905;322(8):549-560.

62. Basser PJ, Mattiello J, LeBihan D. Estimation of the effective self-diffusion tensor from the NMR spin echo. J Magn Reson B 1994;103(3):247-254.

63. Basser PJ, Pierpaoli C. Microstructural and physiological features of tissues elucidated by quantitative-diffusion-tensor MRI. J Magn Reson B 1996;111(3):209-219.

Chapter 2

2 Finite Difference ^{129}Xe Diffusion Simulations in the Budded Cylinder Airway Model

2.1 Introduction

Numerical models of the lung provide an invaluable tool for predicting behaviour of hyperpolarized noble gases prior to implementing *in vivo* MRI experiments. Over the past decade, several airway models have been developed for diffusion MRI experiments, typically aiming to predict behavior either at short (1-3) or long (4,5) range diffusion time scales, corresponding to a mean path of a few alveoli or several bronchiole generations, respectively. For short diffusion times, the terminal airways have been modeled as an infinite cylinder (1), and a mathematical analysis of this simple model yields an analytical equation for anisotropic diffusion involving two orthogonal diffusion coefficients: D_L, the diffusion coefficient along the axis of the cylinder, and D_T, the diffusion coefficient perpendicular to this axis. Numerical simulations of gas diffusion in the terminal airways have since been extended to a wide range of structural models (2,3). The budded cylinder model, in which partial spheres representing alveoli are joined to a cylinder representing the terminal airways to model the acinus, has recently emerged as a promising tool for modeling emphysema-like airspace expansion (3) and will be used throughout this chapter.

Most numerical simulations until now have been performed with ^3He as it the most used hyperpolarized gas for *in vivo* experiments, due to its signal advantages. Due to a recent surge in the use of ^{129}Xe for hyperpolarized MRI experiments, it is of interest to re-evaluate ^3He diffusion techniques for ^{129}Xe, specifically to optimize pulse sequence parameters. In particular, the smaller self-diffusion coefficient of ^{129}Xe compared to ^3He implies that optimal diffusion times (where the greatest difference of ADCs between normal and disease is observed) will be much larger for ^{129}Xe experiments than for ^3He.

This chapter was motivated by the recent success of ^{3}He numerical diffusion simulations at predicting optimal diffusion times to quantify alveolar damage in an elastase-instilled rat model of emphysema using the Yablonskiy anisotropic diffusion model (6). This study suggested that D_T provides the best sensitivity to measure alveolar damage in an animal model at ultra-short diffusion times ($\Delta_{opt,\ He}$ = 360 μs). A rough estimation using the results of Ref. (6) for ^{3}He and the ratio of diffusion coefficients ($D_{He}/D_{Xe} \approx 30$) yields an optimal diffusion time on the order of 10 ms for ^{129}Xe. The optimal diffusion times for the measurement of D_L and D_T can be more precisely estimated with finite difference diffusion simulations using the budded-cylinder model, which is the subject of this chapter.

2.2 Method

A finite difference method of solving the Bloch-Torrey equations (Eqn. [2.1], Section 2.2.2) was used to simulate diffusion of transverse magnetization on a spatial grid in the presence of magnetic field gradients (2). The code was written in the C programming language, and run using an Intel® Core™ i7 2.80 GHz QuadCore CPU and 8 GB RAM. The pulsed gradient spin echo experiment with trapezoidal gradients was used for these simulations (Fig. 1.10 of Section 1.4.9). In this figure, G_m is the maximal gradient strength, τ is the ramp up/down time, Δ is the diffusion time and δ is the gradient flat time + 2τ. To simplify the code and to provide consistent pulse sequences for all diffusion times, it is assumed that RF pulses are applied instantaneously and $\Delta = \delta$.

A 92 x 72 x 92 array (x,y,z) was used to simulate a spatial grid with 8.75 μm isotropic spatial step sizes ($\Delta x = \Delta y = \Delta z$). The budded cylinder model of the terminal airways determined the boundary conditions that restricted diffusion (3), and a phase wrapping technique was used to simulate an infinite cylinder by diffusing magnetization from one end of the cylinder to the other. The xenon self-diffusion coefficient was set at 6.1 10^{-6} m^2/s (7). The diffusion times (Δ) simulated were 1, 2, 5, 10, 20 and 100 ms, ranging from when the diffusion coefficient converged to the self diffusion coefficient at low diffusion times to when the mean diffused distance exceeded several alveoli and the model would require a branching structure that better reflects lung anatomy. The b-values (Eqn. [1.40] in Section 1.4.9 for the pulse sequence shown in Fig. 1.10) ranged from 3 to 24 s/cm^2 at 3 s/cm^2 intervals, and were limited to this range due to constraints in computation time due to convergence conditions on the maximal gradient strength applicable for set spatial step sizes (Section 2.2.3).

2.2.1 Budded cylinder model

The budded cylinder model used for these simulations was introduced by Fichele *et al* (3), and is shown in Fig. 2.1. Two sets of four spheres representing alveoli are attached to a cylinder for a more realistic model of the acinus than the simple cylinder model. The spheres from each set were separated by 90° relative to the center of the cylinder, and one set of four spheres was rotated by 45° degrees relative to the other set. Both sets of spheres were separated by a distance $2L_A$ = 320 μm. The radius of the spheres (R_A) was set at 140 μm and the relative distance between the center of the cylinder and the center of the spheres (R) was set at 210 μm. To model airspace expansion characteristic of emphysema, the radius of the cylinder R_D was varied depending on disease severity to simulate erosion of the airways. The severity of the disease was interpreted using the ratio $R_D/(R+R_A)$, where a ratio of 0.55 has previously been shown to simulate normal airways (3), and $R_D/(R+R_A)$ = 0.8 represents emphysema-like destruction. In accordance to these values, "Healthy" tissue was represented by a cylinder radius R_D of 193 μm, and "Diseased" tissue by a value of 280 μm. Although Fichele *et al.* modeled these airway sizes as a model based on emphysematous changes observed in human terminal airways, a recent study (6) has shown that these parameters provided a good prediction of changes in ^{3}He anisotropic ADC at different diffusion times for damage induced by 75 IU of elastase in rats, six to eight weeks post-instillation. As such, this work assumes that these parameters are a good approximation for the purpose of ^{129}Xe ADC measurements in this same animal model.

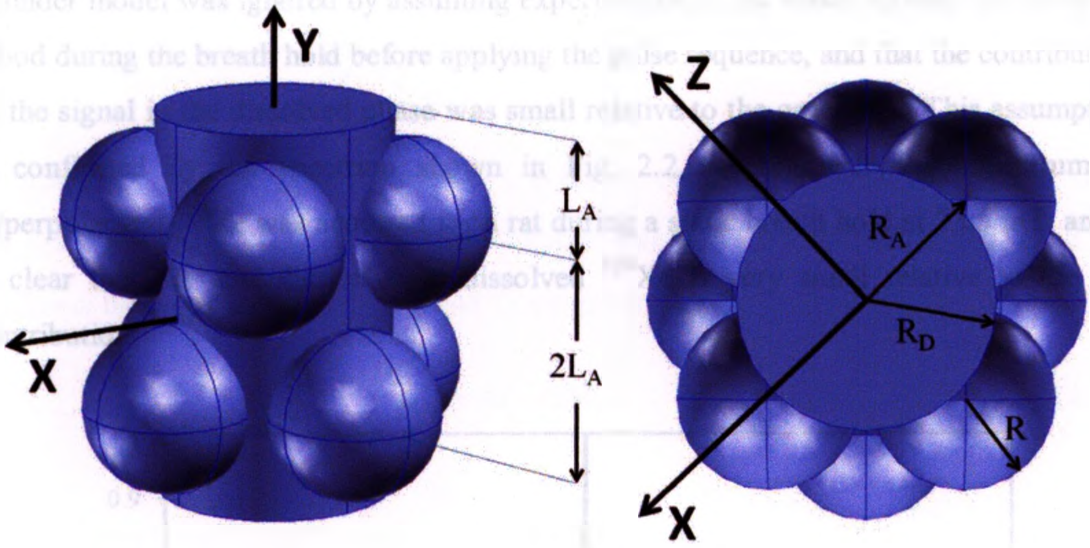

Figure 2.1. Budded cylinder model of the terminal airways, showing a side view (left) and end view (right).

2.2.2 Finite Difference Method of Solving the Bloch-Torrey Equations

A finite difference approach was used to numerically solve the Bloch-Torrey differential equations for transverse magnetization (2,3) for a pulsed gradient spin echo (PGSE) experiment (Fig. 1.10, Section 1.4.9). In order to simplify the calculations, several assumptions were made for these simulations. No signal decay was present in the absence of magnetic gradients, reflecting that T_1 relaxation was ignored by simulating only the transverse magnetization and assuming that perfect 90° and 180° pulses were applied. This also reflects that T_2 relaxation effects were ignored, as experimentally, T_2 relaxation is accounted for in a two acquisition experiment: (i) an experiment with applied gradients (b-value + T_2 decay) and (ii) an experiment without applied pulsed gradients (T_2 decay). The echo measured with applied gradients on is thus normalized by the echo measured without. No bulk flow of gas was present in these simulations, which is equivalent to assuming a static breath hold,. Magnetic field inhomogeneities (other than the applied gradients) were also ignored. Prior to applying the gradients, the magnitude and phase of the transverse magnetization was homogeneous. Boundary permeability of the budded cylinder model was ignored by assuming experimentally that xenon already saturated the blood during the breath hold before applying the pulse sequence, and that the contribution of the signal in the dissolved phase was small relative to the gas signal. This assumption is confirmed by the spectrum shown in Fig. 2.2, where an *in vivo* spectrum of hyperpolarized ^{129}Xe was acquired for a rat during a static breath hold at 73.5 mT, and it is clear that the contribution from dissolved ^{129}Xe is very small relative to the gas contribution.

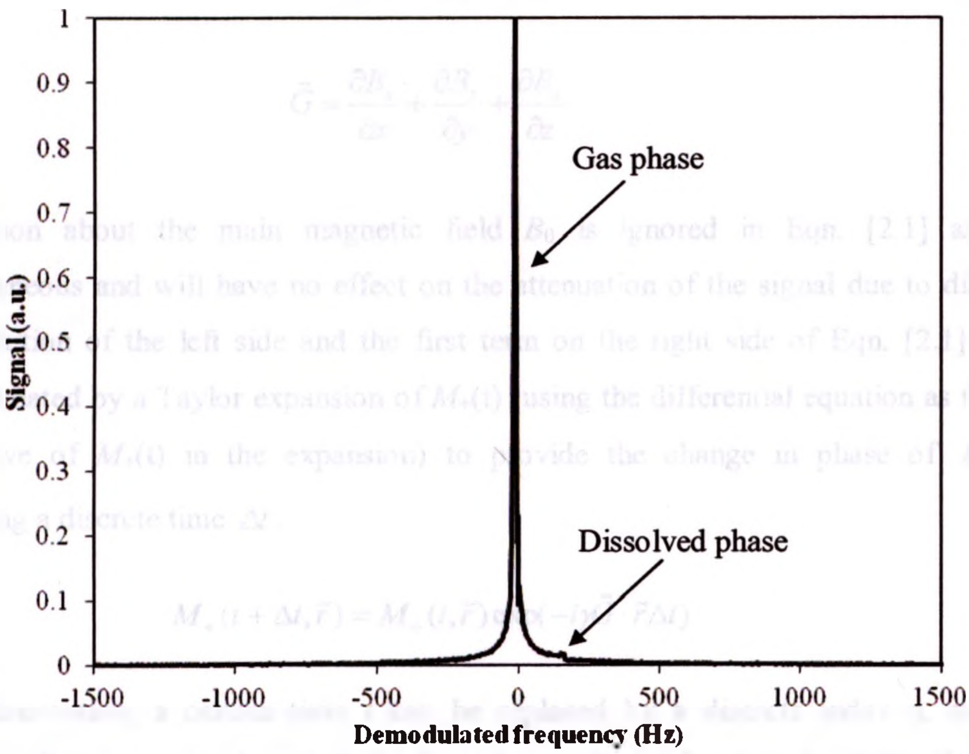

Figure 2.2. Experimental *in vivo* spectra of hyperpolarized ^{129}Xe at 73.5 mT for a rat during a static breath hold. Due to its relatively low abundance compared to ^{129}Xe in the gas phase, the dissolved phase is ignored for these simulations.

The differential equation for transverse magnetization of particles diffusing in an external magnetic field gradient can be expressed by the following modified Bloch-Torrey equations (8):

$$\frac{\partial M_+}{\partial t} = -i\gamma M_+ \vec{G} \cdot \vec{r} + D\nabla^2 M_+ \quad [2.1]$$

In Eqn. [2.1], $\vec{r}$ is the spatial position, γ is the gyromagnetic ratio of the nucleus, D is the diffusion coefficient, M_+ is the complex transverse magnetization and $\vec{G}$ is the magnetic field gradient, where M_+ and $\vec{G}$ are given by Eqn. [2.2] and [2.3]:

$$M_+ = M_x + iM_y \quad [2.2]$$

$$\vec{G} = \frac{\partial B_z}{\partial x} + \frac{\partial B_z}{\partial y} + \frac{\partial B_z}{\partial z} \quad [2.3]$$

Precession about the main magnetic field B_0 is ignored in Eqn. [2.1] as B_0 is homogeneous and will have no effect on the attenuation of the signal due to diffusion. The solution of the left side and the first term on the right side of Eqn. [2.1] can be approximated by a Taylor expansion of $M_+(t)$ (using the differential equation as the time derivative of $M_+(t)$ in the expansion) to provide the change in phase of $M_+(t,\vec{r})$ following a discrete time Δt.

$$M_+(t + \Delta t, \vec{r}) = M_+(t, \vec{r}) \exp(-i\gamma \vec{G} \cdot \vec{r} \Delta t) \quad [2.4]$$

As a convention, a certain time t can be replaced by a discrete index n, and it is understood that $t = n\,\Delta t$ where Δt is the finite temporal step duration. Similarly, the spatial coordinates (x,y,z) can be replaced by the discrete indices (i,j,k) such that (x,y,z) = (i Δx, j Δy, k Δz), where Δx, Δy and Δz are the finite spatial step sizes of the computation. Using this convention, the second term of Eqn. [2.1] was calculated by a finite difference approximation of the temporal and spatial derivative which yielded the following recursive equation, and added to Eqn. 2.4 (not shown below):

$$M^{n+1}_{+(i,j,k)} = M^{n}_{+(i,j,k)} + \frac{\Delta t}{\Delta x^2} D_{i,i-1}\left[M^{n}_{+(i-1,j,k)} - M^{n}_{+(i,j,k)}\right] + \frac{\Delta t}{\Delta x^2} D_{i,i+1}\left[M^{n}_{+(i+1,j,k)} - M^{n}_{+(i,j,k)}\right] + \frac{\Delta t}{\Delta y^2} D_{j,j-1}\left[M^{n}_{+(i,j-1,k)} - M^{n}_{+(i,j,k)}\right] + \frac{\Delta t}{\Delta y^2} D_{j,j+1}\left[M^{n}_{+(i,j+1,k)} - M^{n}_{+(i,j,k)}\right] + \frac{\Delta t}{\Delta z^2} D_{k,k-1}\left[M^{n}_{+(i,j,k-1)} - M^{n}_{+(i,j,k)}\right] + \frac{\Delta t}{\Delta z^2} D_{k,k+1}\left[M^{n}_{+(i,j,k+1)} - M^{n}_{+(i,j,k)}\right] \quad [2.5]$$

where $D_{i,i-1}$ is the diffusion coefficient between the i and i-1 grid positions. Signal was then defined as magnitude of the complex sum of the magnetization of each grid position: S_o being the initial signal and S being the signal after the second gradient is applied. The diffusion coefficients are used to set the boundary conditions described in Section 2.2.1 by setting them zero at the airway and alveolar walls, and defining them to be the self-diffusion coefficient of the nuclei everywhere inside the airway (Fig. 2.3).

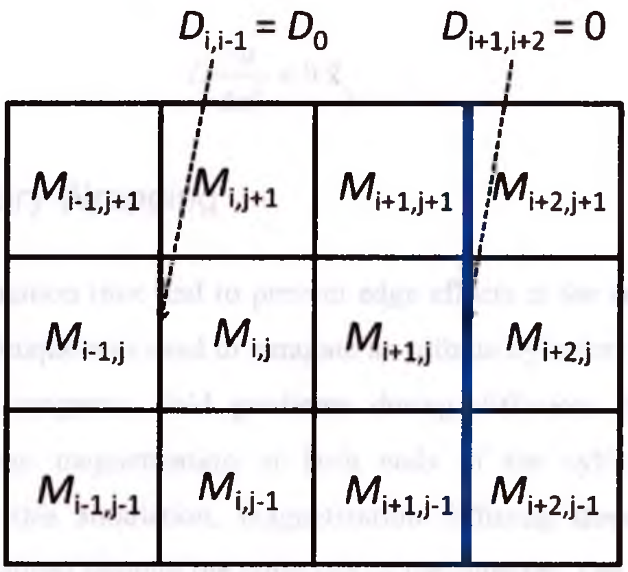

Figure 2.3. A two dimensional representation of the computational grid used to numerically calculate Eqn. [2.5]. The blue line represents an impermeable barrier.

For *in vivo* MRI experiments, each imaging voxel contains hundreds of randomly oriented alveoli. To simulate random orientation of airways in a voxel, the pulsed trapezoidal gradients were applied in 30 different orientations ($\theta_m = m\pi/30$ radians where m=1, 2, 3, ... , 30) relative to the cylinder (Eqn. [2.6]) and reconstructed during the data analysis:

$$\vec{G} = G\sin(\theta_m)\hat{x} + G\cos(\theta_m)\hat{y} \qquad [2.6]$$

2.2.3 Convergence

The spatial steps sizes (Δx, Δy and Δz) satisfied the Nyquist criterion to ensure the convergence of the simulations. Specifically, to achieve less than 1% error, the following condition was always satisfied (2):

$$\Delta x < \frac{\pi}{10\gamma G_x \delta}. \qquad [2.7]$$

In addition, the temporal step size (Δt) satisfied the following condition to ensure stability of the simulations:

$$D\frac{\Delta t}{\Delta x^2} < 0.2 \qquad [2.8]$$

2.2.4 Boundary Wrapping

To minimize computation time and to prevent edge effects at the ends of the cylinder, a phase wrapping technique was used to simulate an infinite cylinder. Due to the history of the applied spatial magnetic field gradients during diffusion, there exists a phase discontinuity between magnetization at both ends of the cylinder which must be accounted for. For this simulation, magnetization diffusing through one end of the cylinder was reintroduced through the other end of the cylinder. The phase difference:

$$\varphi_y = \gamma \Delta y N_y \int_0^t G_y(t')dt' \qquad [2.9]$$

was added to magnetization diffusing out of elements where $G_y y < 0$, and subtracted from magnetization diffusing out of elements where $G_y y > 0$.

2.2.5 Data Analysis

For each diffusion time (Δ), echo signals (S) were normalized to the initial signal (S_0) for each gradient orientation θ_m. Assuming that the budded cylinders are isotropically distributed (in three dimensions) in every voxel, normalized echoes for each gradient orientations are weighted by the distribution function $\sin(\theta_m)$ and the mean normalized signal (for a certain diffusion time and b-value) is:

$$\frac{S}{S_0} = \frac{\sum_m \frac{S}{S_0}(\theta_m)\sin(\theta_m)}{\sum_m \sin(\theta_m)} \quad [2.10]$$

Normalized echoes were calculated for each b-value, and the Yablonskiy anisotropic diffusion equation (Eqn. [1.53], (1) was fitted to the data for each diffusion time using a non-linear least squares Matlab function (lsqcurvefit.m, The Mathworks, Natick, MA) to extract the longitudinal and transverse diffusion coefficients (D_L and D_T).

2.3 Results and Discussion

Figures 2.4 a) and b) show the simulated dependence of anisotropic diffusion coefficients (D_L and D_T) on Δ for the budded cylinder models of healthy and diseased airways. Figures 2 c) and d) show the differences in the diffusion coefficients (ΔD_L and ΔD_T) between diseased and healthy airways for D_L and D_T respectively.

For the simulated diffusion times, the largest increase of D_T between the healthy and disease model occurs at $\Delta = 5$ ms (159% increase), and the largest increase of D_L occurs at $\Delta = 50$ ms (53% increase). These results show that D_T is predicted to have greater sensitivity than D_L for measuring emphysema with xenon in this model, agreeing with what was observed in a previous study (6) for ^{3}He, both theoretically and experimentally. As expected, both D_L and D_T converge toward the self-diffusion coefficient of xenon at short diffusion times, and D_L follows the same general trend previously observed for ^{3}He ADC in the cylinder model (Fig. 4 of (2)).

As a result of these simulations, the *in vivo* experiments described in Chapter 3 used Δ = 6, 50 and 100 ms (the use of 6 ms instead of 5 ms was due to hardware limitations).

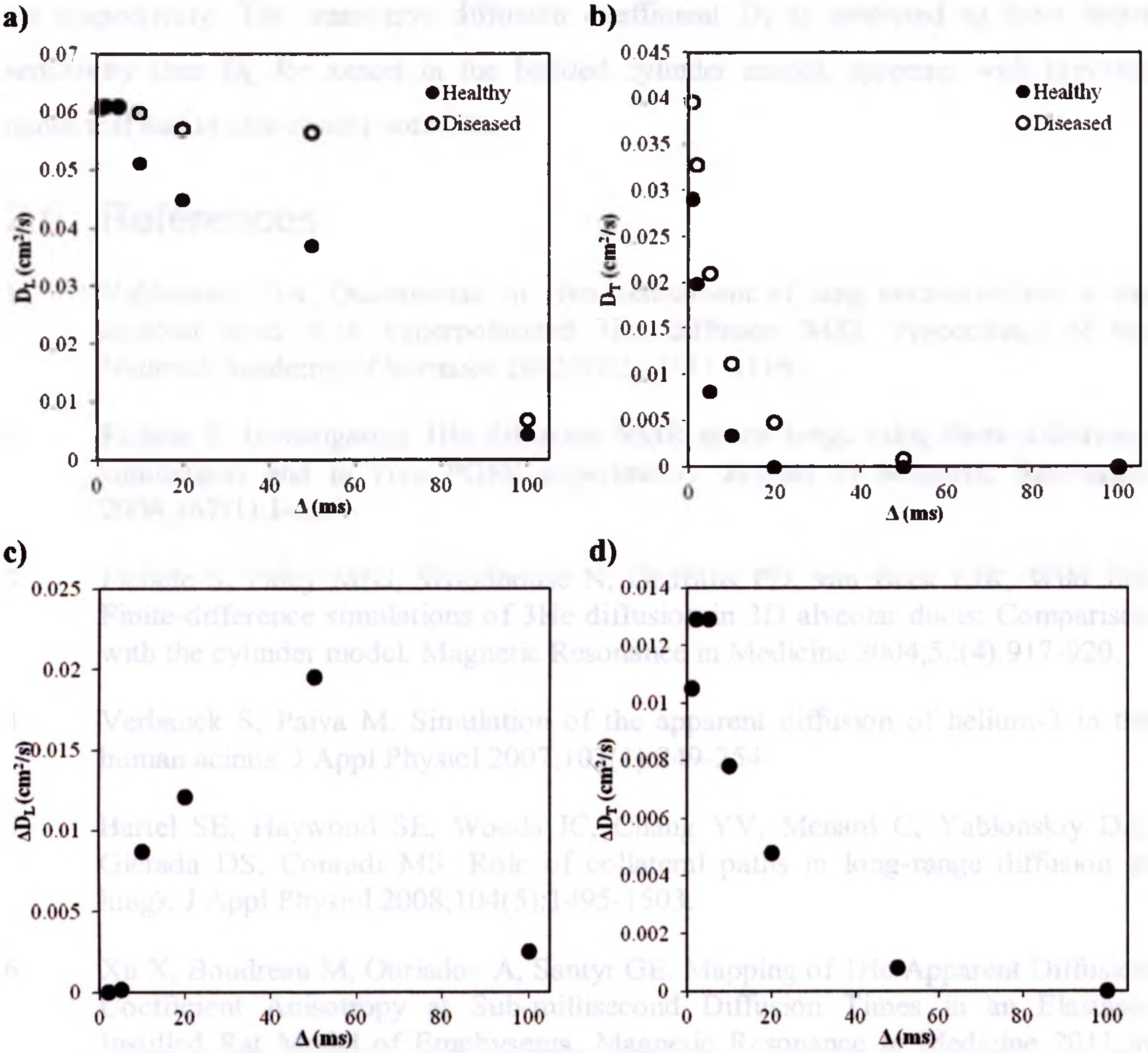

Figure 2.4. Longitudinal (a) and transverse (b) diffusion coefficients extracted from diffusion simulations in a budded cylinder model of the terminal airways. "Healthy" corresponds to R_D = 193 µm; "Diseased" to R_D = 280 µm. The difference in diffusion coefficients between "Diseased" and "Healthy" airways for longitudinal and transverse diffusion coefficients are shown in (c) and (d) respectively.

2.4 Conclusion

This chapter provided an estimation of the optimal diffusion time Δ to investigate alveolar enlargement and destruction with anisotropic diffusion coefficients D_L and D_T by simulating xenon gas diffusion in the budded cylinder model. D_L and D_T are predicted for xenon to have optimal sensitivity to destructive alveolar diseases near $\Delta = 50$ ms and 5 ms respectively. The transverse diffusion coefficient D_T is predicted to have better sensitivity than D_L for xenon in the budded cylinder model, agreeing with previous numerical and *in vivo* results with ^{3}He.

2.5 References

1. Yablonskiy DA. Quantitative in vivo assessment of lung microstructure at the alveolar level with hyperpolarized 3He diffusion MRI. Proceedings of the National Academy of Sciences 2002;99(5):3111-3116.
2. Fichele S. Investigating 3He diffusion NMR in the lungs using finite difference simulations and in vivo PGSE experiments. Journal of Magnetic Resonance 2004;167(1):1-11.
3. Fichele S, Paley MNJ, Woodhouse N, Griffiths PD, van Beek EJR, Wild JM. Finite-difference simulations of 3He diffusion in 3D alveolar ducts: Comparison with the cylinder model. Magnetic Resonance in Medicine 2004;52(4):917-920.
4. Verbanck S, Paiva M. Simulation of the apparent diffusion of helium-3 in the human acinus. J Appl Physiol 2007;103(1):249-254.
5. Bartel SE, Haywood SE, Woods JC, Chang YV, Menard C, Yablonskiy DA, Gierada DS, Conradi MS. Role of collateral paths in long-range diffusion in lungs. J Appl Physiol 2008;104(5):1495-1503.
6. Xu X, Boudreau M, Ouriadov A, Santyr GE. Mapping of 3He Apparent Diffusion Coefficient Anisotropy at Sub-millisecond Diffusion Times in an Elastase-Instilled Rat Model of Emphysema. Magnetic Resonance in Medicine 2011;*In Press*.
7. Chen XJ, Moller HE, Chawla MS, Cofer GP, Driehuys B, Hedlund LW, Johnson GA. Spatially resolved measurements of hyperpolarized gas properties in the lung in vivo. Part I: diffusion coefficient. Magn Reson Med 1999;42(4):721-728.
8. Stejskal EO, Tanner JE. Spin Diffusion Measurements: Spin Echoes in the Presence of a Time-Dependent Field Gradient. Journal of Chemical Physics 1965;42(1):288-.

Chapter 3

3 Measurement of 129Xe Gas Apparent Diffusion Coefficient Anisotropy in an Elastase-Instilled Rat Model of Emphysema

3.1 Introduction

Hyperpolarized magnetic resonance imaging (MRI) is an emerging modality for quantifying anatomical and functional characteristics of the lung *in vivo* (1). Hyperpolarized MRI studies have to date focused mainly on ^{3}He due to its large gyromagnetic ratio, maximizing the signal achievable per volume of gas compared to other nuclei which can be hyperpolarized (eg. ^{129}Xe, ^{13}C). ^{3}He ventilation maps have proven to be a useful tool for investigating asthma (2,3) and chronic obstructive disease (4,5). In addition, by measuring the T_1 and T_2 relaxation of hyperpolarized gases in the lungs, regional alveolar oxygen partial pressure can be quantified (6-8). Microstructural changes in the terminal airways can be detected by measuring the apparent diffusion coefficient (ADC) of ^{3}He (9), which is smaller than the self diffusion coefficient of ^{3}He due to restrictive diffusion in the lung. An increase in ^{3}He ADC is observable in chronic obstructive lung disease (COPD) (4,10-12) due to airway tissue expansion and alveolar destruction (ie. emphysema), and correlates well with histological measurements, such as mean linear intercept; an indication of alveolar destruction (11,13). Furthermore, ^{3}He ADC due to emphysema can be anisotropic (14), and depends on the duration of observation during which the nuclei diffuse in the restricted environment (ie. the diffusion time) (15).

Recently, the hyperpolarized MRI research community has shifted towards ^{129}Xe (16) due to its higher natural abundance than ^{3}He, as well as recent improvements in hyperpolarization and delivery of ^{129}Xe (17,18). Recent clinical studies (19,20) have shown that ^{129}Xe MRI can provide similar diagnostic information compared to ^{3}He techniques, particularly ventilation defects and ADC. However, more work is needed in order to identify the key differences in studying both nuclei and how to adapt and optimize established ^{3}He techniques to ^{129}Xe. One important difference is that ^{129}Xe is much more soluble in blood than ^{3}He (21), leading to the possibility of investigating xenon gas exchange *in vivo* (22-24). In addition, ^{129}Xe has a self diffusion coefficient approximately 30 times smaller than ^{3}He (9), which implies that ADC studies using ^{129}Xe will likely need to employ considerably longer diffusion times than for ^{3}He to probe similar alveolar dimensions.

The root mean square r_{rms} distance that a particle diffuses to due to Brownian motion over time in an unrestricted environment is:

$$r_{rms} = \sqrt{6D_0 \cdot \Delta} \qquad [3.1]$$

where D_0 is the self diffusion coefficient and Δ is the diffusion time. The effects of long diffusion times (greater than 5 ms) on ADC in lungs have been studied with clinical MRI systems using ^{3}He, but special pulse sequence approaches such as stimulated echoes (25,26) and magnetization tagging (27) are often required due to low T_2^* in the airspaces, and significant signal penalties are associated with these techniques. An emerging approach to this problem is to use low field magnetic fields (28,29), since hyperpolarized magnetization is independent of the field strength of the MRI system. The SNR of hyperpolarized MRI in lungs has been predicted to be optimal at magnetic field strengths of about 0.1 T (30). This approach potentially makes better use of the available signal since a pulsed-gradient spin echo (PGSE) technique may be used to investigate a wider range of diffusion times, by taking advantage of a much longer T_2 and T_2^* due to reduced air-tissue susceptibility differences at low magnetic field strength (31,32).

Diffusion at short length scales (on the order of a few alveoli) has been shown analytically (14) and numerically (33,34) to have an anisotropic behavior due to the cylinder-like morphology of the terminal airways. Anisotropic ADC in a cylindrical geometry can be described by two components (35): D_L, the longitudinal diffusion coefficient along the main axis of the cylinder, and D_T, the transverse diffusion coefficient perpendicular to this axis. Diffusion studies at these length scales have the potential for detecting early onset of emphysema as well as quantifying sub-voxel terminal airway dimensions, such as the airway radius and alveolar diameters (14,36,37).

A recent study has shown in an elastase-induced rat model of emphysema that ^{3}He D_T at sub-millisecond diffusion times was more sensitive than D_L for quantifying alveolar destruction (15), suggesting that D_T measurements may be an important indicator of emphysema-induced alveolar destruction.

The aims of this study were to investigate theoretically the dependence of ^{129}Xe anisotropy (D_L and D_T) on diffusion time in a budded cylinder model and to validate using whole lung D_L and D_T measurements obtained with a PGSE approach at a magnetic field strength of 73.5 mT (29) in sham-instilled rats and an elastase-instilled rat model of emphysema (11). The results are correlated with mean linear intercept measurements obtained from lung histology. The optimal diffusion times and choice of D_L or D_T required to best distinguish elastase-instilled changes in this rat model of emphysema with xenon and implications for clinical applications are discussed.

3.2 Method

3.2.1 Numerical Simulations

A finite difference approach implemented in the C programming language was used to numerically solve the Bloch-Torrey equations for transverse magnetization (33,34).

A 92x72x92 grid was constructed using 8.75 μm isotropic spatial step sizes. Pulsed trapezoidal gradients separated by a 180 degree pulse (Fig. 3.1, $\Delta=\delta$) were applied in 30 different orientations relative to the cylinder ($\pi/30$ to π rad) to simulate random orientation of airways in a voxel. A phase wrapping boundary technique was used to simulate an infinite cylinder.

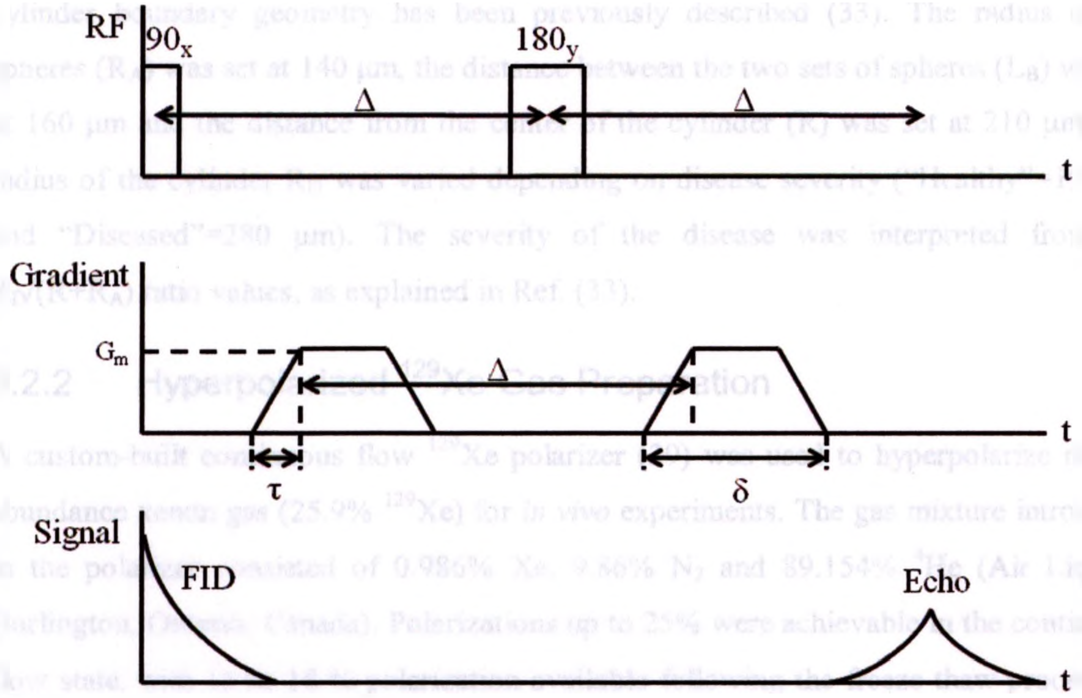

Figure 3.1 Pulse gradient spin echo pulse sequence using trapezoidal gradients. G_m is the maximal gradient strength, τ is the ramp up/down time, Δ is the diffusion time and δ is the gradient flat time + 2 τ.

The xenon self-diffusion coefficient was set to 6.1 x 10^{-6} m^2/s (9). Diffusion times (Δ) from 1 to 100 ms were used, ranging from when the diffusion coefficient converged to the self diffusion coefficient at low diffusion times to when the mean diffused distance exceeded several alveoli, where the model would require a branching structure to better model the airways. b-values (for the pulse sequence shown in Fig. 3.1) were calculated using the following equation and ranged from 3 to 24 s/cm^2, and were limited to this range due to constraints in computation time due to convergence conditions on the maximal gradient strength useable for set spatial step sizes (34):

$$b = (\gamma G_m)^2 \left[\delta^2 \left(\Delta - \frac{\delta}{3} \right) + \tau \left(\delta^2 - 2\Delta\delta + \Delta\tau - \frac{7}{6}\delta\tau + \frac{8}{15}\tau^2 \right) \right] \quad [3.2]$$

where γ is the gyromagnetic ratio, G_m is the maximal gradient strength, τ is the ramp up/down time, Δ is the diffusion time and δ is the gradient flat time + 2τ. The budded cylinder boundary geometry has been previously described (33). The radius of the spheres (R_A) was set at 140 µm, the distance between the two sets of spheres (L_B) was set at 160 µm and the distance from the center of the cylinder (R) was set at 210 µm. The radius of the cylinder R_D was varied depending on disease severity ("Healthy"=193 µm and "Diseased"=280 µm). The severity of the disease was interpreted from the $R_D/(R+R_A)$ ratio values, as explained in Ref. (33).

3.2.2 Hyperpolarized ^{129}Xe Gas Preparation

A custom-built continuous flow ^{129}Xe polarizer (29) was used to hyperpolarize natural abundance xenon gas (25.9% ^{129}Xe) for *in vivo* experiments. The gas mixture introduced in the polarizer consisted of 0.986% Xe, 9.86% N_2 and 89.154% ^{4}He (Air Liquide, Burlington, Ontario, Canada). Polarizations up to 25% were achievable in the continuous flow state, with 16 to 18 % polarization available following the freeze-thaw process for extracting xenon from the gas mixture.

The gas flowed through the gas lines at a rate of 0.40 ± 0.03 L/min and at a pressure of 30.0 ± 1.0 PSI. Water (Supelco, Bellefonte, USA) and O_2 (Chromatography Research Supplies, Louisville, USA) filters are used to remove any residual O_2 from the lines before contact with the rubidium. Rubidium atoms were vaporized from a glass trap heated to 330 ± 30 °C and flowed into an optical cell (220 ± 10 °C). A 60 W dual beam, circularly polarized 795 nm laser beam (Coherent Inc., Santa Clara, CA, USA) was focused on the center of the optical cell, which rests in the center of a 50 Gauss solenoid coil. At the exit of the polarizer, rubidium atoms were removed with a glass wool filter.

Xenon was extracted from the gas by freezing it in a glass trap using liquid N_2 while the residual gases flowed through, and was thawed after the required quantity of xenon was collected. A 5-turn linear horizontal glass trap was used to accumulate the frozen xenon. The trap was placed in an insulated foam liquid nitrogen bath. The liquid nitrogen level was raised at equal time intervals to cover each layer of the trap sequentially, ensuring thin xenon layers. The trap was then vacuumed to remove any residual gases and placed in a bath of boiling water, thawing the xenon into a Tedlar bag (Jensen Inert, Coral

Springs, USA). Typical collection times of 1 hour yielded 220-240 ml of hyperpolarized xenon.

3.2.3 Animal Preparation

This study was approved by the University of Western Ontario Council on Animal Care. (Appendix A)

3.2.3.1 Elastase Instillation

Nine male Wistar rats (264 ± 30 g, Charles River Laboratories, Saint-Constant, Canada) were initially anesthetized with 5.0% Isoflurane (Abbott Laboratories, Saint-Laurent, Canada) through a nose cone with a vaporizer (VetEquip, Pleasanton, CA). Lacrilube® (Allergan Inc, Marckham, Canada) was applied gently to both eyes to reduce the effects of dehydration. Intraperitoneal injections were performed at doses of 1 mL/kg of 4:2 Ketamine (Bioniche Animal Healthy, Belleville, Canada) and Xylazine (Rompun®, Bayer Healthcare, Toronto, Canada). Two drops of Lidocaine (Alveda, Toronto, Canada) were placed on the larynx two minutes before insertion of a 16 G endotracheal tube (Becton Dickinson, Franklin Lakes, NJ). Four rats were instilled with 75 IU of porcine elastase stock (Elastin Products Company, Owensville, MO) mixed at a concentration of 175 IU/ml in saline (11). The remaining rats were sham-instilled with 0.43 ml of saline. The rats were gently rotated to evenly distribute the instilled liquid in the lungs. Physiological and behavioral characteristics of the rats, such as respiratory rate, colour and posture, were monitored for 48 hours following this procedure, and no adverse reactions were observed. Experiments are performed 6-8 weeks post-instillation to allow sufficient alveolar damage to occur due to the breakdown of down elastin by the elastase-instillation (15).

3.2.3.2 Surgical Procedure

Nine male Wistar rats (479 ± 32 g, Charles River Laboratories, Saint-Constant, Canada) were initially anesthetized with 5.0 % Isofluorane (Baxter Corporation, Mississauga, Canada) through a nosecone using a vaporizer (VetEquip, Pleasanton, CA), reduced to 3.0 % once the animal was stable. Lacrilube® (Allergan Inc, Marckham, Canada) was applied gently to both eyes to reduce the effect of dehydration, and 5 IU of glycopyrrolate (Sandoz, Quebec, Canada) was injected subcutaneously to reduce tracheobronchial secretions. Rats remained anesthetized by intravenous administration of a 10:1 Propofol (AstraZeneca, Mississauga, Canada) and Ketamine (Bioniche Animal Health, Belleville, Canada) mix intravenously at a rate of 45-60 mg/g/h. Two drops of Lidocaine (Alveda, Toronto, Canada) were placed on the larynx and, after two minutes, the rat was intubated with an 18 G endotracheal tube (Becton Dickinson, Franklin Lakes, NJ). 5 IU of Sensorcaine® (AstraZeneca, Mississauga, Canada) was injected subcutaneously in the neck, and the trachea was then exposed through a 2 cm incision. The trachea was tied tightly around the endotracheal tube using 3 loops of 0-silk suture (Johnson & Johnson, Ethicon, New Brunswick, NJ), ensuring an air-tight seal, and the skin was sutured closed. A custom ventilator (GEHC, Malmo, Sweden) was used to ventilate the animals with medical air at a rate of 60 breaths per minute in the supine position, as well as providing breaths and breath holds of hyperpolarized xenon (Appendix B, (38)). The peak inspiratory pressure (PIP) was maintained at 12 cm H_2O for every breath hold with the use of a flow restrictor in order to avoid the low PIP region where ADC is strongly dependent on lung compliance (39). Animals were sacrificed at the end of the experiment by intravenous injection of Euthanyl Forte (Bimeda-MTC, Cambridge, Canada).

3.2.4 MR Acquisition

A 73.5 mT custom-built resistive MRI system (29) with maximal gradients of 180 mT/m was used to quantify whole lung diffusion coefficients. A custom-built transmit-only/receive-only saddle coil tuned to 0.866 MHz was used for these studies; the receive coil was built using Litz wire (Kerrigan Lewis Wire Products, Chicago, IL) to reduce coil dominated noise at these low frequencies (~1 MHz) (40). Acquisition of the data was performed with an APOLLO MRI console using the accompanying NTNMR software (Tecmag Inc., Houston, TX). The 90° and 180° RF pulse was calibrated with continuously flowing hyperpolarized ^{129}Xe in a syringe placed within an annular cylinder of water to properly load the coil. For the 180° RF pulse calibration, the pulse width of a single square pulse was varied until the minimum free induction decay (FID) signal was observed, and an inversion in phase of the FID was seen. The 90° RF pulse was calibrated in a similar manner.

A trapezoidal gradient PGSE experiment (Fig. 3.1) was performed (41) during 4 second ^{129}Xe breath holds (one per b-value, for each Δ), preceded by three ^{129}Xe wash-out breaths to remove residual air (eg. oxygen) in the lungs (8) thereby maximizing signal. The pulse sequence had the following parameters: gradient ramp up/down times (τ) of 600 μs and flat top times (δ–2τ) of 800 μs, hard 90° and 180° pulses of 65 μs and 130 μs duration, N=16 acquisition points was used to acquire both the FID and echo (N=32 total) with a dwell time of 100 μs. Eight b-values ranging from 0 to 77 s/cm^2 were used for each diffusion time by varying the gradient strength, and each b-value was acquired during separate breath holds The above experiments were repeated for Δ = 6, 50 and 100 ms for all rats. These choices of diffusion times and b-values were based on the simulations as well as hardware limitations. A syringe phantom measurement of the self-diffusion coefficient of hyperpolarized natural abundance xenon gas (25.9% ^{129}Xe) was performed to confirm that the prescribed PGSE sequence was properly calibrated. A 60 ml medical syringe was connected to the xenon bag, the line between the bag and syringe was vacuumed and 10-20 ml of xenon was drawn into the syringe.

3.2.5 Morphological Analysis

Lungs were extracted post-mortem, filled with a 10% formalin solution and then placed in this same solution for 24 hours (42). The lungs were then embedded in paraffin, sectioned into eight slides covering four transverse regions of the lung and stained with hematoxylin and eosin. Five representative images from each slide were acquired at 10x magnification using an Axio Imager.A1 microscope (Carl Zeiss MicroImaging, Thornwood, NY), Retiga EXi 1294 camera (QImaging, Surrey, Canada) and Image-Pro Plus 7.0 software (MediaCybernetics, Bethesda, MD). The mean linear intercepts (L_m) were counted on a 4x3 grid for each of these images (13). Mean linear intercepts for five images at 10x magnification from eight slides for eight rats were calculated with a 4x3 grid; a grand total of 30,950 intercepts were counted manually.

3.2.6 Data Analysis

Normalized echoes were calculated for each b-value, and the following anisotropic diffusion equation was fit to the data using a non-linear least squares Matlab algorithm (lsqcurvefit.m, The Mathworks, Natick, MA) to extract whole-lung longitudinal and transverse diffusion coefficients (D_L and D_T):

$$\frac{S}{S_0} = e^{-bD_T}\left[\frac{\pi}{4b(D_L - D_T)}\right]^{1/2} \Phi\left\{[b(D_L - D_T)]^{1/2}\right\} \qquad [3.3]$$

where S is the normalized echo for each b-values, S_0 is the normalized echo for b = 0 s/cm^2 and Φ is the error function.

Statistical analysis was performed using Prism® (GraphPad Software Inc., La Jolla, CA). An unpaired two-tailed Student's t-test was implemented between the measured anisotropic ADCs in the normal and elastase-instilled rats as well as for L_m from histology between these two cohorts. A Pearson test was used to estimate the strength of correlations between increases in L_m and the measured anisotropic ADCs for sham and elastase-instilled rats.

3.3 Results

3.3.1 Simulations

Figures 3.2 a) and b) show the difference between diseased and healthy airways for simulated D_L and D_T diffusion coefficients for Δ ranging from 1 to 100 ms. The largest difference in D_T between the healthy and disease model occurred at Δ = 5 ms (159% increase), and the largest difference in D_L occurred at Δ = 50 ms (53% increase). As expected, both D_L and D_T converged towards the self-diffusion coefficient of xenon at short diffusion times, and D_L follows the same general trend previously observed for ^{3}He ADC in the cylinder model (Fig. 4 of (34)).

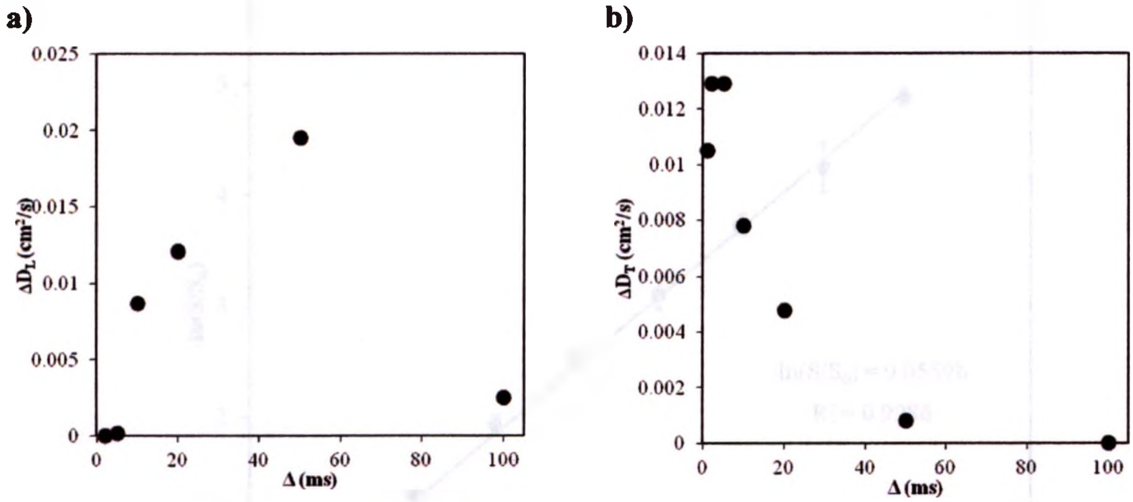

Figure 3.2 Calculated differences in longitudinal (a) and transverse (b) diffusion coefficients between normal and emphysematous terminal airways as a function diffusion times (Δ = 1 to 100 ms). Diffusion coefficients were extracted by fitting the Eqn. [3.3] to data simulated using the Bloch-Torrey equations describing anisotropic ^{129}Xe diffusion in a budded cylinder model of the terminal airways.

3.3.2 Phantom Experiments

Figure 3.3 shows the relationship between $-\ln(S/S_0)$ and b-value for hyperpolarized natural abundance xenon (25.9% ^{129}Xe) in a syringe. The measurement was repeated five times for each b-value, the data points are the mean value for each b-value and the error bars represent one standard deviation of the data set. The self diffusion coefficient of natural abundance ^{129}Xe extracted from the slope of a linear least-squares fit to these data was 0.0559 cm^2/s (R^2=0.9986), which agrees well with expected values (9,43), thereby validating this approach.

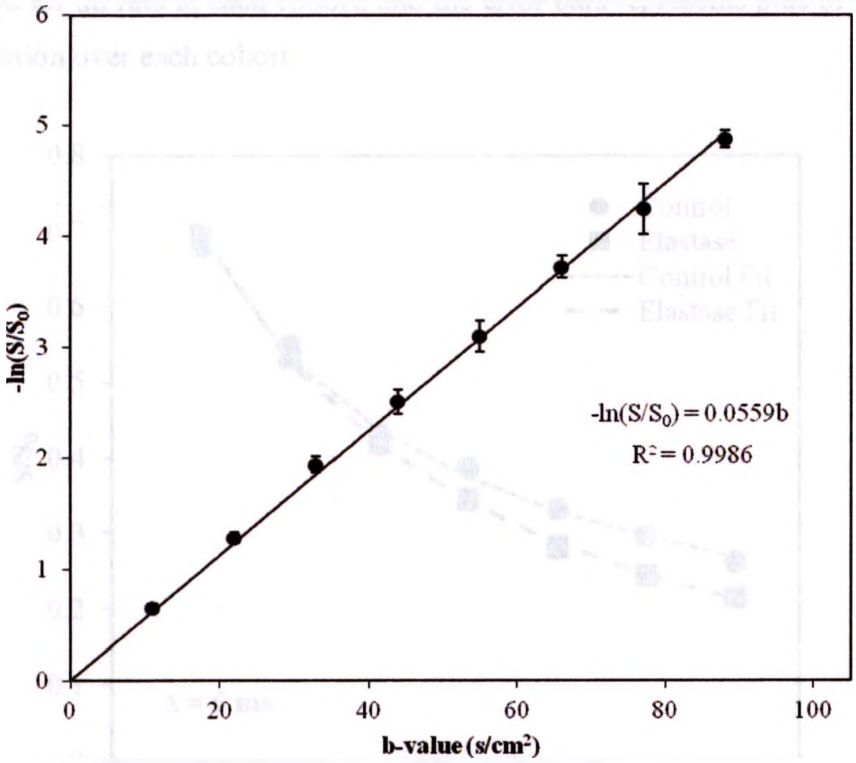

Figure 3.3. Measurement of the self diffusion coefficient of hyperpolarized natural abundance xenon (25.9% ^{129}Xe) at 73.5 mT in a syringe for Δ = 6 ms. The self diffusion coefficient of extracted from the slope of a linear least-squares fit to these data was 0.0559 cm^2/s (R^2=0.9986).

3.3.3 *In vivo* Experiments

Figure 3.4 shows signal as a function of b-value for one representative sham and one representative elastase-instilled rat; the dotted lines represent the best fit based on Eqn. [3.3]. Figure 3.5 shows–ln(S/S_0) as a function of b-value (Δ = 6 ms) for all sham and elastase-instilled rats. The data points represent the average value for all rats of the cohort, and the error bars represents one standard deviation. Figure 3.6 a) and b) show the measured whole lung D_L and D_T for the combined sham and elastase-instilled rat cohorts at the three diffusion times (Δ = 6, 50 and 100 ms). The data points represent the average values for all rats in each cohort, and the error bars represents plus or minus one standard deviation over each cohort.

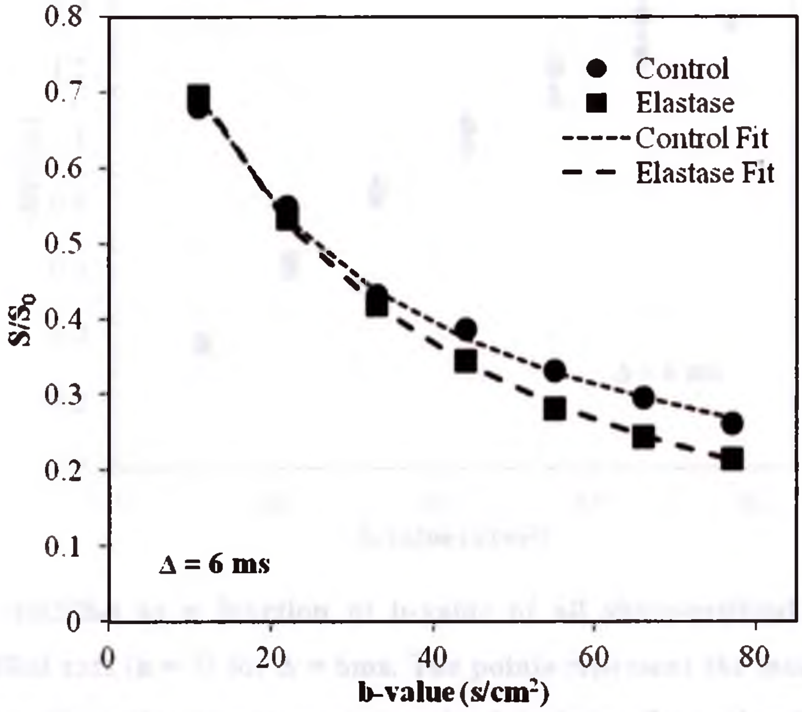

Figure 3.4. S/S_0 as a function of b-value for a representative sham-instilled and elastase-instilled rat for Δ = 6ms. The longitudinal and transverse diffusion coefficients extracted from the sham-instilled rat were 0.1127 and 0.0018 cm^2/s respectively, while for the elastase-instilled rat were 0.0963 and 0.0060 cm^2/s respectively.

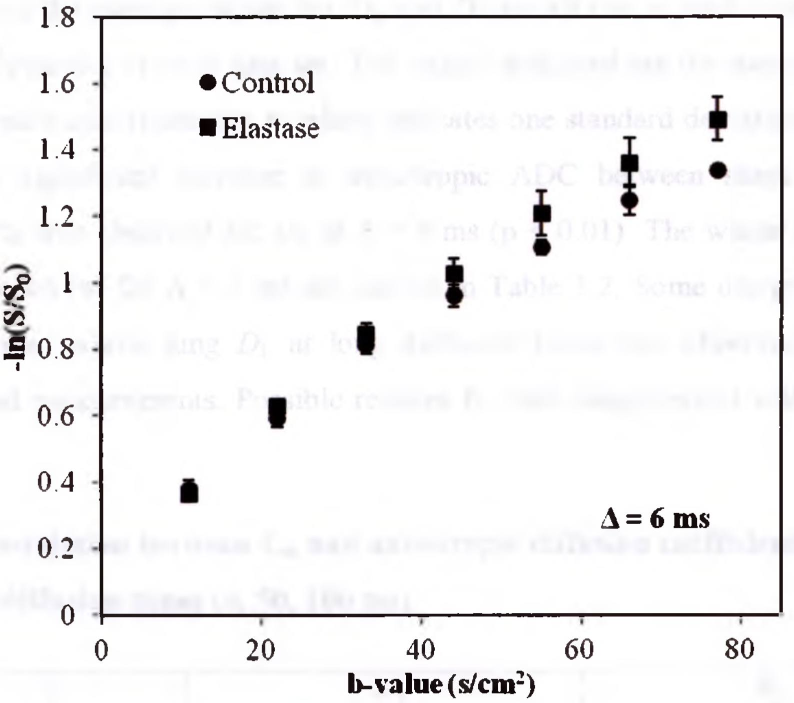

Figure 3.5. –ln(S/S₀) as a function of b-value of all sham-instilled (n = 4) and elastase-instilled rats (n = 5) for Δ = 6ms. The points represent the mean values and the error bars reflect plus or minus one standard deviation for each cohort.

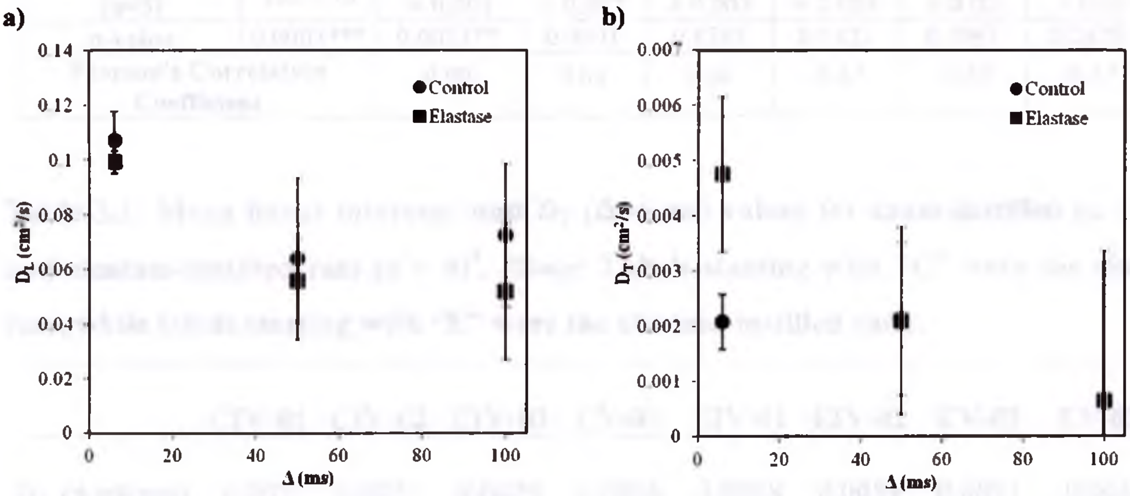

Figure 3.6. Experimental longitudinal (a) and transverse (b) diffusion coefficients for three diffusion times (6, 50 and 100 ms) measured in the whole lung of elastase-instilled (n=5) and sham-instilled rats (n=4). The points represent the mean values and the error bars reflect plus or minus one standard deviation from the two cohorts.

Table 3.1 shows the average values for D_L and D_T for all rats in each cohort as well as one standard deviation of each data set. The values indicated are the mean of the values for all rats of each cohort and the ± values indicates one standard deviation of the mean. A statistically significant increase in anisotropic ADC between sham and elastase instilled cohorts was observed for D_T at $\Delta = 6$ ms ($p < 0.01$). The whole lung D_T value measured for each rat for $\Delta = 6$ ms are shown in Table 3.2. Some disagreement in the behavior of mean whole lung D_L at long diffusion times was observed between the simulations and measurements. Possible reasons for this disagreement will be discussed later.

Table 3.1: Correlation between L_m and anisotropic diffusion coefficients (D_L and D_T) for three diffusion times (6, 50, 100 ms).

	L_m (µm)	D_T (cm²/s)			D_L (cm²/s)		
Diffusion time (Δ)		**6 ms**	**50 ms**	**100 ms**	**6 ms**	**50 ms**	**100 ms**
Sham-instilled (n=4)	73 ± 4	0.0021 ± 0.0005	0.002 ± 0.001	0.001 ± 0.003	0.11 ± 0.01	0.06 ± 0.03	0.07 ± 0.03
Elastase-instilled (n=5)	122 ± 13	0.005 ± 0.001	0.002 ± 0.002	0.001 ± 0.003	0.099 ± 0.004	0.06 ± 0.02	0.05 ± 0.02
p-value	0.0003***	0.0021**	0.9601	0.8585	0.2427	0.5967	0.2429
Pearson's Correlation Coefficient		0.90	0.04	0.08	-0.47	-0.32	-0.47

Table 3.2: Mean linear intercept and D_T (Δ=6 ms) values for sham-instilled (n = 4) and elastase-instilled rats (n = 4)[1]. (Note: Labels starting with "C" were the sham rats, while labels starting with "E" were the elastase-instilled rats).

	CIV-01	**CIV-02**	**CIV-03**	**CV-01**	**EIV-01**	**EIV-02**	**EV-02**	**EV-03**
D_T (Δ =6 ms)	0.002	0.0021	0.0029	0.0016	0.0038	0.0059	0.0033	0.006
L_m (µm)	68±14	73±14	77±16	74±15	117±33	141±72	111±39	120±46

[1] **Histology data from one elastase-instilled rat was unavailable as there were complications in removing the lung.**

3.3.4 Morphology

Table 3.1 shows the p-values for increases in L_m as well as for D_L and D_T between sham and elastase-instilled rats for all Δ values. Histological data from one rat was unavailable as there were complications in removing the lung. Table 3.1 also provides the Pearson Correlation Coefficient (r) between the changes in L_m and anisotropic diffusion coefficients for all Δ values for each rat cohort. The strongest correlation between L_m and the anisotropic ADCs was observed for D_T at $\Delta = 6$ ms, and had a Pearson Correlation Coefficient r of 0.90.

Table 3.2 summarizes the mean linear intercept results for the sham ($n = 4$) and elastase ($n = 4$) as well as the whole-lung D_T values for each rat for $\Delta = 6$ ms. The L_m values represent the mean for each rat and the error bars represent plus or minus one standard deviation based on the sampling of each rat lung. Note that these standard deviations mainly represent the heterogeneity of mean linear intercept measurements throughout the lungs and are not substantially due to errors in the measurement method. Figure 3.7 shows an example H&E stained sham a) and elastase-instilled histological slide b), where the damage due to the elastase is clearly visible as increase in airspace.

a) **b)**

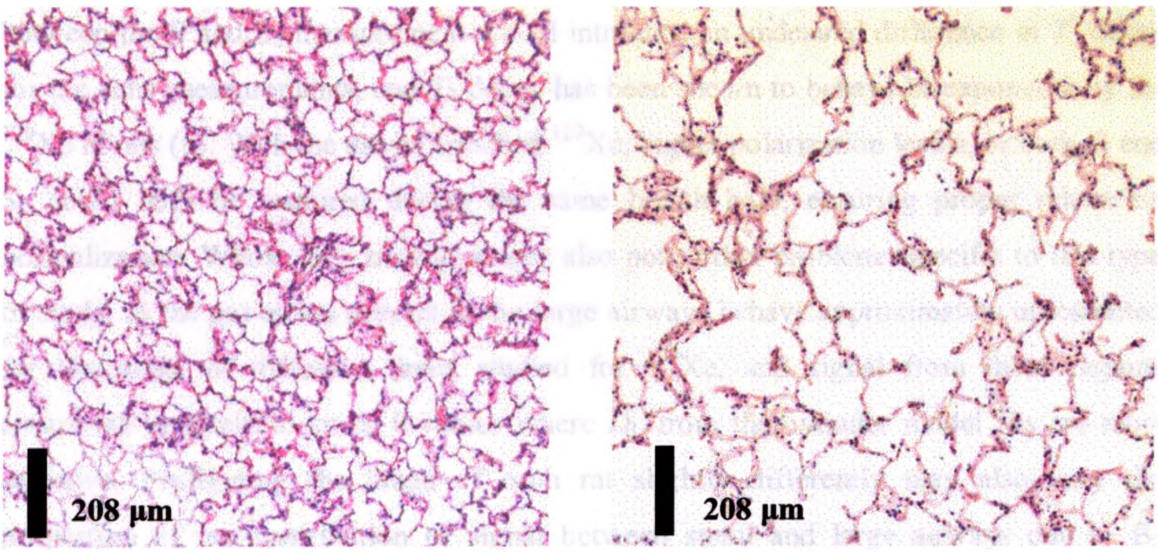

Figure 3.7. H&E stained histological slide images of sham-instilled (a) and elastase-instilled (b) rat lungs. Notice the enlarged airspaces in the elastase-instilled rat lungs.

3.4 Discussion

Results obtained from *in vivo* experiments at 73.5 mT show a significant increase in D_T for Δ = 6 ms ($p < 0.01$) between sham and elastase-instilled cohorts (Table 3.1). As a result, a strong correlation between L_m and D_T for Δ = 6 ms ($r = 0.90$) was also observed, suggesting that D_T measured at Δ = 6 ms may be as effective as the mean linear intercept at quantifying damage due to instilled elastase in rat lungs. Considering that the diffusion coefficients are obtained from whole lung measurements, the observed increase of *in vivo* D_T for Δ = 6 ms (138%) is in relatively good agreement with the numerically predicted value (159%).

No statistically significant differences were observed for D_L at any of the Δ values. This is not consistent with the theoretical model which predicted a significant difference in D_L at Δ~50 ms, according to numerical predictions in Fig. 3.2. The possible sources of error in the D_L at long diffusion times deserve some discussion. Due to the use of natural abundance ^{129}Xe and the achievable polarization levels, the normalized echoes with (S) and without (S_0) applied gradients were measured using separate breath holds. Although three wash-out breaths were applied for each acquisition to minimize residual atmospheric gases in the lung, any differences in the gas composition present in the lungs between the S and S_0 measurement would introduce an undesired difference in T_2 decay for the echo measurements, and T_2 decay has been shown to behave bi-exponentially for ^{129}Xe in rats (8). With the use of enriched ^{129}Xe, higher polarization levels, or both, S and S_0 could both be acquired during the same breath hold, ensuring proper relaxation normalization. Whole lung measurements also pose other problems specific to this type of study, as the gas atoms present in the large airways behave approximately unrestricted for the range of diffusion times studied for ^{129}Xe, and signal from these regions contribute uniquely to small b-values where D_L from the cylinder model fits are most sensitive. Positioning the lungs of each rat slightly differently may also vary the proportion of the contribution of signal between small and large airways due to B_1 sensitivity variations. Both of these problems could potentially be solved by regional ADC mapping using fast imaging techniques. Future studies providing anisotropic ^{129}Xe ADC coefficient maps of the lungs would also be beneficial for investigating regional structural information of the lungs and may be possible with the use of enriched ^{129}Xe and high-performance polarizers (44). Ventilator induced lung injury may have also occurred, as most experiments lasted up to four hours due to the long xenon collection times. Future studies could employ shorter collection times to reduce the duration that the animal is mechanically ventilated, or multiple polarizers could be used simultaneously. One last contribution to discuss is an additional term to the b-value that can manifest when a background gradient from the non-uniformities in the static magnetic field (G_0) couples with the applied diffusion gradient (G_m) (41). Though often neglected, the contribution of this term can be important when ΔG_0 is on the order of δG_m, which may occur at the large Δ used in this study. This effect was confirmed *in vitro* by purposely manipulating G_0 over a range of static background gradients with the low field MRI system used in this study. However, *in vivo,* no significant changes were observed, possibly due to the smaller ADC from restricted diffusion and its effect on the signal vs. b-value slope. Field inhomogeneities due to air-tissue susceptibility differences should not contribute significantly to the coupling term of the b-value at long diffusion times, as this term is proportional to $\mathbf{G_m \cdot G_0}$, and would average close to zero due to the spherical nature of alveoli.

Some D_L values are observed to be greater than the self-diffusion coefficient of ^{129}Xe. Closer investigation indicates that this may be an artefactual behavior of the Yablonskiy model fits to the whole lung data, possibly due to the fact that these measurements contain signal from gas in both restricted (terminal airways) and unrestricted (large airways) environments. Figure 3.5 shows the relationship between $-\ln(S/S_0)$ and b-values (Δ = 6 ms) for sham and elastase-instilled rats. The largest two point b-value ADC is measured between b = 0 and 11 s/cm^2 to be 0.034 cm^2/s for both cohorts, almost half of the self-diffusion coefficient of ^{129}Xe. This indicates that no signal attenuation measured due to diffusion sensitizing gradients were non-physical, and therefore the large D_L values may be a result of fitting the Yablonskiy model to this data set, possibly due to the use of whole lung measurements.

It has been recently reported that the analytical cylinder model of anisotropic ADC may not be an appropriate model as gases exhibit non-Gaussian diffusion in heterogeneous structures (45) when in the localized diffusion regime. Since then, the cylinder model has been updated through numerical simulations in an attempt to correct the model for non-Gaussian effects on D_L and D_T (36). This model was deemed inappropriate for this study as there has not been extensive *in vivo* ^{3}He studies performed with this model to provide a thorough comparison for a ^{129}Xe study. In addition, a recent study (46) suggests that the updated cylinder model may still be incomplete as there are significant deviations between the model and *in vitro* experiments for large gradient strengths. Furthermore, models that only account for the terminal airway microstructure are likely not sufficient to described anisotropic diffusion at longer diffusion times where diffusion lengths are on the order of 0.1 cm and exceed the terminal airway lengths (a few hundred microns). Models which incorporate the branching structure of the lung airway tree (47,48) will likely be more useful for predicting diffusion behaviour at diffusion times in excess of 40-50 ms, and may explain the discrepancy observed between our theory and experiment at the long diffusion times used in this study.

These results can be compared to previous ^{3}He work that investigated D_L or D_T changes due to elastase damage in the rat lung at sub-millisecond diffusion times (15). That study showed for the same animal model used in this paper that D_T strongly correlated with L_m (r = 0.90) for a diffusion time of Δ = 360 μs. Our study using ^{129}Xe showed the same strength of correlation (Table 3.2) occurs for D_T a diffusion time over 15 times larger (Δ = 6 ms) than that reported for ^{3}He, suggesting that whole lung ^{129}Xe studies may be as efficient at quantifying emphysema as ^{3}He. In addition, there is a significant decrease in gradient strength required for ^{129}Xe studies rat due to the longer diffusion times compared to ^{3}He, which may make anisotropic ^{129}Xe ADC studies a more viable choice compared to ^{3}He ADC on clinical MR systems. Previous long range ^{3}He diffusion studies using stimulated echoes (25,26) and magnetization tagging (27) have shown that ^{3}He ADCs measured for diffusion times on the order of a few seconds have good sensitivity for detecting emphysema-like tissue destruction and COPD. Though the current study used diffusion times up to 100 ms and ADC sensitivity was observed at the long Δ, the diffusion length for ^{129}Xe at Δ~100 ms would not considered long range as its diffusion coefficient is approximately 30 times smaller than that of ^{3}He. Therefore it may be of interest to pursue even longer Δ values using ^{129}Xe and this low field approach in future, providing T_2* is sufficiently long ($\Delta \sim T_2$*).

One interesting observation can be seen in Fig. 3.5, where significant signal change between sham and elastase-instilled rats only occurs at b-values greater than 60 s/cm^2 for Δ = 6 ms. For the PGSE pulse sequence and 6 ms diffusion times, this requires applying gradient strengths greater than 10 G/cm. As clinical MR systems typically only have gradient strengths up to 5 G/cm, high performance insert gradients (49) may be required to achieve optimal sensitivity in studying diffusion with rodent disease models using ^{129}Xe on clinical systems. As humans have larger alveoli, T_2^* decay of a pure ^{129}Xe gas mixture is expected to be larger than for rodents, and the large b-values required for increased sensitivity of two b-value ADC measurement may be accessible with clinical gradient strength by using slightly larger diffusion times and slew rates available on high quality clinical scanners.

The correlation between D_T and L_m may prove to be an efficient tool in the future for quantifying emphysema regionally *in vivo* using hyperpolarized ^{129}Xe MRI. The diffusion times where anisotropic ADC was observed in this study are in the range that has typically been used for clinical ^3He studies, suggesting that clinical studies transitioning into hyperpolarized ^{129}Xe must take care when interpreting non-linear ADC measurements in the lung, particularly when only two b-values are used.

3.5 Conclusion

The results of this study demonstrate that whole-lung measurements of ^{129}Xe transverse diffusion coefficients (D_T) for Δ = 6 ms correlate well with L_m in an elastase-instilled rat model of emphysema. These results are similar to previous ^3He D_T measurements obtained at sub-millisecond Δ values, consistent with the expected differences in self-diffusion coefficient between the two gases. This study confirms that ^{129}Xe anisotropic ADC measurements are as sensitive as ^3He for quantifying elastase-instilled alveolar destruction in rats and could be a valuable tool for measuring regional microstructural changes associated with emphysema and COPD.

3.6 References

1. Möller HE, Chen XJ, Saam B, Hagspiel KD, Johnson GA, Altes TA, de Lange EE, Kauczor H-U. MRI of the lungs using hyperpolarized noble gases. Magnetic Resonance in Medicine 2002;47(6):1029-1051.

2. de Lange EE, Altes TA, Patrie JT, Battiston JJ, Juersivich AP, Mugler JP, 3rd, Platts-Mills TA. Changes in regional airflow obstruction over time in the lungs of patients with asthma: evaluation with 3He MR imaging. Radiology 2009;250(2):567-575.

3. Tzeng YS, Lutchen K, Albert M. The difference in ventilation heterogeneity between asthmatic and healthy subjects quantified using hyperpolarized He-3 MRI. Journal of Applied Physiology 2009;106(3):813-822.

4. Mathew L, Evans A, Ouriadov A, Etemad-Rezai R, Fogel R, Santyr G, McCormack DG, Parraga G. Hyperpolarized 3He magnetic resonance imaging of chronic obstructive pulmonary disease: reproducibility at 3.0 tesla. Acad Radiol 2008;15(10):1298-1311.

5. Kirby M, Mathew L, Wheatley A, Santyr GE, McCormack DG, Parraga G. Chronic obstructive pulmonary disease: longitudinal hyperpolarized (3)He MR imaging. Radiology 2010;256(1):280-289.

6. Ouriadov AV, Lam WW, Santyr GE. Rapid 3-D mapping of hyperpolarized He-3 spin-lattice relaxation times using variable flip angle gradient echo imaging with application to alveolar oxygen partial pressure measurement in rat lungs. Magn Reson Mater Phy 2009;22(5):309-318.

7. Fischer MC, Kadlecek S, Yu JS, Ishii M, Emami K, Vahdat V, Lipson DA, Rizi RR. Measurements of regional alveolar oxygen pressure using hyperpolarized He-3 MRI. Academic Radiology 2005;12(11):1430-1439.

8. Kraayvanger RJ, Bidinosti CP, Dominguez-Viqueira W, Parra-Robles J, Fox M, Lam WW, Santyr GE. Measurement of alveolar oxygen partial pressure in the rat lung using Carr-Purcell-Meiboom-Gill spin-spin relaxation times of hyperpolarized 3He and 129Xe at 74 mT. Magnetic Resonance in Medicine 2010;64(5):1484-1490.

9. Chen XJ, Moller HE, Chawla MS, Cofer GP, Driehuys B, Hedlund LW, Johnson GA. Spatially resolved measurements of hyperpolarized gas properties in the lung in vivo. Part I: diffusion coefficient. Magn Reson Med 1999;42(4):721-728.

10. Diaz S, Casselbrant I, Piitulainen E, Pettersson G, Magnusson P, Peterson B, Wollmer P, Leander P, Ekberg O, Akeson P. Hyperpolarized He-3 apparent diffusion coefficient MRI of the lung: Reproducibility and volume dependency in

healthy volunteers and patients with emphysema. Journal of Magnetic Resonance Imaging 2008;27(4):763-770.

11. Peces-Barba G, Ruiz-Cabello J, Cremillieux Y, Rodriguez I, Dupuich D, Callot V, Ortega M, Rubio Arbo ML, Cortijo M, Gonzalez-Mangado N. Helium-3 MRI diffusion coefficient: correlation to morphometry in a model of mild emphysema. European Respiratory Journal 2003;22(1):14-19.

12. Gierada DS, Woods JC, Bierhals AJ, Bartel ST, Ritter JH, Choong CK, Das NA, Hong C, Pilgram TK, Chang YV, Jacob RE, Hogg JC, Battafarano RJ, Cooper JD, Meyers BF, Patterson GA, Yablonskiy DA, Conradi MS. Effects of diffusion time on short-range hyperpolarized3He diffusivity measurements in emphysema. Journal of Magnetic Resonance Imaging 2009;30(4):801-808.

13. Woods JC, Choong CK, Yablonskiy DA, Bentley J, Wong J, Pierce JA, Cooper JD, Macklem PT, Conradi MS, Hogg JC. Hyperpolarized 3He diffusion MRI and histology in pulmonary emphysema. Magn Reson Med 2006;56(6):1293-1300.

14. Yablonskiy DA. Quantitative in vivo assessment of lung microstructure at the alveolar level with hyperpolarized 3He diffusion MRI. Proceedings of the National Academy of Sciences 2002;99(5):3111-3116.

15. Xu X, Boudreau M, Ouriadov A, Santyr GE. Mapping of 3He Apparent Diffusion Coefficient Anisotropy at Sub-millisecond Diffusion Times in an Elastase-Instilled Rat Model of Emphysema. Magnetic Resonance in Medicine 2011;*In Press*.

16. Patz S, Hersman FW, Muradian I, Hrovat MI, Ruset IC, Ketel S, Jacobson F, Topulos GP, Hatabu H, Butler JP. Hyperpolarized (129)Xe MRI: a viable functional lung imaging modality? Eur J Radiol 2007;64(3):335-344.

17. Ruset IC, Ketel S, Hersman FW. Optical pumping system design for large production of hyperpolarized. Phys Rev Lett 2006;96(5):053002.

18. Hersman FW, Ruset IC, Ketel S, Muradian I, Covrig SD, Distelbrink J, Porter W, Watt D, Ketel J, Brackett J, Hope A, Patz S. Large production system for hyperpolarized 129Xe for human lung imaging studies. Acad Radiol 2008;15(6):683-692.

19. Patz S, Muradian I, Hrovat MI, Ruset IC, Topulos G, Covrig SD, Frederick E, Hatabu H, Hersman FW, Butler JP. Human pulmonary imaging and spectroscopy with hyperpolarized 129Xe at 0.2T. Acad Radiol 2008;15(6):713-727.

20. Kaushik SS, Cleveland ZI, Cofer GP, Metz G, Beaver D, Nouls J, Kraft M, Auffermann W, Wolber J, McAdams HP, Driehuys B. Diffusion-weighted hyperpolarized (129) Xe MRI in healthy volunteers and subjects with chronic obstructive pulmonary disease. Magn Reson Med 2011;65(4):1154-1165.

21. Weathersby PK, Homer LD. Solubility of Inert-Gases in Biological-Fluids and Tissues - a Review. Undersea Biomed Res 1980;7(4):277-296.

22. Mansson S, Johansson E, Svensson J, Olsson LE, Stahlberg F, Petersson JS, Golman K. Echo-planar MR imaging of dissolved hyperpolarized 129Xe. Acta Radiol 2002;43(5):455-460.

23. Cleveland ZI, Cofer GP, Metz G, Beaver D, Nouls J, Kaushik SS, Kraft M, Wolber J, Kelly KT, McAdams HP, Driehuys B. Hyperpolarized Xe MR imaging of alveolar gas uptake in humans. PLoS One 2010;5(8):e12192.

24. Abdeen N, Cross A, Cron G, White S, Rand T, Miller D, Santyr G. Measurement of xenon diffusing capacity in the rat lung by hyperpolarized 129Xe MRI and dynamic spectroscopy in a single breath-hold. Magn Reson Med 2006;56(2):255-264.

25. Wang C, Miller GW, Altes TA, de Lange EE, Cates Jr GD, Mugler JP. Time dependence of3He diffusion in the human lung: Measurement in the long-time regime using stimulated echoes. Magnetic Resonance in Medicine 2006;56(2):296-309.

26. Rodríguez I, Pérez-Sánchez JM, Peces-Barba G, Kaulisch T, Stiller D, Ruiz-Cabello J. Long-range diffusion of hyperpolarized3He in rats. Magnetic Resonance in Medicine 2009;61(1):54-58.

27. Woods JC, Yablonskiy DA, Chino K, Tanoli TSK, Cooper JD, Conradi MS. Magnetization tagging decay to measure long-range3He diffusion in healthy and emphysematous canine lungs. Magnetic Resonance in Medicine 2004;51(5):1002-1008.

28. Tsai LL, Mair RW, Rosen MS, Patz S, Walsworth RL. An open-access, very-low-field MRI system for posture-dependent 3He human lung imaging. J Magn Reson 2008;193(2):274-285.

29. Dominguez-Viqueira W, Parra-Robles J, Fox M, Handler WB, Chronik BA, Santyr GE. A variable field strength system for hyperpolarized noble gas MR imaging of rodent lungs. Concepts in Magnetic Resonance Part B: Magnetic Resonance Engineering 2008;33B(2):124-137.

30. Parra-Robles J, Cross AR, Santyr GE. Theoretical signal-to-noise ratio and spatial resolution dependence on the magnetic field strength for hyperpolarized noble gas magnetic resonance imaging of human lungs. Medical Physics 2005;32(1):221.

31. Parra-Robles J, Dominguez Viqueira W, Xu X, Ouriadov A, Santyr GE. Theoretical prediction and experimental measurement of the field dependence of the apparent transverse relaxation of hyperpolarized noble gases in lungs. Journal of Magnetic Resonance 2008;192(1):85-91.

32. Durand E, Guillot G, Darrasse L, Tastevin G, Nacher PJ, Vignaud A, Vattolo D, Bittoun J. CPMG measurements and ultrafast imaging in human lungs with hyperpolarized helium-3 at low field (0.1 T). Magnetic Resonance in Medicine 2002;47(1):75-81.

33. Fichele S, Paley MNJ, Woodhouse N, Griffiths PD, van Beek EJR, Wild JM. Finite-difference simulations of 3He diffusion in 3D alveolar ducts: Comparison with the cylinder model. Magnetic Resonance in Medicine 2004;52(4):917-920.

34. Fichele S. Investigating 3He diffusion NMR in the lungs using finite difference simulations and in vivo PGSE experiments. Journal of Magnetic Resonance 2004;167(1):1-11.

35. Callaghan PT, Jolley KW, Lelievre J. Diffusion of water in the endosperm tissue of wheat grains as studied by pulsed field gradient nuclear magnetic resonance. Biophysical Journal 1979;28(1):133-141.

36. Sukstanskii A, Yablonskiy D. In vivo lung morphometry with hyperpolarized 3He diffusion MRI: Theoretical background. Journal of Magnetic Resonance 2008;190(2):200-210.

37. Yablonskiy DA, Sukstanskii AL, Woods JC, Gierada DS, Quirk JD, Hogg JC, Cooper JD, Conradi MS. Quantification of lung microstructure with hyperpolarized 3He diffusion MRI. J Appl Physiol 2009;107(4):1258-1265.

38. Santyr GE, Lam WW, Ouriadov A. Rapid and efficient mapping of regional ventilation in the rat lung using hyperpolarized3He with Flip angle variation for offset of RF and relaxation (FAVOR). Magnetic Resonance in Medicine 2008;59(6):1304-1310.

39. Xin Y, Enami K, Kadlecek SJ, Mongkolwisetwara P, Kuzma NN, Profka H, Xu Y, Hamedani H, Pullinger BM, Ghosh RK, Rajaei S, Pickup S, Ishii M, Rizi RR. Imaging of Lung Micromechanics with Hyperpolarized Gas Diffusion MRI: Regional Compliace. Proc Intl Soc Mag Reson Med 2011;19.

40. Dominguez-Viqueira W, Berger W, Parra-Robles J, Santyr GE. Litz Wire Radiofrequency Receive Coils for Hyperpolarized Noble Gas MR Imaging of Rodent Lungs at 73.5 mT. Concept Magn Reson B 2010;37B(2):75-85.

41. Stejskal EO, Tanner JE. Spin Diffusion Measurements: Spin Echoes in the Presence of a Time-Dependent Field Gradient. Journal of Chemical Physics 1965;42(1):288-+.

42. Blümler P, Acosta RH, Thomas-Semm A, Reuss S. Lung Fixation for the Preservation of Air Spaces. Experimental Lung Research 2004;30(1):73-82.

43. Hirschfelder JO, Curtiss CF, Bird RB. Molecular theory of gases and liquids. New York,: Wiley; 1954. 1219 p. p.

44. Hersman FW, Ruset IC, Ketel S, Muradian I, Covrig SD, Distelbrink J, Porter W, Watt D, Ketel J, Brackett J, Hope A, Patz S. Large Production System for Hyperpolarized 129Xe for Human Lung Imaging Studies. Academic Radiology 2008;15(6):683-692.

45. Liu C, Bammer R, Moseley ME. Limitations of apparent diffusion coefficient-based models in characterizing non-gaussian diffusion. Magnetic Resonance in Medicine 2005;54(2):419-428.

46. Parra-Robles J, Ajraoui S, Deppe MH, Parnell SR, Wild JM. Experimental investigation and numerical simulation of 3He gas diffusion in simple geometries: Implications for analytical models of 3He MR lung morphometry. Journal of Magnetic Resonance 2010;204(2):228-238.

47. Verbanck S, Paiva M. Simulation of the apparent diffusion of helium-3 in the human acinus. J Appl Physiol 2007;103(1):249-254.

48. Bartel SE, Haywood SE, Woods JC, Chang YV, Menard C, Yablonskiy DA, Gierada DS, Conradi MS. Role of collateral paths in long-range diffusion in lungs. J Appl Physiol 2008;104(5):1495-1503.

49. Chronik B, Alejski A, Rutt BK. Design and fabrication of a three-axis multilayer gradient coil for magnetic resonance microscopy of mice. Magnetic Resonance Materials in Biology, Physics, and Medicine 2000;10(2):131-146.

Chapter 4

4 Discussion and Future Work

4.1 Discussion

The goal for this work was to measure and optimize sensitivity of ^{129}Xe anisotropic ADCs (D_L, D_T) through the investigation of the MR diffusion sensitizing parameters for the purpose of detecting alveolar expansion and destruction. We numerically investigated the behavior of anisotropic diffusion coefficients in a budded cylinder model, and subsequently hypothesized that the transverse anisotropic diffusion coefficient D_T may provide greater sensitivity than D_L for quantifying alveolar enlargement and that this would be measured near a 5 ms diffusion time (Δ). Confirmation of our hypothesis was provided by *in vivo* measurements at 73.5 mT in a rodent model of emphysema based on elastase-instillation, where the only significant increase of anisotropic ADC was observed for D_T at Δ = 6 ms, and a significant correlation between D_T at Δ = 6 ms with histology was reported.

4.1.1 Numerical Simulations

Chapter 2 described finite difference numerical simulations (1) of ^{129}Xe diffusion in a budded cylinder model (2) of the terminal airways to investigate the dependence of Yablonskiy anisotropic diffusion coefficients (3) on diffusion time. In agreement with previously reported results for ^{3}He (4), the transverse diffusion coefficient D_T provided optimal sensitivity to alveolar destruction caused by the elastase. The largest percentage increase in D_T (159%) for the disease model occurred at Δ = 5 ms, while for D_L the largest increase was only about one third the increase observed in D_T (53% for D_L).

4.1.2 *In vivo* ^{129}Xe ADC in an Elastase Rat Model at 73.5 mT

This work hypothesized that ^{129}Xe anisotropic diffusion coefficients can be sensitive to changes in alveolar airspace induced in an elastase-instilled rat model of emphysema by investigating the optimal diffusion time (Δ) and anisotropic ADCs (D_L or D_T) for quantifying disease using a 73.5 mT MRI system. The results in Chapter 3 supported this hypothesis, with a significant increase in anisotropic ADC following elastase-instillation measured for the transverse diffusion coefficient (D_T) at $\Delta = 6$ ms. D_T was measured for $\Delta = 6$ ms in a sham-instilled cohort to be 0.0021 ± 0.0005 cm^2/s, and for the elastase-instilled cohort D_T increased by 138% to 0.005 ± 0.001 cm^2/s, and the increase was determined to be statistically significant using an unpaired Student's t-test ($p = 0.0021$). These results were compared with histological evidence of an increase of airspace in the elastase-instilled rats by measuring the mean linear intercepts (L_m), and a significant increase in L_m was observed ($p = 0.0003$). A comparison between D_T for $\Delta = 6$ ms with L_m yielded a strong correlation by measuring the Pearson's Correlation Coefficient r ($r = 0.90$). A previously published study of ^3He anisotropic ADC measurements in this disease model (4) showed an equally strong correlation between D_T and L_m for $\Delta = 360$ μs, suggesting that whole lung ^{129}Xe studies may be as efficient at quantifying emphysema as ^3He.

4.1.3 Current Limitations

The numerical simulations used in this study are limited to short diffusion lengths/times due to the model used. Assuming that the model breaks down after unrestricted xenon would diffuse a mean path of two cylinder lengths (1.28 mm), this would imply that the model may only be a good approximation for diffusion times below 40 ms (Eqn. [1.50], Chapter 1). The budded cylinder has a role for short diffusion times where the gas diffuses through a few alveoli, but at long diffusion times the model lacks a branching structure to properly model airways. In addition, the disease model presented in this work is a simple approximation of the behavior of emphysema-like alveolar enlargement observed in COPD. In reality, the airways not only expand as a consequence of the elastase damage but severe tissue damage may larger create holes in tissue which were not accounted for in this model. Accounting for gas exchange between neighbouring acini may provide a better approximation of the signal dynamics observed *in vivo*.

The experimental portion of this study consisted of well controlled ventilation and breath-hold measurements in anaesthetized animals. For safety reasons, humans are typically not anaesthetized and mechanically ventilated for MRI studies, thus patient motion may limit the resolution of ADC maps. Also, due to the anaesthetic properties of xenon at high concentrations, buffer gases (N_2, medical air) are generally mixed with xenon for safety reasons, which reduces the available signal per voxel. Thus, high b-value measurements as described in this work may require the use of enriched ^{129}Xe concentrations instead of natural abundance xenon (25.9% ^{129}Xe), and will increase the overall cost of measurements.

This work was limited to whole lung measurements as the polarization process of the home-built xenon polarizer was not refined enough to achieve polarizations needed for ADC mapping in rats for the strong b-values used. The signal-to-noise ratio is also limited by the hardware (eg. receive coil sensitivity, noise filters), even though considerable efforts were made to have the receive coils be in the sample noise dominated regime with the use of Litz wire (5). Due to the maturation period of the disease (six to eight weeks), the weight gain of the rats made them too large to use our most sensitive small xenon coils. In addition to using enriched ^{129}Xe, high efficiency xenon polarizers have recently been developed (6) achieving polarizations of up to 64 %, thus hyperpolarized ^{129}Xe anisotropic ADC mapping in humans or even rodents may be achievable with decent resolution.

4.2 Future Work

4.2.1 ADC Mapping

An important next step of this work will be to perform ^{129}Xe ADC mapping in disease models. Emphysema is a heterogeneous disease which manifests in different regions of the lungs depending on the nature of the disease. Centriacinar emphysema is mostly present in smokers and occurs most commonly in the upper regions of the lung; panacinar emphysema is typically present in patients with α1-antitrypsin deficiency and typically occurs in the lower regions of the lung. In addition to providing valuable regional information on disease, ADC mapping would likely provide a better a better measure of the Yablonskiy anisotropic ADCs (D_L and D_T) as signal mixing between large airways and the terminal airways would be minimized compared to whole lung measurements.

Due to the non-renewable nature of hyperpolarized gases and the presence of severe signal attenuation contributors in the lung (O_2, air-tissue susceptibility differences), rapid k-space acquisition imaging pulse sequences should be used for ADC mapping. Two common fast imaging techniques that may be worth investigating for ADC mapping are Echo Planar imaging (EPI) and Rapid Acquisition with Relaxation Enhancement (RARE).

4.2.2 Echo Planar Imaging (EPI)

Echo planar imaging (7,8) is a gradient echo approach which acquires k-space extremely quickly, typically using a single 90° RF pulse followed by a train of gradient echoes which is called a "single-shot" sequence. Figure 4.1 shows an example of a single shot Cartesian spin echo EPI pulse sequence.

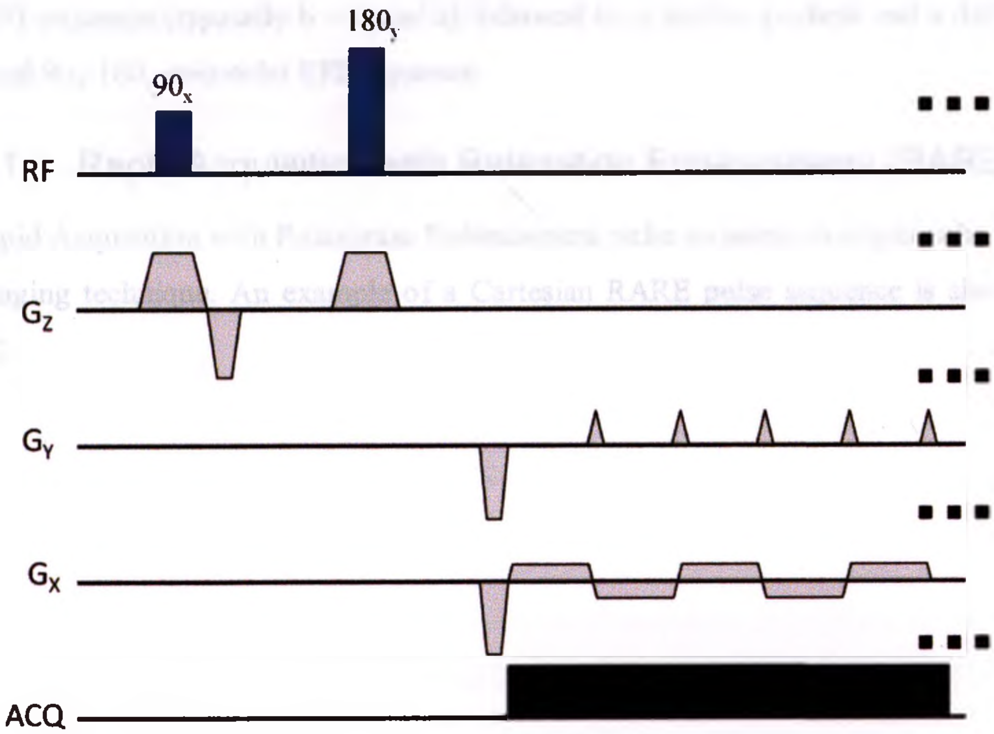

Figure 4.1. An example of a Cartesian spin-echo EPI pulse sequence.

Following the applications of RF pulses along with compensating phase-encode and frequency-encode gradients, bipolar frequency-encode gradients are continuously applied in between small positive phase-encode gradients to continuously acquire k-space in a zig-zag pattern. EPI sequences acquire k-space faster than most other imaging pulse sequences (i.e. RARE), but they impose a considerable burden on the imaging gradients due to rapidly applying gradients with large slew rates. As the data is acquired through gradient echoes, k-space is weighted by T_2^* decay which can limit diffusion times achievable in diffusion imaging.

Diffusion coefficient mapping can be integrated with spin-echo EPI pulse sequence by applying balanced diffusion sensitizing gradients before and after the 180° pulse (7). Typically the center of k-space will be acquired first and the parameters are adjusted such that the diffusion time corresponds to half echo time of the 90_x-180_y pulse, and the spin echo from these pulses provides the best signal for the first few lines of k-space which regulates the SNR of the image. Practically, if the polarization levels permit, two b-value weighted images can be acquired in a single breath hold by first applying a 45°-180° spin-echo EPI sequence (typically b = 0 cm^2/s) followed by a spoiler gradient and a diffusion sensitized 90_x-180_y spin-echo EPI sequence.

4.2.2.1 Rapid Acquisition with Relaxation Enhancement (RARE)

The Rapid Acquisition with Relaxation Enhancement pulse sequence is a spin-echo based fast imaging technique. An example of a Cartesian RARE pulse sequence is shown in Fig. 4.2.

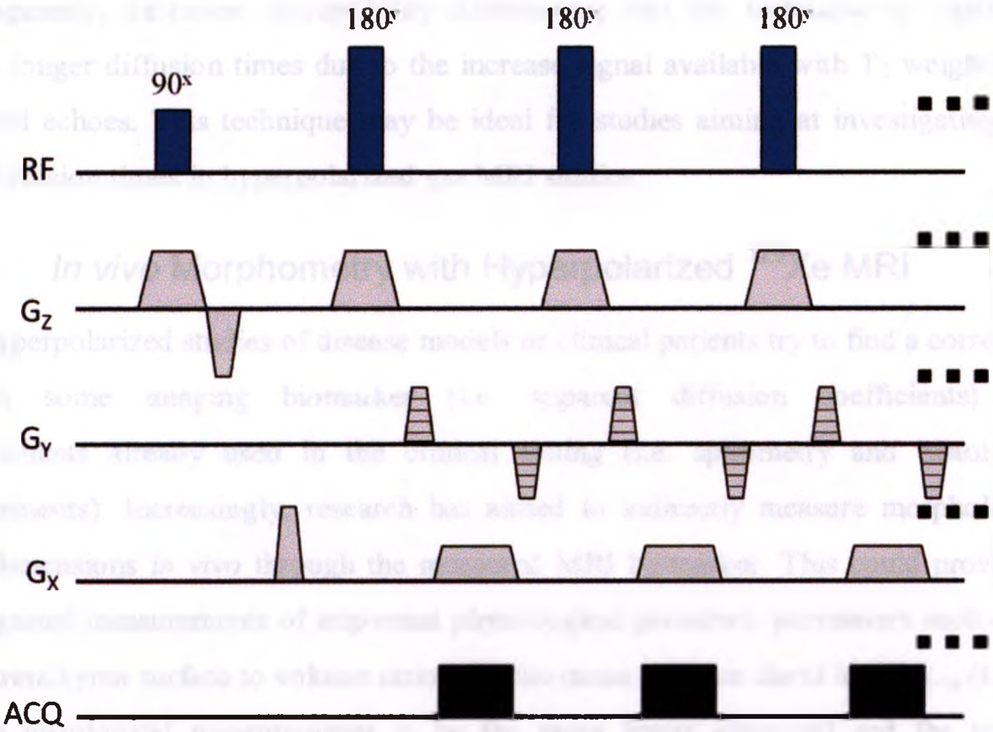

Figure 4.2. An example of a Cartesian RARE pulse sequence.

Following a 90° pulse, a train of spatially selective 180° RF pulses continually refocus the transverse magnetization, providing a T_2 weighting to the acquired data. K-space is traversed by applying a phase-encoding gradient after each 180° pulse, and a line of k-space is acquired while a frequency encoding gradient is applied. A rewinding phase-encoding gradient is applied prior to the following 180° refocusing pulse to ensure proper phase coherence throughout the echo train. Diffusion coefficient maps can be acquired in a similar method as was described in Section 4.2.1.1 for EPI pulse sequences.

Due to the use of an RF echo train and the many pulse sequence considerations necessary to ensure proper echo formation such as bipolar phase encoding/rewinding gradients and crusher gradient (not shown in Fig. 4.2), RARE generally a acquires k-space slower than EPI. RARE pulse sequences also have an increased specific absorption rate (SAR) than gradient echo imaging techniques due to the long train of RF pulses, and low field MRIs may provide an advantage at using RARE due to a reduction in energy deposition per pulses as the RF frequencies are much smaller than used than at high fields. Despite these disadvantages, RARE images are less sensitive to field inhomogeneities (i.e. B_0

inhomogeneity, air-tissue susceptibility differences) and the technique is capable to acquire longer diffusion times due to the increase signal available with T_2 weighting of refocused echoes. This technique may be ideal for studies aiming at investigating long range diffusion times in hyperpolarized gas MRI studies.

4.2.3 *In vivo* Morphometry with Hyperpolarized ^{129}Xe MRI

Most hyperpolarized studies of disease models or clinical patients try to find a correlation between some imaging biomarker (i.e. apparent diffusion coefficients) with measurements already used in the clinical setting (i.e. spirometry and histological measurements). Increasingly, research has aimed to indirectly measure morphological tissue dimensions *in vivo* through the measured MRI biomarker. This could provide *in vivo* regional measurements of important physiological geometric parameters such as the lung parenchyma surface to volume ratio S/V, the mean airspace chord length L_m (known through histological measurements to be the mean linear intercept) and the volume density of alveoli N_A.

Recent numerical studies have shown a relationship between the anisotropic diffusion coefficient and b-values (a result of non-Gaussian diffusion at large b-values in heterogeneous structures), and their relationship with geometric parameters of the terminal airways such as external and internal airway radii, R and r, and the alveolar size, L. Using these geometrical dimensions, physiological parameters S/V, L_m and N_A can be estimated. A recent ^{3}He anisotropic ADC study (9) has verified this model in *ex vivo* human lungs, and good agreement of the modeled parameters S/V, L_m and N_A with histological measurements of the same geometric parameters was observed. If ^{129}Xe can be polarized to high enough signal levels, this model could be investigated with ^{129}Xe using the ADC mapping by applying a diffusion sensitized EPI or RARE sequence. As the ^{3}He study used diffusion times of approximately 2 ms, diffusion times on the order of 50-100 ms may be required due to the smaller diffusion coefficient of ^{129}Xe, thus RARE may be the better choice of pulse sequences. Low field MRIs may prove to be a useful tool for this investigation due to the low air-tissue susceptibility differences at low field strengths.

4.3 Conclusion

This thesis proposed a way of measuring pulmonary airway enlargement and destruction with the use of ^{129}Xe diffusion MRI, and was successful at identifying key factors that characterize these measurements (diffusion anisotropy, optimal diffusion times). Although signal levels were not large enough to enable regional diffusion coefficient maps, recent advances in ^{129}Xe hyperpolarizers may provide the high signal levels needed in the near future, and results from this study can provide important information on diffusion sensitivity behaviour for this transition. Overall, hyperpolarized ^{129}Xe anisotropic ADC measurements could be a useful tool at regionally quantifying emphysema during the early stages of COPD.

4.4 References

1. Fichele S. Investigating 3He diffusion NMR in the lungs using finite difference simulations and in vivo PGSE experiments. Journal of Magnetic Resonance 2004;167(1):1-11.

2. Fichele S, Paley MNJ, Woodhouse N, Griffiths PD, van Beek EJR, Wild JM. Finite-difference simulations of 3He diffusion in 3D alveolar ducts: Comparison with the cylinder model. Magnetic Resonance in Medicine 2004;52(4):917-920.

3. Yablonskiy DA. Quantitative in vivo assessment of lung microstructure at the alveolar level with hyperpolarized 3He diffusion MRI. Proceedings of the National Academy of Sciences 2002;99(5):3111-3116.

4. Xu X, Boudreau M, Ouriadov A, Santyr GE. Mapping of 3He Apparent Diffusion Coefficient Anisotropy at Sub-millisecond Diffusion Times in an Elastase-Instilled Rat Model of Emphysema. Magnetic Resonance in Medicine 2011;*In Press*.

5. Dominguez-Viqueira W, Berger W, Parra-Robles J, Santyr GE. Litz Wire Radiofrequency Receive Coils for Hyperpolarized Noble Gas MR Imaging of Rodent Lungs at 73.5 mT. Concept Magn Reson B 2010;37B(2):75-85.

6. Hersman FW, Ruset IC, Ketel S, Muradian I, Covrig SD, Distelbrink J, Porter W, Watt D, Ketel J, Brackett J, Hope A, Patz S. Large Production System for Hyperpolarized 129Xe for Human Lung Imaging Studies. Academic Radiology 2008;15(6):683-692.

7. Edelman RR, Wielopolski P, Schmitt F. Echo-planar MR imaging. Radiology 1994;192(3):600-612.

8. Saam B, Yablonskiy DA, Gierada DS, Conradi MS. Rapid imaging of hyperpolarized gas using EPI. Magnetic Resonance in Medicine 1999;42(3):507-514.

9. Yablonskiy DA, Sukstanskii AL, Woods JC, Gierada DS, Quirk JD, Hogg JC, Cooper JD, Conradi MS. Quantification of lung microstructure with hyperpolarized 3He diffusion MRI. J Appl Physiol 2009;107(4):1258-1265.

Appendix A: Animal Protocol

Western

January 12, 2009

This is the Original Approval for this protocol
A Full Protocol submission will be required in 2013

Dear Dr. Santyr:

Your Animal Use Protocol form entitled:
Micro-Imaging Approaches for Murine Models of Obstructive Pulmonary Disease
Funding Agency CIHR - Grant #MOP-81357

has been approved by the University Council on Animal Care. This approval is valid from **January 12, 2009** to **January 31, 2009**. The protocol number for this project is **#2008-126**.

1. This number must be indicated when ordering animals for this project.
2. Animals for other projects may not be ordered under this number.
3. If no number appears please contact this office when grant approval is received.
   If the application for funding is not successful and you wish to proceed with the project, request that an internal scientific peer review be performed by the Animal Use Subcommittee office.
4. Purchases of animals other than through this system must be cleared through the ACVS office. Health certificates will be required.

ANIMALS APPROVED FOR 4 Years

Species	Strain	Other Detail	Pain Level	Animal # Total for 4 Years
Rat	Wistar	Males	D	58

REQUIREMENTS/COMMENTS
Please ensure that individual(s) performing procedures on live animals, as described in this protocol, are familiar with the contents of this document.

c.c. Approved Protocol - G. Santyr, M. Pickering
Approval Letter - G. Santyr, M. Pickering

The University of Western Ontario
Animal Use Subcommittee / University Council on Animal Care
Health Sciences Centre, • London, Ontario • CANADA - N6A 5C1
PH: 519-661-2111 ext. 86770 • FL 519-661-2028 • www.uwo.ca / animal

Western

February 1, 2010
*This is the 2nd Renewal of this protocol
*A Full Protocol submission will be required in 2012

Dear Dr. Sanyr

Your Animal Use Protocol form entitled:

Micro-Imaging Approaches for Murine Models of Obstructive Pulmonary Disease

has had its yearly renewal approved by the Animal Use Subcommittee.

This approval is valid from **February 1, 2010** to **January 31, 2011**

The protocol number for this project remains as **#2008-128**

1. This number must be indicated when ordering animals for this project.
2. Animals for other projects may not be ordered under this number.
3. If no number appears please contact this office when grant approval is received. If the application for funding is not successful and you wish to proceed with the project, request that an internal scientific peer review be performed by the Animal Use Subcommittee office.
4. Purchases of animals other than through this system must be cleared through the ACVS office. Health certificates will be required.

REQUIREMENTS/COMMENTS
Please ensure that individual(s) performing procedures on live animals, as described in this protocol, are familiar with the contents of this document.

The holder of this Animal Use Protocol is responsible to ensure that all associated safety components (biosafety, radiation safety, general laboratory safety) comply with institutional safety standards and have received all necessary approvals. Please consult directly with your institutional safety officers.

c.c. Approved Protocol - G. Santyr, A. Farag, M. Pickering
Approval Letter - G. Santyr, A. Farag, M. Pickering

The University of Western Ontario
Animal Use Subcommittee / University Council on Animal Care
Health Sciences Centre, • London, Ontario • CANADA – N6A 5C1
PH: 519-661-2111 ext. 86770 • FL 519-661-2028 • www.uwo.ca / animal

Appendix B: Ventilator Setup

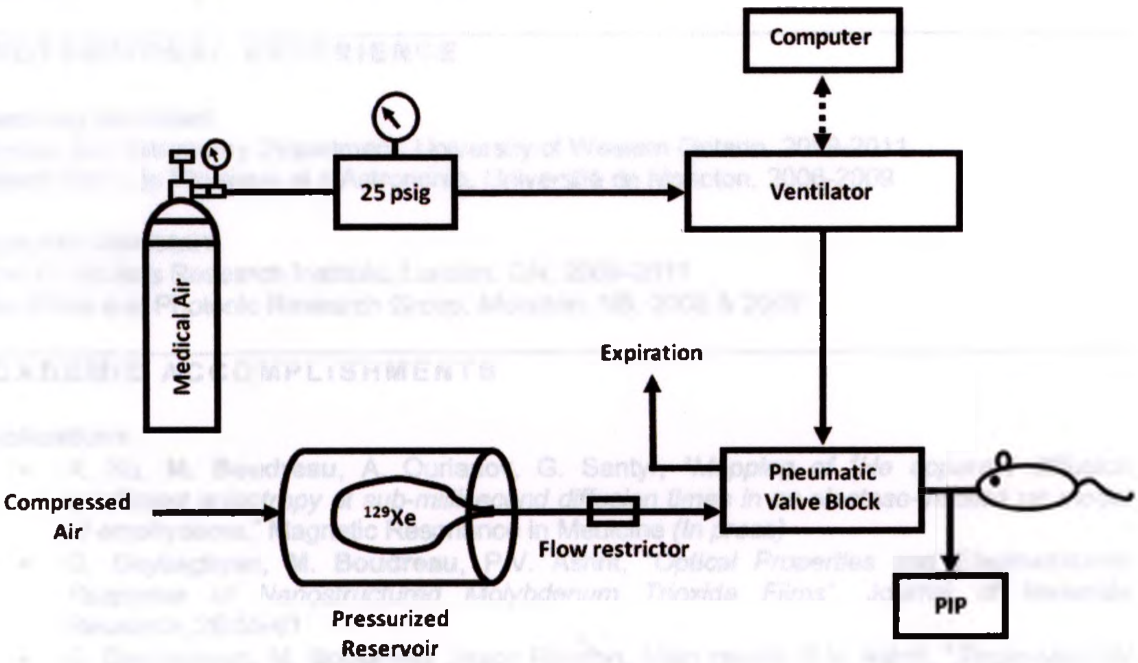

Schematic diagram courtesy of Marcus Couch